



BULGARIAN
ACADEMY
OF SCIENCE

— 1869 —

Bulgarian Academy of Sciences



Institute of Astronomy and National Astronomical Observatory

Solar Transients From The Sun to Earth Coronal Bright Fronts, Radio Bursts, and Energetic Protons

Autoreferat of PhD dissertation
4.1 Physics, Specialization: Heliophysics

Mohamed ElSayed Nedal AbulAinain Mohamed

Supervisor: Assoc. Prof. Kamen Asenov Kozarev
Sofia March 26, 2024

Acknowledgments

Pursuing a doctoral degree during a global pandemic has been a challenging yet incredible and rewarding journey of personal growth and intellectual stimulation. This dissertation would not have been possible without the guidance and support of many incredible people around me.

First and foremost, I am deeply grateful to my advisor, Dr. Kamen Kozarev. Thank you for giving me the opportunity to work on such an interesting and exciting project (SPREADFAST: Solar Particle Radiation Environment Analysis and Forecasting—Acceleration and Scattering Transport). Thank you for granting me the flexibility to work and the freedom to explore and experiment with new ideas. Your insightful feedback, unwavering encouragement, and dedication to my success have been invaluable throughout this process. I am incredibly grateful for your patience during moments of doubt and your enthusiasm that reignited my passion when I needed it most, as well as your ability to help me refine my thoughts and ideas. I am truly fortunate to have had you as my advisor.

I extend my heartfelt gratitude to my colleagues in the Sun and Solar System Department at the Institute of Astronomy and National Astronomical Observatory, Bulgarian Academy of Sciences: Dr. Rositsa Miteva, Dr. Oleg Stepanyuk, and Dr. Momchil Dechev. Thank you for the stimulating discussions, the collaborative spirit, and for generously sharing your expertise. Your valuable advice, feedback, and support have greatly enriched my experience. I am also grateful to Nestor Arsenov and Yordan Darakchiev for the insightful discussions on deep learning models, which have been valuable in shaping my understanding.

A special thank you goes to Dr. Pietro Zucca and Dr. Peijin Zhang for introducing me to the fascinating world of radio observations from the Low-Frequency Array (LOFAR) and guiding me through the intricacies of working with the data and relevant software. Thank you for the cherished moments we shared during my visits to the Netherlands and other places; those experiences have left an indelible imprint.

Furthermore, I am grateful for the financial support provided by the MOSAICS project (Modeling and Observational Integrated Investigations of Coronal Solar Eruptions) and the STELLAR project (Scientific and Technological Excellence by Leveraging LOFAR Advancements in Radio Astronomy). This funding has been a tremendous blessing, allowing me to focus wholeheartedly on my research without financial constraints, and has significantly contributed to the successful completion of this dissertation.

My deepest appreciation goes to my family. Thank you for your unwavering love, belief in me, and constant prayers and encouragement throughout this long journey. You have been my source of strength and motivation. To my dear Bulgarian, Egyptian, and Arab friends, thank you for the countless moments of laughter, the much-needed distractions, and for reminding me of the vibrant world beyond academia. Your support and companionship, especially during my initial period in Bulgaria, have rendered this experience all the more enjoyable.

Finally, I would like to acknowledge and express my heartfelt gratitude to all those who have directly or indirectly contributed to this work. The collective efforts of all contributors, no matter how big or small, have played a crucial role in bringing me to this point and the successful completion of this dissertation.

Those four years were the most beautiful time of my life and I will always cherish them. Thank you all from the bottom of my heart.

Solar Transients From The Sun to Earth

Coronal Bright Fronts, Radio Bursts, and Energetic Protons

Mohamed ElSayed Nedal AbulAinain Mohamed

Institute of Astronomy and National Astronomical Observatory
Bulgarian Academy of Sciences
Sun and Solar System Department

Supervisor: Assoc. Prof. Kamen A. Kozarev

Abstract

This interdisciplinary thesis advances our understanding of solar transients by investigating the early dynamics of Coronal Bright Fronts (CBFs), diagnosing solar type III radio bursts, and forecasting Solar Energetic Proton (SEP) integral fluxes. Integrating these studies, we reveal the relationships among these phenomena and their implications for space weather forecasting and hazard mitigation. Our analysis of 26 CBFs, using the Solar Particle Radiation Environment Analysis and Forecasting–Acceleration and Scattering Transport (SPREAdFAST) framework and data from the Atmospheric Imaging Assembly (AIA) and the Large Angle and Spectrometric Coronagraph (LASCO) instruments, unveils temporal evolution, plasma properties, and compressional characteristics. The second study, employing the Low-Frequency Array (LOFAR) and Parker Solar Probe (PSP), characterizes 9 type III radio bursts in the combined dynamic spectrum and 16 in the LOFAR spectrum alone. Potential Field Source Surface (PFSS) and magnetohydrodynamic (MHD) models offer insights into plasma conditions and magnetic fields, advancing our understanding of type III radio bursts triggered by accelerated electrons associated with CBFs and solar flares. Addressing forecasting, a bi-directional Long short-term memory (BiLSTM) neural network using OMNIWeb data from 1976 to 2019 predicts SEP fluxes, emphasizing the hazardous influence of energetic particles on Earth and technology. This work provides a unified framework, highlighting the interconnected nature of solar transients and their collective impact on space weather.

Contents

1	Introduction	2
1.1	Background and Motivation	2
1.1.1	Coronal Waves	3
1.1.2	Solar Radio Bursts	4
1.1.3	Solar Energetic Protons Forecasting	5
1.2	Objectives and Scope	5
1.3	Outlines	6
2	Remote Observations: Early-stages and Later-stages of Eruption	7
2.1	Introduction	7
2.2	EUV Observations	8
2.3	Data Analysis and Methods	10
2.4	CBF Kinematics and Geometric Modeling: Case Study May 11, 2011	10
2.4.1	Event Context	10
2.4.2	Low Corona Part	11
2.4.3	Middle/Outer Corona Part	11
2.5	Statistical Study	11
2.6	<i>Wavetrack</i> : Automated Recognition and Tracking of Solar Eruptions	18
2.6.1	Overview	18
2.6.2	Image Filtering Techniques	18
2.6.3	Wavetrack for Coronal Wave and Filament Tracking	19
2.6.4	Fourier Local Correlation Tracking (FLCT)	19
2.6.5	Results	19
2.7	Geomagnetic Storms: CME Speed De-Projection vs. In Situ Analysis	23
2.7.1	Overview	23
2.7.2	PyThea 3D De-Projection Tool	23
2.7.3	Results	24
2.8	Discussion	28
2.8.1	CME Kinematics and Coronal Shock Wave Characteristics	28
2.8.2	Dynamic Coronal Features Analysis with Wavetrack	28
2.8.3	Subjectivity in CME Speed Determination	29
2.9	Conclusions	29
3	Solar Radio Observations: Integrating Data for Coronal Diagnostics	31
3.1	Introduction	31
3.2	Observations	31
3.2.1	PSP Observations	34
3.2.2	LOFAR Observations	34
3.3	Methods	34
3.3.1	Imaging of Radio Sources	34
3.3.2	Modeling	36
3.4	Results and discussion	36
3.4.1	Type III Radio Burst Detection and Characterization	36
3.4.2	Imaging of Radio Emission Sources	36
3.4.3	Plasma Diagnostics and Magnetic Field Analysis	38
3.5	Summary and conclusions	38

4 Modeling and Forecasting of Solar Energetic Protons	42
4.1 Introduction	42
4.2 Early-Stage SEP Acceleration by CME-Driven Shocks	43
4.2.1 Overview	43
4.2.2 Coronal SEP Acceleration	43
4.2.3 Input Data and Spectral Fitting	43
4.2.4 Transport of SEPs and Comparison with ERNE Observations	43
4.2.5 Results and Discussions	43
4.3 Solar Proton Flux Forecasting with Deep Learning Models	44
4.3.1 Data Preparation	44
4.3.2 Method	44
4.3.3 Results and discussion	46
4.4 Conclusions	51
5 Summary	53

List of Tables

2.1	List of the CBF events with their associated flares and CMEs.	8
2.2	Mean values and their standard deviation of the wave parameters in the radial direction and the lateral direction for the left and right flanks, at the front, peak, and back sides of the wave for the event occurred on May 11, 2011, in the SDO/AIA FOV.	12
2.3	Mean, median, and standard deviation of the shock parameters output, from the interaction of the S2M spheroid with the MAS MHD model results, for the shock's cap and flanks and for the whole shock surface, for the event on May 11, 2011.	13
2.4	Statistics of the EUV wave kinematics in the SDO/AIA FOV for the 26 events. LL and LR refer to the lateral left and right flanks, respectively. Rad refer to the radial front direction.	15
2.5	CME Speeds ($km\ s^{-1}$) for Observers 1 and 2. Credit goes to Miteva et al. (2023).	25
2.6	Table displaying Pearson correlation coefficients among the GS Dst index, CME speed, and various solar parameters, with the respective sample sizes indicated in parentheses. Credit goes to Miteva et al. (2023).	26
2.7	Tabular representation of Pearson correlation coefficients between the GS Dst index and various parameters of IP phenomena. The data is derived from Wind satellite measurements, unless otherwise stated, with the corresponding sample sizes indicated in parentheses. Credit goes to Miteva et al. (2023).	26
3.1	Characteristics of the type III bursts detected via the automatic algorithm from the combined spectrum.	35
4.1	Summary of the performance results of the models for the validation and test sets.	47
4.2	Confusion matrix for the energy channel ≥ 10 MeV predictions in the test set.	48
4.3	Comparing the skill scores with previous models. The dashed entries mean the data is unavailable (Whitman et al. (2023) for more details).	49
4.4	The MSE/MAE for the validation and test sets over six forecasting windows.	51

List of Figures

1.1	On the left side, a graphical illustration, adapted from ESA/A. Baker, CC BY-SA 3.0 IGO, depicts different eruptive phenomena, while on the right side, there is a representation of spacecraft data (specifically Wind/Waves data from Gopalswamy et al. (2019)) showcasing a radio dynamic spectra, emphasizing distinct spectral categories of SRBs on November 9, 2000. Type-II bursts are correlated with the shock front of a CME, whereas Type-IIIIs are connected with the acceleration of SEPs. Image courtesy ¹	2
1.2	Composite image from the AIA and LASCO telescopes on the NASA-GSFC SDO and NASA/ESA SOHO spacecrafts shows a large CME being ejected to the east and its typical structure.	4
1.3	Classification of solar radio bursts	5
1.4	Coronagraph image captured by the SOHO/LASCO C3 instrument during a Halo-CME event. The speckled appearance of the corona results from signal contamination due to particles generated when SEPs interact with the SOHO telescope.	6
2.1	Illustration for the annulus method used to extract kinematic data from AIA images. (A) shows the full Sun disk with the relevant region highlighted for analysis (green sector). The white box outlines the AIA FOV. (B) displays the extracted annular region mapped onto polar coordinates, with the actual data extent marked by the white curve. Black lines indicate the directions used for measuring radial and lateral motions. (C) shows a stacked plot of intensity along the radial direction, with green markers highlighting intensity peaks and their corresponding distances from the CBF wavefront. The white lines represent the time interval during which the CBF is tracked within the AIA FOV. This figure is curated from (Kozarev et al. 2017).	9
2.2	Synthetic shock model divided into three segments; the cap zone in blue and the flank zones are in red and green.	11
2.3	AIA running-difference images capture a coronal wave evolving over 9 minutes near the Sun's western limb, exhibiting markedly changing intensity and structure as observed in 171, 193, and 211 Å.	12
2.4	Time-series kinematics of the CBF parameters for the front, peak, and back positions in the AIA FOV, with measurement uncertainties shown as small bars over the data points. The horizontal lines in the speed and acceleration panels denote the mean speeds and accelerations for the wave front, peak, and back with respective colors. The left and right columns represent the lateral kinematic measurements in the left and right flanks of the wave, respectively. The middle column represent the kinematic measurements in the radial direction.	13
2.5	Top panel – Height-time profile compiled from AIA and LASCO measurements for the event occurred on May 11, 2011, fitted with two CME kinematics models from the photosphere up to $17 R_{\odot}$. Middle panel – Difference between the fitting and the real observations. Bottom panel – Relative residuals in %.	14
2.6	Extrapolated radial kinematics for the event occurred on May 11, 2011, based on the ballistic model of Gallagher et al. (2003) up to $17 R_{\odot}$.	15
2.7	Dynamic spectra of the EUV waves kinematics in the AIA FOV. The panels from the top to the bottom are the wave speeds, acceleration, mean intensity, and thickness. The left column is for the lateral left flank, the central column is for the radial direction, and the right column is for the lateral right flank.	16
2.8	Histograms of along-field-lines model plasma parameters in the solar corona for all the 26 events. The vertical dashed red lines are the mean values.	17

2.9	Wavetrack images of a May 11, 2011 eruption, with CBF mask applied. Four image pairs shown, separated by 2 minutes, to track CBF over time. Credit goes to Stepanyuk et al. (2022).	20
2.10	FLCT model output for four image pairs from Fig. 3. Left: the plane-of-sky velocity vectors. Right: plane-of-sky speed. Credit goes to Stepanyuk et al. (2022).	21
2.11	Analysis of the center of mass and geometric centers' motion during the May 11, 2011 event. The different rows present the X-, Y-, and R- positions for both GC and CM, the distance between GC and CM in <i>km</i> , and the angle between these two points over time. Credit goes to Stepanyuk et al. (2022).	22
2.12	3D reconstructions of a CME (E03) using the spheroid, ellipsoid, and GCS model from the PyThea tool performed by observers 1 and 2 (top and bottom row, respectively). Credit goes to Miteva et al. (2023).	24
2.13	Scatter plot illustrates the comparison of 3D de-projected CME speeds derived from the spheroid model (depicted as diamonds), the ellipsoid model (represented by stars), and the GCS model (indicated as dots) versus the measurement errors for observers 1 (left) and 2 (right). Credit goes to Miteva et al. (2023).	25
2.14	Scatter plot illustrating the relationship between the Dst index and CME speed, incorporating data from the SOHO/LASCO instrument (represented by filled circles) and 3D de-projections (depicted by empty circles). Credit goes to Miteva et al. (2023).	26
2.15	Comprehensive scatter plots illustrating the relationships between Dst index and various solar wind parameters, including Wind/ACE ICME speed, IP shock speed, Mach number, duration of sheath region, Bz, magnetic field jump, temperature jump, and density jump. Credit goes to Miteva et al. (2023).	27
3.1	Radio dynamic spectra for a single burst obtained from multiple instruments. The top-left panel is from the LOFAR/LBA instrument, the top-right is from the PSP/FIELDS instrument, the bottom-left is from the STEREO/SWAVES instrument, and the bottom-right is from the Wind/WAVES. The vertical red dashed line denotes the start time of the burst.	32
3.2	Top view of the spacecraft positions in the ecliptic plane at 12:15 UT on April 3, 2019, with the Sun-Earth line as the reference point for longitude. The Earth's location is representative of the positions of LOFAR, Wind/WAVES, and GOES-15/XRS instruments. The spacecraft were connected back to the Sun by a 400 km/s reference Parker Spiral. The black arrow represents the longitude of AR12737 and the blue arrow represents the longitude of the AR12738. The gray dotted lines are the background Parker spiral field lines. The black dashed spiral shows the field line connected to the AR12737, and the blue dashed spiral is connected to the AR12738. The figure is generated using the Solar MAGnetic Connection Haus (Solar-MACH) tool (Gieseler et al. 2023).	32
3.3	Exploring the X-ray and EUV emissions from the Sun. The top panel showcases a cutout region of the SDO/AIA 193 Å image of the solar disk along with the STEREO-A EUVI 195 Å point of view. The white curve is the limb of the solar disk as seen by AIA from the right side. The red and blue colors are the contours of the line-of-sight magnetogram from the SDO/HMI instrument. The levels are (50, 100, 150, 300, 500, 1000) Gauss. The middle panel shows the X-ray flux from the GOES-14 spacecraft shows minimum activity. The bottom panel shows the time series of the ESP Quad band from the SDO/EVE instrument, which shows the solar irradiance in the EUV band.	33
3.4	Automatic detection of type III radio bursts from the combined radio dynamic spectrum of LOFAR and PSP instruments. The dashed horizontal lines separates the LOFAR frequency range (top) and the PSP frequency range (bottom).	35
3.5	Automatic detection of type III bursts observed by LOFAR. The red symbols along the fit lines are the (f, t) coordinates of the image snapshots shown in Figure 3.6.	36
3.6	Persistence imaging for the 16 type III bursts detected in the LOFAR dynamic spectrum. The label shows the observation frequencies in MHz and times in (minutes:seconds from 12:00:00 UT). Here, the color coding is not absolute, but rather each panel has its own color code.	37

3.7	Different viewing angles for the deprojection of the radio sources of the sixth burst using the $2.5 \times$ Newkirk electron-density model on the PFSS solution. The black arrow points toward the Earth's LOS. The yz plane is the POS as seen from the Earth. The red dashed line is a spline curve fit for the sources' centroids. The red, black, and blue curves are the open northern, closed, and open southern field lines, respectively. The opacity of the closed field lines is decreased for better visualization.	39
3.8	Synthesized maps of plasma parameters obtained using the FORWARD toolset, with the 70%-contour of radio emission of the sixth burst at the first timestamp (12:34:06.8 UT) at the frequency of 72.26 MHz depicted on top of the 2D POS cuts. The left column represents, from top to bottom, plasma density, magnetic field, and the total plasma dynamic pressure. The right column represents, from top to bottom, the temperature, plasma beta, and the Alfvén speed.	40
3.9	Coronal plasma parameters sampled from the 2D maps by the source centroids. The top panel shows (from left to right) the plasma density profiles from the MAS model, $2.5 \times$ Newkirk model, and the theoretical densities under the fundamental and harmonic assumptions, plasma temperature, and magnetic field. The bottom panel shows, from left to right, the total plasma dynamic pressure, Alfvén speed, and plasma beta. The x-axis is inverted to demonstrate a progression of increasing radial distance from the Sun as the observer moves towards the right.	41
4.1	Data splitting for all input features, showing the training, validation, and testing sets. Daily data from 1976-12-25 00:00 to 2019-07-30 00:00. The gray shading labels the solar cycles from SC21 to SC24.	45
4.2	Architecture of a single BiLSTM layer. The blue circles at the bottom labeled by $(x_0, x_1, x_2, \dots, x_i)$ are the input data values at multiple time steps. The purple circles, on the other hand, are the output data values at multiple time steps labeled by $(y_0, y_1, y_2, \dots, y_i)$. The dark green and light green boxes are the activation units of the forward and backward layers, respectively. The orange and yellow circles are the hidden states at the forward and backward layers, respectively. Both the forward and backward layers compose a single hidden BiLSTM layer. The figure is adopted from Olah (2015)	46
4.3	Benchmarking of 10 models, shows the Huber loss for the validation and test sets.	46
4.4	<i>Left Panel</i> - The Huber loss vs. the number of training epochs for the BiLSTM model for the validation and test sets, for the 3 energy channels. <i>Middle Panel</i> - The mean absolute error (MAE); the model's metric vs. the number of training epochs. <i>Right Panel</i> - Shows how the learning rate of the Adam optimizer changes over the number of epochs.	47
4.5	Correlation between the model predictions and observations for 1-day, 2-day, and 3-day ahead for >10 MeV (top panel), >30 MeV (middle panel), and >60 MeV (bottom panel). The panels in the left column represent all the points of the test set, those in the right column represent all the observations points with daily mean flux ≥ 10 pfu.	48
4.6	Comparison between the model outputs and observations of the test set for the 3 energy channels. In addition to the rolling-mean window correlation for 1-day ahead predictions.	49
4.7	The model's forecasts for the out-of-sample testing set for the >10 MeV channel are shown at forecast horizons of 1 day, 2 days, and 3 days ahead, using samples of data from December in selected years mentioned in the top-left side of the plots.	50
4.8	Temporal heatmap shows a comparison between the model outputs and observations for the rolling-mean window correlation of the integral >10 MeV proton flux at six predicting windows. The top panel represents the validation set and the bottom panel represents the testing set. The numbers on the y-axis are the mean R values.	51
4.9	Comparison between the model's forecast and the observations for the integral >10 MeV proton flux at forecast horizon of 1 hour ahead. The top panel represents a sample of the validation set and the bottom panel represents a sample of the testing set.	52

Definitions and Acronyms

Here, I provide definitions for key domain-specific terms and measurement concepts used consistently throughout the thesis. Additionally, relevant terminology will be introduced within the corresponding chapters. Below is a compilation of the essential technical terms and acronyms featured in this work:

- CME – Coronal Mass Ejection
- ICME – Interplanetary Coronal Mass Ejection
- SF – Solar Flare
- CIR – Corotating Interaction Region
- IMF – Interplanetary Magnetic Field
- GS – Geomagnetic Storm
- Dst – Disturbance storm time
- AU – Astronomical Unit
- MPA – Measurement Position Angle
- SEPs – Solar Energetic Particles/Protons
- ESP – Energetic Storm Particle
- EUV – Extreme Ultra-Violet
- CBF – Coronal Bright Front
- SRB – Solar Radio Burst
- DH – Decameter-Hectometric
- SOHO – Solar and Heliospheric Observatory
- LASCO – Large Angle and Spectrometric Coronagraph
- ERNE – Energetic and Relativistic Nuclei and Electron
- EIT – Extreme ultraviolet Imaging Telescope
- TRACE – Transition Region and Coronal Explorer
- ESA – European Space Agency
- MHD – Magneto-Hydro-Dynamic
- MAS – Magnetohydrodynamic Algorithm outside a Sphere
- PSI – Predictive Science Inc.
- PFSS – Potential Field Source Surface
- AIA – Atmospheric Imaging Assembly
- SDO – Solar Dynamic Observatory
- EUVI – Extreme Ultraviolet Imager
- STEREO – Solar Terrestrial Relations Observatory
- LOFAR – Low-Frequency Array
- PSP – Parker Solar Probe
- GOES – Geostationary Operational Environmental Satellite
- SN – Sunspot Number
- SC – Solar Cycle
- sfu – solar flux units
- pfu – proton flux units
- L1 – First Lagrange point
- SPDF – Space Physics Data Facility
- SILSO – Sunspot Index and Long-term Solar Observations
- NOAA – National Oceanic and Atmospheric Administration
- NASA – National Aeronautics and Space Administration
- GSFC – Goddard Space Flight Center

SPREAdFAST – Solar Particle Radiation Environment Analysis and Forecasting–Acceleration and Scattering Transport

CASHeW – Coronal Analysis of SHocks and Waves

DSA – Diffusive Shock Acceleration

SDA – Shock Drift Acceleration

S2M – Synthetic Shock Model

EPRREM – Energetic Particle Radiation Environment Module

DEM – Differential Emission Measure

FLCT – Fourier Local Correlation Tracking

CM – Centers of Mass

GC – Geometric Center

GCS – Graduated Cylindrical Shell

NN – Neural Network

ML – Machine Learning

DL – Deep Learning

CNN – Convolutional Neural Network

GAN – Generative Adversarial Networks

RNN – Recurrent Neural Network

BiLSTM – Bi-directional Long short-term Memory

Adam – Adaptive moment estimation

MIMO – Multi-Input Multiple Output

MSE – Mean Squared Error

MAE – Mean Absolute Error

MSLE – Mean Squared Logarithmic Error

TP – True Positive

TN – True Negative

FP – False Positive

FN – False Negative

POD – Probability of Detection

POFD – Probability of False Detection

FAR – False Alarm Rate

CSI – Critical Success Index

TSS – True Skill Statistic

HSS – Heidke Skill Score

Chapter 1

Introduction

1.1 Background and Motivation

The Sun, a typical star at the center of our solar system, displays various forms of activity across different scales. This includes energetic eruptive events like solar flares and Coronal Mass Ejections (CMEs), driven by the release of magnetic energy stored in complex magnetic structures in the solar atmosphere (Moore et al. 2001; Priest & Forbes 2007; Zhang et al. 2012; Amari et al. 2014). These events release electromagnetic radiation and energetic particles (Schwenn 2006; Pulkkinen 2007), affecting *space weather* (Schrijver & Siscoe 2010a; Eastwood et al. 2017) (Fig. 1.1). They cause disturbances in near-Earth and planetary environments, impacting communication, satellites, power grids, aviation, and space missions (Lanzerotti 2001; Schwenn 2006; Pulkkinen 2007; Liliensten et al. 2014).

Understanding these solar phenomena and their impacts is crucial globally. Research aims to uncover the underlying physical processes through observations, theory, and modeling, while also developing predictive capabilities for space weather. This field, known as *heliophysics* (Schrijver & Siscoe 2010b), encompasses studying solar, heliospheric, and geospace plasma processes, their impacts on technology and space assets, and strategies for prevention and mitigation (Schrijver et al. 2015; Schrijver 2015). Initiatives like NASA's Living With a Star program and the National Science Foundation's Space Weather activities drive scientific understanding and predictive capabilities (Brewer et al. 2002).

This thesis focuses on investigating key aspects of solar eruptive activity and its impacts within the realm of heliophysics and space weather. Specific topics include studying the propagation of coronal disturbances triggered by CMEs and flares, the characteristics of solar type III radio bursts, and forecasting Solar Energetic Particle (SEP) events, which pose significant space radiation hazards.

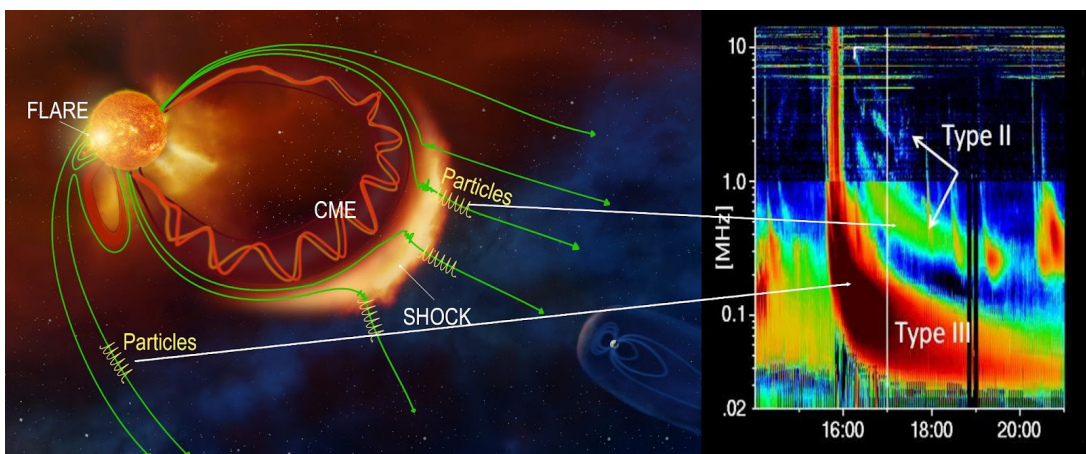


Figure 1.1: On the left side, a graphical illustration, adapted from ESA/A. Baker, CC BY-SA 3.0 IGO, depicts different eruptive phenomena, while on the right side, there is a representation of spacecraft data (specifically Wind/Waves data from Gopalswamy et al. (2019)) showcasing a radio dynamic spectra, emphasizing distinct spectral categories of SRBs on November 9, 2000. Type-IIIs are correlated with the shock front of a CME, whereas Type-IIIs are connected with the acceleration of SEPs. Image courtesy¹

The thesis investigates the origins and propagation mechanisms of transient phenomena resulting from solar eruptions. It employs observational data, analytical theory, modeling, and data science techniques. Despite decades of study using space mission observations, gaps persist in understanding their underlying physics and space weather impacts. The thesis aims to provide new insights within the framework of heliophysics research. Each research topic is explored in dedicated chapters, discussing background, significance, observational challenges, knowledge gaps, and relevant literature. More details can be found in the thesis.

1.1.1 Coronal Waves

Coronal waves, also known as Coronal Bright Fronts (CBFs) or EUV waves, are large-scale arc-shaped disturbances observed propagating across the solar corona following the eruption of CMEs and solar flares (Thompson et al. 1998; Nindos et al. 2008; Vršnak & Cliver 2008; Magdalenić et al. 2010a; Veronig et al. 2010; Warmuth 2015). These waves, visible in EUV, white-light coronal emission, and radio wavelengths, can span distances of up to several hundred Mm and travel at speeds ranging between $100\text{-}1000 \text{ km s}^{-1}$, faster than the local characteristic speed in the corona, eventually transforming into shock waves (Pick et al. 2006; Thompson & Myers 2009; Nitta et al. 2013; Liu & Ofman 2014). They consist of piled-up plasma with higher density, making them appear brighter in white-light images.

Discovered through observations obtained with the Extreme ultraviolet Imaging Telescope (EIT) instrument on the Solar and Heliospheric Observatory (SOHO) that was launched in 1995, coronal waves appear as bright propagating fronts in 19.5 nm wavelength imaging of Fe XII emission lines formed at approximately 1.5 MK plasma (Thompson et al. 1998). Subsequent studies using SOHO/EIT and the Transition Region and Coronal Explorer (TRACE) found correlations between coronal waves and CMEs, suggesting they are fast-mode magnetohydrodynamic (MHD) waves driven by CME lateral expansions (Biesecker et al. 2002).

Since 2010, the initiation and evolution of coronal waves have been observed with unprecedented resolution by the Atmospheric Imaging Assembly (AIA) on the Solar Dynamics Observatory (SDO), using multiple EUV passbands sensitive to a wide temperature range (Lemen et al. 2012; Nitta et al. 2013). Observing and studying coronal shock waves remotely is typically done through EUV observations using space-based instruments like AIA onboard the SDO spacecraft. Alternatively, shock waves can be indirectly observed through the detection of type II radio bursts, commonly associated with shock waves in the solar corona (Vršnak & Cliver 2008).

The AIA instrument, with its exceptional spatial and temporal resolution, has provided significant insights into the dynamics of the low solar corona over the past decade (Patsourakos et al. 2010; Ma et al. 2011; Kozarev et al. 2011). By observing the solar disk in bands 193 and 211 Å, it distinguishes compressive waves in the lower corona, offering valuable information about the kinematics and geometric structure of CBFs. Observations off the solar limb are preferred to study the evolution of the wave's leading front accurately, mitigating projection effects that may introduce ambiguities (Kozarev et al. 2015).

CMEs typically consist of three parts (Fig. 1.2): the CME Front, CME Cavity, and CME Core (Vourlidas et al. 2013). CBFs form in front of the expanding front of CMEs. In situ observations of shock waves classify them into quasi-parallel, quasi-perpendicular, sub-critical, and super-critical shocks based on the angle between the wavefront normal vector and the upstream magnetic field lines (Tsurutani 1985). Coronal waves display diverse morphology and kinematics, ranging from circular fronts to narrow jets or expanding dome-like structures (Veronig et al. 2010). However, fundamental questions persist regarding their physical nature and drivers (Chen 2016; Vršnak & Cliver 2008; Warmuth 2015), including whether they are true wave disturbances or pseudo-wave fronts (Wills-Davey et al. 2007; Vršnak & Cliver 2008; Delannée & Aulanier 1999; Chen et al. 2002).

Extensive observational and modeling studies have been conducted to evaluate these paradigms, but a consensus remains elusive (Patsourakos & Vourlidas 2012; Long et al. 2017). Addressing these outstanding questions is crucial, as coronal waves are being incorporated into models as primary agents producing SEP events and geomagnetic storms following CMEs (Rouillard et al. 2012; Park et al. 2013). The present thesis undertakes an extensive statistical analysis of coronal EUV wave events observed by SDO to provide new insights into their kinematical properties and relationship to CMEs and plasma properties in the corona. It focuses on analyzing their large-scale evolution as a function of distance and direction from the source region, aiming to uncover systematic trends in their propagation kinematics and exploring relationships between different pairs of kinematical parameters compared to previous works.

¹<https://www.dias.ie/cosmicphysics/astrophysics/astro-surround/>

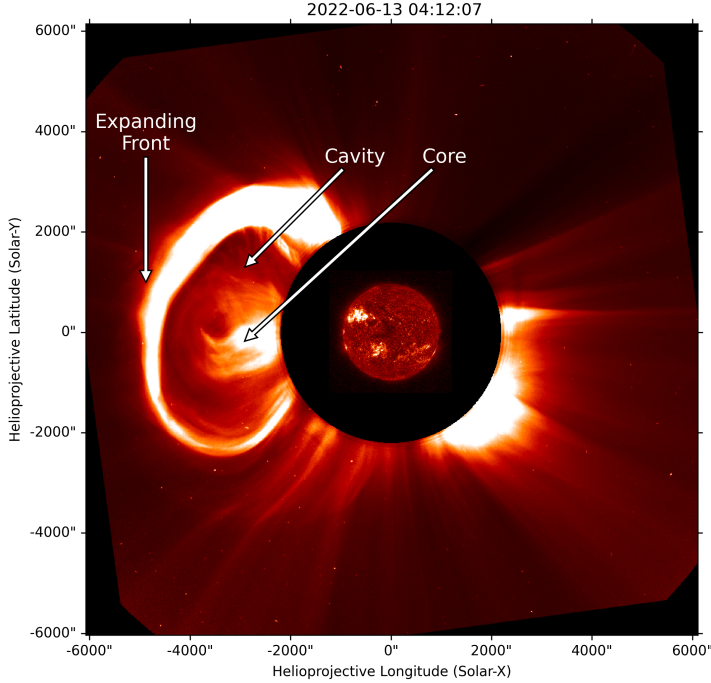


Figure 1.2: Composite image from the AIA and LASCO telescopes on the NASA-GSFC SDO and NASA/ESA SOHO spacecrafts shows a large CME being ejected to the east and its typical structure.

These results have important implications for incorporating coronal waves into predictive models of CMEs and SEP events for future space weather forecasting.

1.1.2 Solar Radio Bursts

Solar radio emissions, including solar radio bursts, are extensively studied due to their association with solar activity and potential impacts on Earth's atmosphere and technology. Type III bursts, originating from transient energetic electron beams injected into the corona, serve as remote diagnostics for studying energetic electrons and plasma dynamics (Ergun et al. 1998; Pick et al. 2006; Reid 2020). These bursts, linked to plasma density, offer insights into processes driving solar active phenomena like CMEs and flares (Reid & Ratcliffe 2014; Kontar et al. 2017). They provide valuable information on electron acceleration and transport, shedding light on the dynamic interaction between non-thermal electron distributions and ambient plasma (Melrose 1980).

Pioneering observations in the 1940s led to the classification and subsequent spectrographic studies of solar radio bursts, uncovering emission mechanisms and particle diagnostics (Wild et al. 1963; Suzuki & Dulk 1985). Magnetic reconnection models provided theoretical explanations for particle acceleration generating these bursts (Holman et al. 2011). Radio imaging spectroscopy enables tracking of radio sources on the Sun, offering insights into energetic particle transport from the Sun to Earth (Krucker et al. 2011; Klassen et al. 2003a,b). Different burst types are observed and classified based on their spectral characteristics (Fig. 1.3) (Wild et al. 1963), with this thesis focusing on a detailed analysis of solar type III radio bursts.

Type III bursts manifest as intense enhancements of radio flux with rapid frequency drifts, observable across a broad frequency spectrum from GHz to kHz (Wild & McCready 1950; Lecacheux et al. 1989; Bonnin et al. 2008). They arise from energetic electron beams ejected during magnetic reconnection, with the rapid drift corresponding to the beams' propagation from the Sun's lower corona outward along open magnetic field lines (Cane et al. 2002; MacDowall et al. 2003). Investigating their source locations, plasma environments, and beam kinematics is vital for understanding coronal particle acceleration and transport relevant to SEP forecasting models.

Despite over 50 years of study, gaps persist in understanding the exciter beams and emission mechanisms of type III bursts, including detailed electron acceleration sites, beam configurations, burst onset drivers, and the role of density fluctuations in beam propagation (Reid & Kontar 2018b,a; Li & Cairns 2012). Recent work combining imaging and spectral data with modeling aims to constrain radio burst

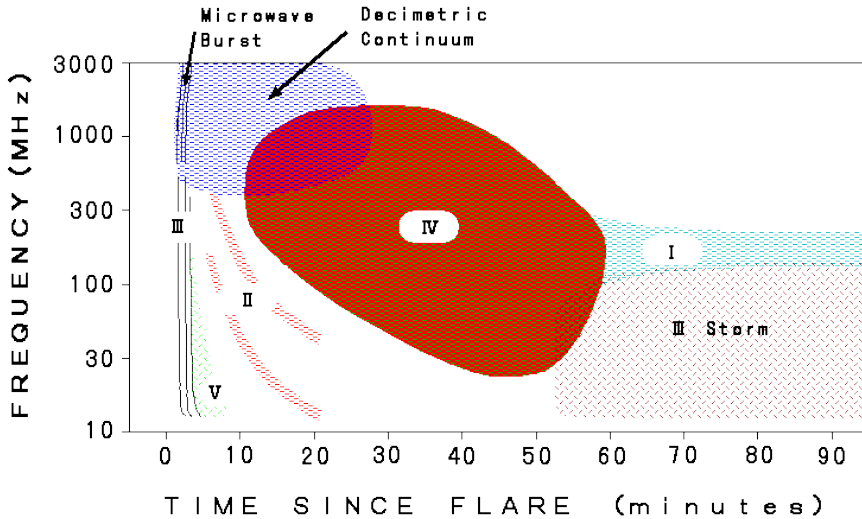


Figure 1.3: Diagram illustrating the classification of solar radio bursts. Image courtesy²

exciters in detail (Chen et al. 2013; Kontar et al. 2017), yet challenges remain in reconciling models with observations and predicting radio diagnostics. Coordinated observations and modeling efforts can advance knowledge in these areas, aiding predictions of energetic electron properties based on radio diagnostics. This thesis undertakes a detailed investigation of a solar type III burst, deriving electron beam trajectories, coronal densities, and emission sources, providing insights into the corona plasma environment and energetic electron transport relevant to SEP forecasting applications.

1.1.3 Solar Energetic Protons Forecasting

Solar energetic protons (SEPs) are high-energy particles originating from solar flares and CMEs, characterized by their high energy levels (up to the GeV/nucleon range) and potential to cause radiation damage (Aschwanden 2002; Lin 2005; Reames 2013). Their fluence and energy spectrum depend on various factors, including solar activity strength and interplanetary conditions (Kahler et al. 1984, 1987; Debrunner et al. 1988; Miteva et al. 2013; Trottet et al. 2015; Dierckxsens et al. 2015; Le & Zhang 2017; Gopalswamy et al. 2017). SEPs exhibit a strong association with the solar cycle, peaking during its maximum phase (Reames 2013), although the exact relationship remains complex and not fully understood (Nymmik 2007; Ramstad et al. 2018).

Figure 1.4 illustrates the impact of SEPs during the *Halloween storm* of 2003, a significant solar event. SEPs play a crucial role in adverse space weather, posing radiation hazards to humans and equipment in space (Reames 1999). SEP events consist primarily of protons accelerated by CME-driven shock waves, with gradual events involving protons above ~ 10 MeV and impulsive events dominated by electrons and ions like ${}^3\text{He}$ (Reames 2013; Nitta et al. 2015).

SEP forecasting models face challenges due to the complex physics involved, motivating the exploration of data-driven approaches using machine learning (Kahler et al. 2007; Laitinen & Dalla 2017). Deep learning techniques offer promising avenues for improved predictions, capturing complex relationships between parameters (Florios et al. 2018; Camporeale 2019). This thesis aims to develop deep Neural Network models for predicting SEP intensity profiles, leveraging historical data to enhance forecasting capabilities.

1.2 Objectives and Scope

This PhD thesis explores various solar phenomena, including CBFs, type III radio bursts, and SEP events, aiming to deepen our understanding of solar corona physics and its relation to eruptions and energetic particle radiation.

For CBFs, the research analyzes 26 historical events observed by the AIA instrument on SDO from 2010 to 2017, examining their properties and kinematics in relation to the coronal plasma environment.

²Types of solar radio bursts: http://solar.physics.montana.edu/takeda/radio_burst/srb.html

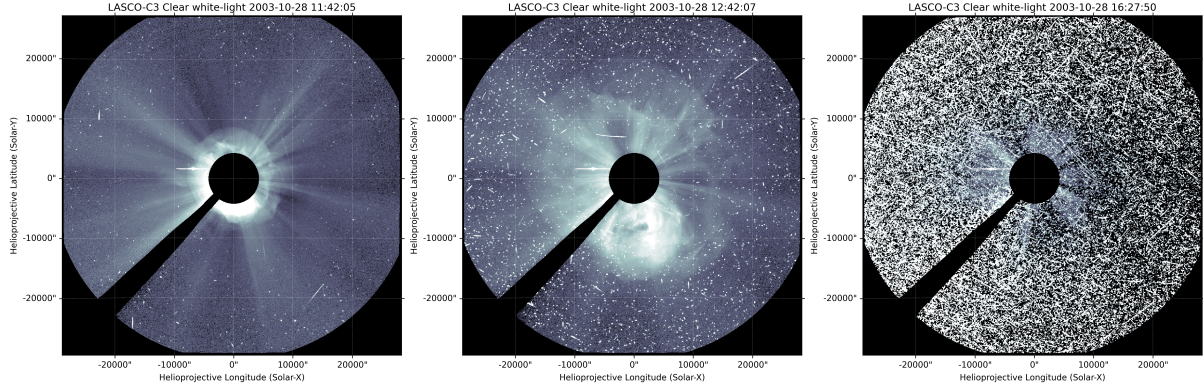


Figure 1.4: Coronagraph image captured by the SOHO/LASCO C3 instrument during a Halo-CME event. The speckled appearance of the corona results from signal contamination due to particles generated when SEPs interact with the SOHO telescope.

Techniques like base-difference images and geometric models are employed to derive measurements, alongside exploring shock properties within the CBFs.

The study of type III radio bursts focuses on unraveling their generation mechanisms, identifying their sources in the solar corona, and investigating relationships with magnetic field structures and plasma environment. It analyzes specific bursts observed on April 3, 2019, using data from LOFAR and PSP instruments, comparing observations with existing models and exploring potential burst sources.

In SEP forecasting, the aim is to develop a BiLSTM neural network model capable of predicting daily SEP integral flux over a three-day window for energy ranges >10 MeV, >30 MeV, and >60 MeV. The model's performance is evaluated against established forecasting models using historical SEP data from the past four solar cycles, assessing accuracy and effectiveness through various metrics and correlation analysis. By addressing these aspects of solar activity, this research advances our understanding of solar dynamics and enhances our ability to predict space weather events impacting Earth.

1.3 Outlines

This dissertation examines CBFs, solar radio bursts, and SEP events. It analyzes the kinematics of CBFs in the solar corona, investigating 26 CBFs associated with SEP events observed between 2010 and 2017. The study employs the SPREAdFAST framework to understand CBF kinematics and plasma parameters, aiding space weather forecasting and SEP event studies (Chapter 2). Additionally, it presents a method for identifying and tracking CME-driven shock waves using wavelet transform and image filtering, with applications in deep-learning solar datasets.

Another study in Chapter 2 explores the correlation between geomagnetic storm intensity and solar and interplanetary phenomena, emphasizing the importance of considering CME speed and magnetic structure orientation for accurate storm prediction. Chapter 3 focuses on type III radio bursts, analyzing an event on April 3, 2019, and characterizing 16 bursts using multi-wavelength data and models, revealing insights about plasma conditions along burst trajectories.

Chapter 4 investigates SEP events, modeling their acceleration and transport during coronal shock events through the SPREAdFAST framework, and developing SEP forecasting models using a BiLSTM neural network. The effectiveness of these models is validated through testing and benchmarking against existing ones. Finally, Chapter 5 summarizes the dissertation's key findings.

Chapter 2

Remote Observations Early-stages and Later-stages of Eruption

This chapter covers three main topics related to EUV waves and CMEs. Firstly, it focuses on the kinematics of CBFs in both the lower and middle/outer coronas, along with an examination of coronal plasma conditions during these eruptions. Additionally, it discusses my contributions to testing and debugging the *Wavetrack* Python library, developed by Stepanyuk et al. (2022), for detecting and tracking solar features using wavelet transforms and filtering techniques. Lastly, it examines the research led by Miteva et al. (2023) regarding the connection between reconstructed 3D CME models and geomagnetic storm intensity, emphasizing the importance of accurate 3D modeling for space weather forecasting. The chapter will present the results of each topic individually, followed by a combined discussion and concluding remarks.

2.1 Introduction

CMEs are prominent indicators of solar activity, observable through various wavelengths including white light, UV, and radio (Vourlidas et al. 2003; Zhang & Dere 2006; Bein et al. 2011; Bastian et al. 2001; Veronig et al. 2010). Early CME phases are effectively observed in Extreme Ultraviolet (EUV) light, facilitated by instruments like AIA aboard SDO (Lemen et al. 2011; Pesnell et al. 2012). CMEs can induce shock waves in the solar corona, visible as EUV waves or CBFs (Thompson et al. 1998; Long et al. 2011).

CBFs are disturbances propagating over the solar disk and limb, often faster than local characteristic speeds, driven primarily by CMEs or solar flares (Thompson et al. 1998; Veronig et al. 2010; Vršnak & Cliver 2008; Magdalenić et al. 2010b; Nindos et al. 2011). They appear as dome-shaped structures in radio and white-light observations, composed of denser plasma and thus appearing brighter in images (Pick et al. 2006; Nindos et al. 2008; Thompson & Myers 2009).

Studies have clarified CBF characteristics both on the solar disk and off the limb, confirming their wave-like nature (Nitta et al. 2013; Long et al. 2011; Olmedo et al. 2012). Observations from instruments like LASCO onboard SOHO have extended shock wave investigations beyond $2.5 R_{\odot}$ (Domingo et al. 1995; Vourlidas et al. 2003). While EUV observations link CMEs and EUV waves, understanding shock waves in EUV remains incomplete (Patsourakos & Vourlidas 2009; Kozarev et al. 2011). Emission measure modeling using AIA's EUV channels provides insights into temperature and density changes in the wavefront's sheath (Kozarev et al. 2011). Multi-wavelength observations from SOHO/LASCO and SDO/AIA instruments have revealed valuable information about CBF properties near the Sun (Warmuth 2015). Factors such as nearby active regions or coronal holes can distort CBF morphology, and a connection between CBFs and chromospheric disturbances known as Moreton waves has been established (Ofman & Thompson 2002; Mann et al. 2003; Piantschitsch et al. 2018; Thompson et al. 1999). In this study, I analyzed 26 CBF events up to $\sim 17 R_{\odot}$ using observations and modeling tools from the Solar Particle Radiation Environment Analysis and Forecasting–Acceleration and Scattering Transport (SPREAdFAST) framework (Kozarev et al. 2022). The study aims to characterize CBF kinematics and estimate ambient plasma properties to understand the relationships between shock and plasma parameters.

Table 2.1: List of the CBF events with their associated flares and CMEs.

ID	Event Date	Flare Start (UT)	Flare Max (UT)	Flare Class	EUV Wave Start (UT)	EUV Wave End (UT)	Source X (")	Source Y (")	CME on	V_{CME}	AW
0	2010/06/12	0:30	0:57	20	0:55	1:19	633	390	1:32	486	119
1	2010/08/14	9:38	10:05	4.4	9:30	10:08	697	-26	10:12	1205	360
2	2010/12/31	4:18	4:25	1.3	4:15	5:01	799	246	5:00	363	45
3	2011/01/28	0:44	1:03	13	0:45	1:59	949	218	1:26	606	119
4	2011/03/07	19:43	20:12	37	19:31	22:59	614	553	20:00	2125	360
5	2011/05/11	2:23	2:43	0.81	2:20	2:35	785	399	2:48	745	225
6	2011/08/04	3:41	3:57	93	3:43	4:20	546	200	4:12	1315	360
7	2011/08/08	18:00	18:10	35	17:45	18:43	812	215	18:12	1343	237
8	2012/03/07	1:05	1:14	130	0:00	0:40	-475	397	1:30	1825	360
9	2012/03/13	17:12	17:41	79	17:03	17:44	804	352	17:36	1884	360
10	2012/07/23	u	u	u	2:09	2:48	912	-243	2:36	2003	360
11	2013/04/21	u	u	u	6:35	7:35	937	181	7:24	919	360
12	2013/05/13	15:48	16:05	280	15:44	16:20	-927	186	16:08	1850	360
13	2013/05/15	1:25	1:48	120	1:06	1:50	-852	199	1:48	1366	360
14	2013/05/22	13:08	13:32	50	12:33	13:20	875	238	13:26	1466	360
15	2013/06/21	2:30	3:14	29	2:31	3:21	-869	-268	3:12	1900	207
16	2013/10/25	7:53	8:01	170	7:53	8:29	-914	-158	8:12	587	360
17	2013/12/12	3:11	3:36	0.22	3:03	3:33	750	-450	3:36	1002	276
18	2013/12/28	17:53	18:02	9.3	17:10	18:00	942	-252	17:36	1118	360
19	2014/07/08	16:06	16:20	65	16:06	16:51	-767	163	16:36	773	360
20	2014/12/05	5:28	5:37	2.1	5:42	6:21	872	-366	6:24	534	172
21	2015/05/12	2:15	3:02	2.6	2:18	2:49	960	-192	2:48	772	250
22	2015/09/20	17:32	18:03	21	17:28	18:11	660	-429	18:12	1239	360
23	2015/10/29	u	u	u	2:13	2:52	951	-167	2:36	530	202
24	2015/11/09	12:49	13:12	39	12:51	13:27	-626	-229	13:25	1041	273
25	2017/04/01	21:35	21:48	44	21:31	22:19	761	308	22:12	516	115

2.2 EUV Observations

We conducted a study utilizing data from the SOHO/ERNE instrument, focusing on proton events with energies between 17-22 MeV, spanning from 2010 to 2017. Initially, 216 events were identified, but after stringent selection criteria were applied, 133 events were excluded due to various factors such as the absence of EUV wave associations, CMEs, or flares. This left us with a final set of 26 events for analysis. The selected events (Table 2.1), previously discussed in (Kozarev et al. 2022), were further examined using imagery from the AIA instrument's EUV channel 193 Å. These images, captured at a 24-second cadence, provided the primary input for our analysis within the SPREAdFAST framework.

Detailed information about the selected events, including their start/end times, associated flares, and source locations on the solar disk, was obtained from the Heliophysics Events Knowledge (HEK) database. Notably, the mean latitude and longitude of the CBFs were calculated, along with their distribution across the solar hemispheres and quadrants. CBFs, observed as faint quasi-spherical sheaths, were primarily visible in the 193 Å channel. To analyze their evolution, sequences of base-difference images were generated for each event, allowing us to track their propagation over time (Vourlidas et al. 2003; Ontiveros & Vourlidas 2009; Kozarev et al. 2011; Ma et al. 2011).

The mean latitude and mean longitude of the CBFs were calculated as 56.35 and 378.04 arcsec, respectively. Additionally, the mean latitudes of CBFs in the northern and southern solar hemispheres were found to be 283.00 and -252.73 arcsec, respectively. As for the mean longitudes, they were -775.71 and 803.11 arcsec on the eastern and western sides, respectively.

To analyze the kinematics of CBFs, the Coronal Analysis of SHocks and Waves framework (Kozarev et al. 2017, CASHeW) was employed. This semi-automated technique involved extracting annular regions from AIA images and mapping them onto polar projections (Fig. 2.1). By tracking intensity changes along radial and lateral directions, we could measure the kinematics of the CBFs.

Furthermore, plasma parameters and modeling were performed using information retrieved from the HEK database and Nariaki Nitta's catalog of coronal waves (Nitta et al. 2013). The SPREAdFAST framework facilitated calculations of kinematics, inference of shock parameters, and determination of plasma properties for each event.

To accurately determine the positions of CBFs over time, we employed several algorithms, including Savitzky-Golay filtering (Savitzky & Golay 1964) for data smoothening and local minima/maxima ordering for identifying wave positions. Additionally, we manually specified starting and ending times for each CBF event and determined their corresponding heights above the solar limb. By analyzing intensity values, we defined the positions of CBFs at each time step, considering the front and back of

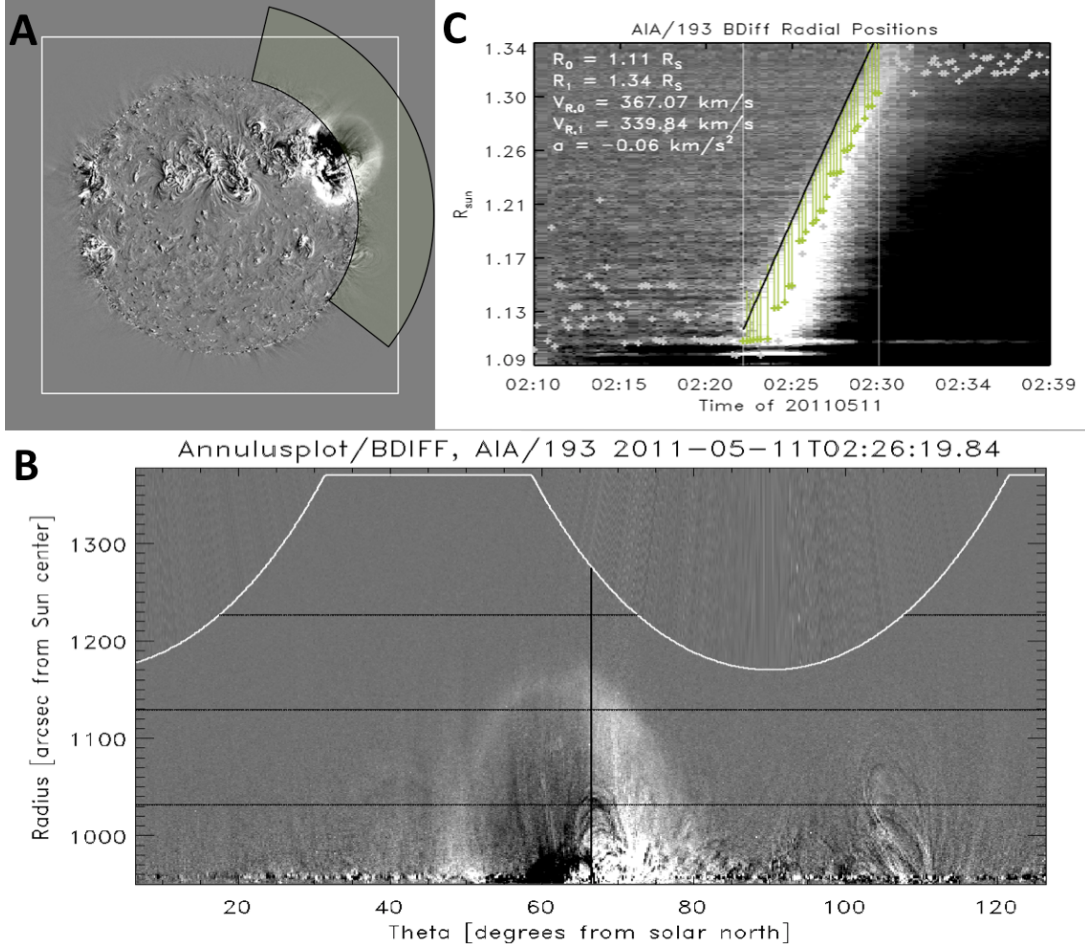


Figure 2.1: Illustration for the annulus method used to extract kinematic data from AIA images. (A) shows the full Sun disk with the relevant region highlighted for analysis (green sector). The white box outlines the AIA FOV. (B) displays the extracted annular region mapped onto polar coordinates, with the actual data extent marked by the white curve. Black lines indicate the directions used for measuring radial and lateral motions. (C) shows a stacked plot of intensity along the radial direction, with green markers highlighting intensity peaks and their corresponding distances from the CBF wavefront. The white lines represent the time interval during which the CBF is tracked within the AIA FOV. This figure is curated from (Kozarev et al. 2017).

the wave to be at 20% of the peak intensity. Furthermore, we applied mathematical techniques such as Levenberg-Marquardt least squares minimization (Markwardt 2009) and bootstrapping optimization (Efron 1979) to fit fourth-order polynomials to the wave positions, enabling measurements of speeds, accelerations, intensities, and thicknesses in both radial and lateral directions.

Finally, measurements of CBF heights and lateral positions were obtained relative to the solar disk and wavefront direction, respectively, providing comprehensive insights into the dynamics of these solar phenomena. For further reference, the HEK database¹, Nariaki Nitta’s catalog of coronal waves², and the LASCO CME Catalog³ were utilized, along with detailed summary plots available in the online SPREAdFAST catalog⁴.

2.3 Data Analysis and Methods

The Solar Particle Radiation Environment Analysis and Forecasting—Acceleration and Scattering Transport (SPREAdFAST) system, developed by Kozarev et al. (2022) and referred to as SPREAdFAST throughout this discussion, operates as a physics-based prototype for forecasting SEP events within the heliosphere. Built upon the CASHeW framework, SPREAdFAST integrates data-driven models to forecast various aspects of SEP events, including arrival times, maximum intensities, and fluxes at different locations in the inner heliosphere. These predictions play a vital role in space weather forecasting, contributing to the protection of assets owned by the European Space Agency (ESA) and aiding satellite operators in making informed decisions to mitigate the impacts of space weather on electronics and human activities in space (Kozarev et al. 2022).

The SPREAdFAST catalog offers summary plots of J-maps and kinematic data for each SEP event, as highlighted by Kozarev et al. (2022). Additionally, to ensure consistency in lateral kinematic measurements, an averaging technique is applied to data from both lateral left and right flanks, as described by the same authors. Further analysis involves the application of a Savitzky-Golay fit, as outlined in previous work by Kozarev et al. (2019), and the utilization of analytical models for CME kinematics by Gallagher et al. (2003) and Byrne et al. (2013) to extrapolate smoothed radial positions up to $\sim 17 R_{\odot}$.

Moving forward, the development of synthetic shock models (S2M) forms the next phase of the study, as mentioned by Kozarev et al. (2022). These models, operating at a 24-second cadence, are constructed based on extrapolated radial and lateral kinematic results and incorporate major and minor axes of spheroids representing compressive waves. The shock surface is delineated from the onset of the CBF until its nose reaches $10 R_{\odot}$ and then extended up to $30 R_{\odot}$ utilizing results from the Magnetohydrodynamic Algorithm outside a Sphere (MAS) synoptic coronal model.

The methodology for estimating shock density jump is detailed by Kozarev et al. (2017), involving the calculation of differential emission measure (DEM) during and before the event at each shock crossing and timestep. This approach, informed by Cheung et al. (2015), provides insights into the variation in density across shock structures. Notably, while the density jump within the AIA FOV typically remains below 1.2, regions beyond observational limits are assigned a value of 1.2, assuming the presence of weak shocks. To facilitate analysis, the synthetic shock model is segmented into distinct regions—the cap representing the shock nose, Zone 1, and Zone 2 representing the shock flanks—as explained by Kozarev et al. (2022). This segmentation aids in the examination of plasma parameter distributions across different sectors of the shock surface, as depicted in Figure 2.2.

2.4 CBF Kinematics and Geometric Modeling: Case Study May 11, 2011

In this section, I analyze a case study event in the low corona region and investigate plasma parameters along shock-crossing magnetic field lines in the AIA FOV.

2.4.1 Event Context

The eruption occurred on May 11, 2011, at around 02:20 UT (Fig. 2.3), originating from an active region in the northwestern sector (N18W52). It involved a massive shock wave propelled by a fast

¹HEK Database: www.lmsal.com/isolsearch

²Nariaki Nitta’s Catalog: https://lmsal.com/nitta/movies/AIA_Waves/index.html

³LASCO CME Catalog: https://cdaw.gsfc.nasa.gov/CME_list/

⁴SPREAdFAST Catalog: <https://spreadfast.astro.bas.bg/catalog/>

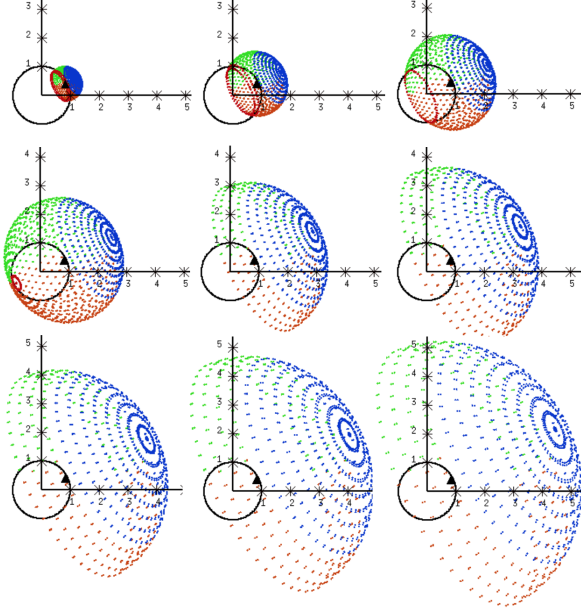


Figure 2.2: Synthetic shock model divided into three segments; the cap zone in blue and the flank zones are in red and green.

partial-halo CME, with a linear speed of 745 km s^{-1} , a 2^{nd} -order speed at $20 R_{\odot}$ of 776 km s^{-1} , and an acceleration of 3.3 m s^{-2} . The eruption was accompanied by a weak B8.1 solar flare and an eruptive filament observed by the SDO/AIA instrument. Additionally, a type II radio burst was associated with the eruption, observed by the Learmonth spectrogram. Proton fluxes near 1 AU showed an increase, and an SEP event was detected at Earth with onset time of 03:39 UT and a J_p of $0.0133 \text{ protons}/(\text{cm}^2 \text{ s sr MeV})$ in the energy channel 17-22 MeV (Miteva et al. 2016, 2017). J_p is the peak proton intensity after subtracting the pre-event level.

2.4.2 Low Corona Part

To investigate the kinematics of the CBF event, I employed the CASHeW module within the SPREAd-FAST framework. The shock wave's asymmetrical evolution is detailed, along with its morphological changes over time. The average speeds and accelerations for the radial and lateral directions are provided (Fig. 2.4), along with a comparison of wave thickness between flanks. The shock surface is divided into segments for further analysis (Fig. 2.2). Table 2.2 provides a summary of the statistical results, and the results for the three segments are summarized in Table 2.3. Moreover, shock-crossing magnetic field lines during this event were investigated in (Kozarev et al. 2022), with key plasma parameters analyzed up to $10 R_{\odot}$. The aspect ratio of the coronal wave's geometry is discussed, along with changes in shock-field angle and magnetic field amplitude over time and radial distance.

2.4.3 Middle/Outer Corona Part

Complementary measurements from the SOHO/LASCO instrument⁵ expand the analysis of EUV waves' kinematics in the middle/outer corona. The height-time profile of the CME leading edge associated with the coronal wave is examined, employing fitting models of Gallagher et al. (2003) and Byrne et al. (2013) to analyze the data (Fig. 2.5). Insights into the wave's acceleration and speed variation over time and distance from the Sun are provided (Fig. 2.6).

2.5 Statistical Study

I conduct a thorough statistical analysis of coronal wave events observed in the AIA and LASCO FOVs, focusing on kinematic characteristics and plasma parameters.

⁵LASCO CME Catalog: https://cdaw.gsfc.nasa.gov/CME_list/

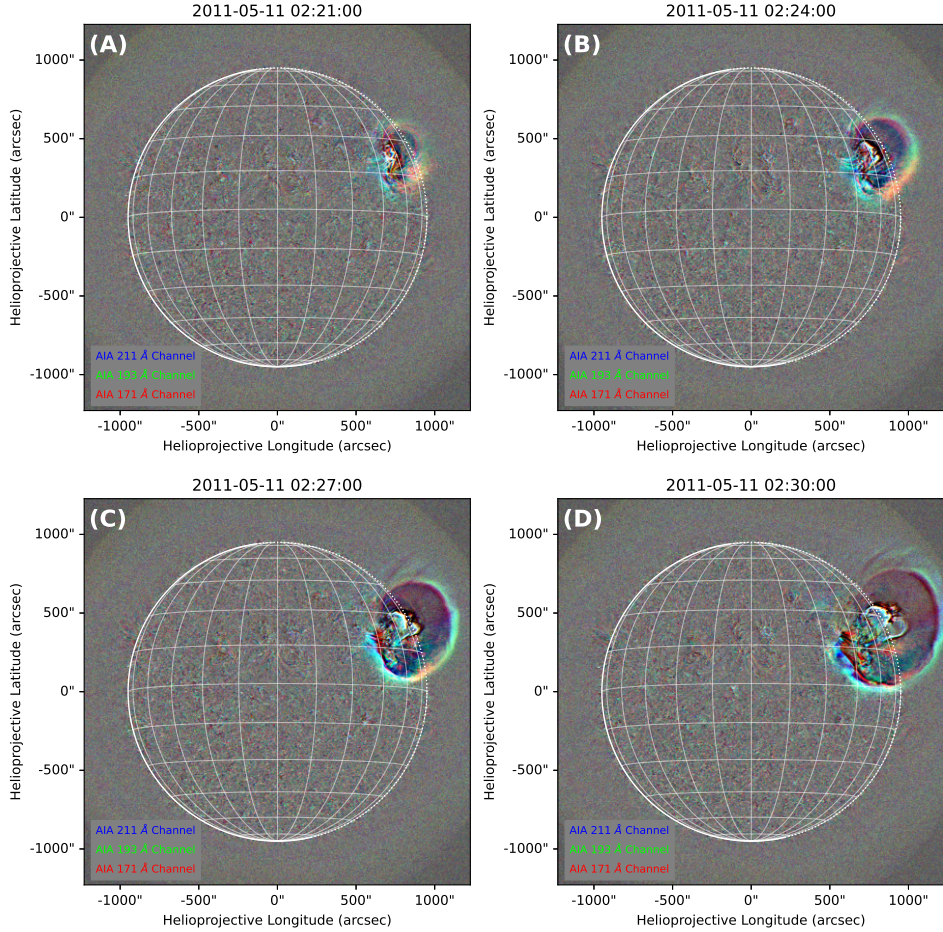


Figure 2.3: AIA running-difference images capture a coronal wave evolving over 9 minutes near the Sun's western limb, exhibiting markedly changing intensity and structure as observed in 171, 193, and 211 Å.

Table 2.2: Mean values and their standard deviation of the wave parameters in the radial direction and the lateral direction for the left and right flanks, at the front, peak, and back sides of the wave for the event occurred on May 11, 2011, in the SDO/AIA FOV.

Parameter	Direction	Front	Peak	Back
$\langle speed \rangle \text{ km s}^{-1}$	Lat. Left	218.46 ± 9.04	297.46 ± 5.45	293.94 ± 9.04
	Radial	427.46 ± 51.85	433.11 ± 82.86	400.81 ± 83.78
	Lat. Right	494.69 ± 0.00	509.25 ± 1.02	498.97 ± 9.21
$\langle accel. \rangle \text{ m s}^{-2}$	Lat. Left	-414.62 ± 227.23	-401.46 ± 164.62	-385.77 ± 227.23
	Radial	147.41 ± 1009.19	758.97 ± 1287.65	485.38 ± 1365.80
	Lat. Right	-415.04 ± 0.00	-209.81 ± 22.32	-266.68 ± 250.80
$\langle intensity \rangle \text{ DN}$	Lat. Left		250.60 ± 5.90	
	Radial		403.34 ± 143.30	
	Lat. Right		489.04 ± 2.86	
$\langle thickness \rangle R_{\odot}$	Lat. Left		0.07 ± 0.00	
	Radial		0.04 ± 0.01	
	Lat. Right		0.09 ± 0.00	

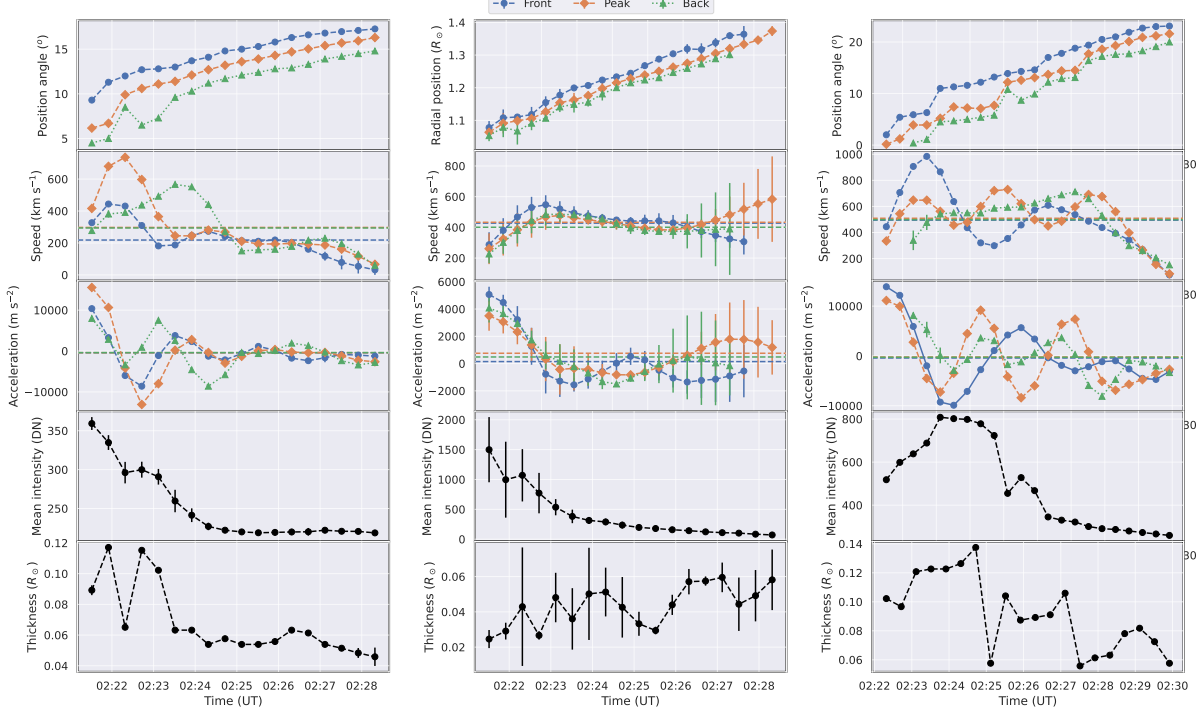


Figure 2.4: Time-series kinematics of the CBF parameters for the front, peak, and back positions in the AIA FOV, with measurement uncertainties shown as small bars over the data points. The horizontal lines in the speed and acceleration panels denote the mean speeds and accelerations for the wave front, peak, and back with respective colors. The left and right columns represent the lateral kinematic measurements in the left and right flanks of the wave, respectively. The middle column represent the kinematic measurements in the radial direction.

Table 2.3: Mean, median, and standard deviation of the shock parameters output, from the interaction of the S2M spheroid with the MAS MHD model results, for the shock's cap and flanks and for the whole shock surface, for the event on May 11, 2011.

Segment	Parameter	Statistics		
		Mean	Median	Stdv
All	V_{SHOCK} km s ⁻¹	577.77	578.39	72.79
	θ_{BN} °	70.06	0.63	44.83
	B_{MAG} G	0.046	0.038	0.070
	Density Jump	1.193	1.188	0.185
Cap	V_{SHOCK} km s ⁻¹	555.18	550.86	42.46
	θ_{BN} °	19.37	3.61	25.51
	B_{MAG} G	0.046	0.036	0.070
	Density Jump	1.193	1.188	0.015
Zone 1	V_{SHOCK} km s ⁻¹	613.69	609.32	59.42
	θ_{BN} °	6.46	0.21	50.92
	B_{MAG} G	0.045	0.045	0.066
	Density Jump	1.190	1.187	0.008
Zone 2	V_{SHOCK} km s ⁻¹	631.37	614.23	73.07
	θ_{BN} °	0.10	0.51	10.61
	B_{MAG} G	0.046	0.029	0.071
	Density Jump	1.194	1.188	0.016

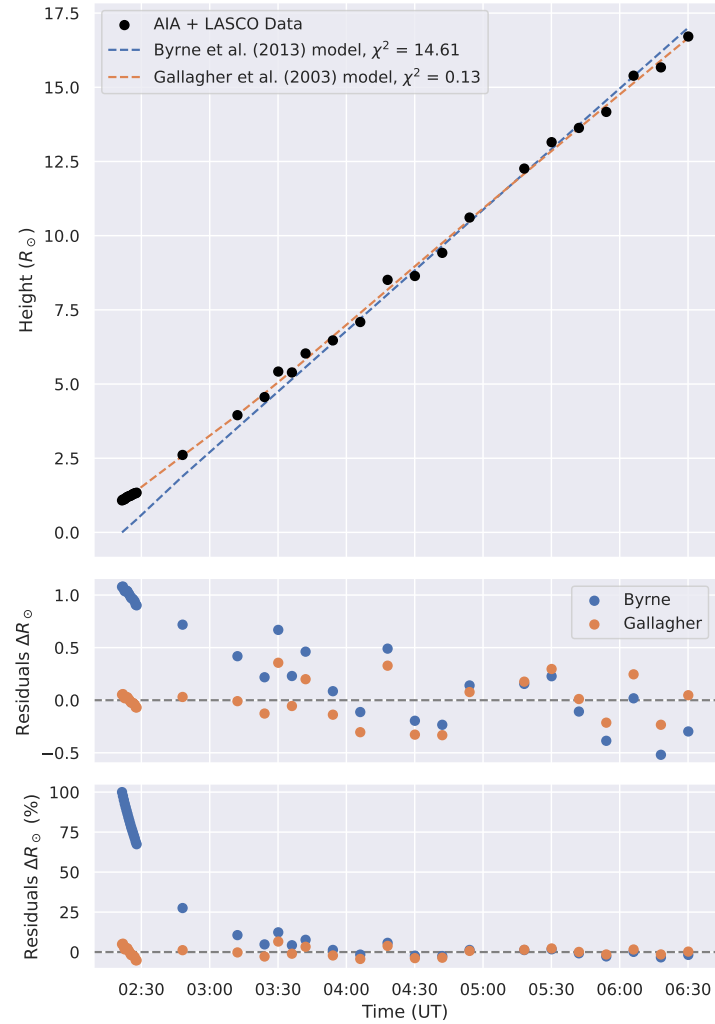


Figure 2.5: Top panel – Height-time profile compiled from AIA and LASCO measurements for the event occurred on May 11, 2011, fitted with two CME kinematics models from the photosphere up to $17 R_{\odot}$. Middle panel – Difference between the fitting and the real observations. Bottom panel – Relative residuals in %.

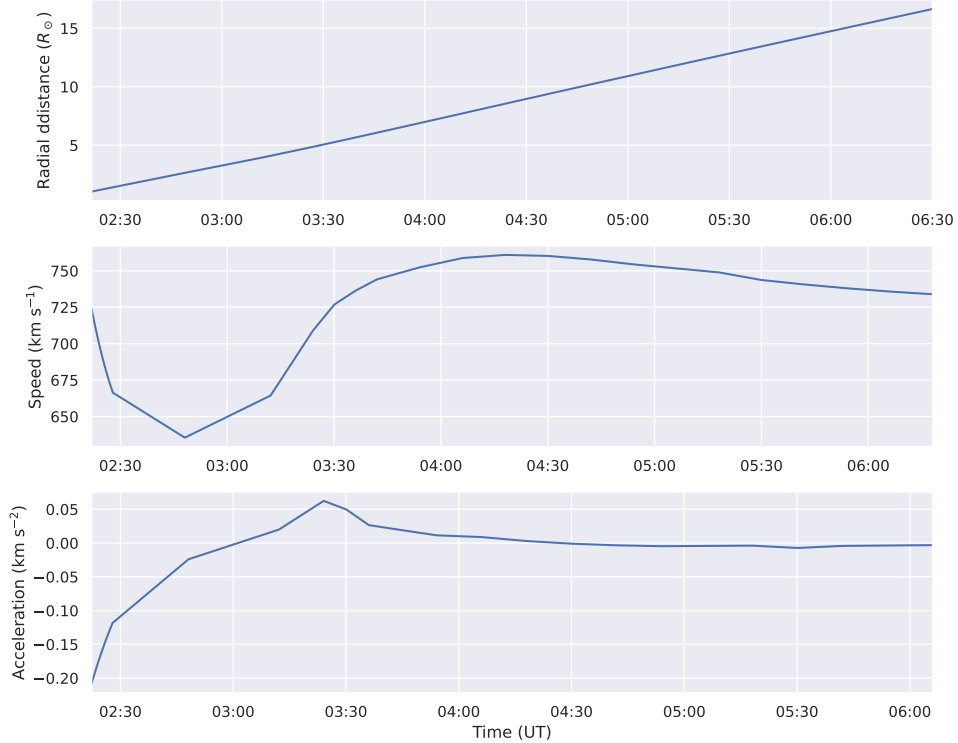


Figure 2.6: Extrapolated radial kinematics for the event occurred on May 11, 2011, based on the ballistic model of Gallagher et al. (2003) up to $17 R_{\odot}$.

Table 2.4 summarizes statistical parameters related to shock characteristics, such as wave speed, intensity, and thickness in the AIA FOV. Analysis reveals higher speeds, accelerations, lower mean intensities, and thickness in the radial direction compared to the lateral direction, suggesting early elongation of waves near the Sun. Figure 2.7 illustrates EUV waves' kinematics evolution in the AIA FOV, showing parameter distributions as a function of distance for shock speed, acceleration, wave intensity, and thickness in radial and lateral directions. Speed and intensity decline with distance due to momentum loss and decreasing plasma densities. All dynamic spectra for individual events are accessible on the SPREAdFAST catalog webpage⁶.

Table 2.4: Statistics of the EUV wave kinematics in the SDO/AIA FOV for the 26 events. LL and LR refer to the lateral left and right flanks, respectively. Rad refer to the radial front direction.

Aspect ratio	Speed (km s^{-1})			Accel. (km s^{-2})			Intensity (DN)			Thickness (R_{\odot})			
	LL	Rad	LR	LL	Rad	LR	LL	Rad	LR	LL	Rad	LR	
Max	2.00	1574.81	2053.73	983.58	28.19	81.01	13.89	1348.87	2431.95	1498.45	9.600	0.185	6.100
Min	0.84	2.11	40.30	2.30	-35.24	-81.01	-9.89	0.53	0.17	150.30	0.027	0.018	0.022
Mean	1.87	316.17	413.60	264.50	-0.15	0.98	0.13	438.99	681.46	442.46	0.715	0.059	0.231
Median	2.00	284.77	349.32	216.32	0.03	0.37	0.11	337.96	425.23	389.06	0.102	0.055	0.076
Stdv.	0.33	261.01	336.11	191.13	5.53	11.08	2.05	292.26	592.78	227.10	1.721	0.030	0.776

Histograms in Figure 2.8 depict correlations between shock-field angle "THBN", coronal magnetic field "BMAG", plasma density "DENSITY" Alfvén speed "VA", shock speed, and shock density jump "SHOCKJUMP". Moderate positive correlations exist between magnetic field and density, and between magnetic field and Alfvén speed, suggesting common underlying physical processes. A negative correlation between magnetic field and shock density jump implies stronger magnetic fields associate with smaller density jumps across shock surfaces, possibly due to magnetic field pressure resisting plasma compression or faster Alfvén waves mitigating density jumps. Further exploration is warranted to establish definitive connections and parameterize shock density jumps.

⁶SPREAdFAST Catalog: <https://spreadfast.astro.bas.bg/catalog/>

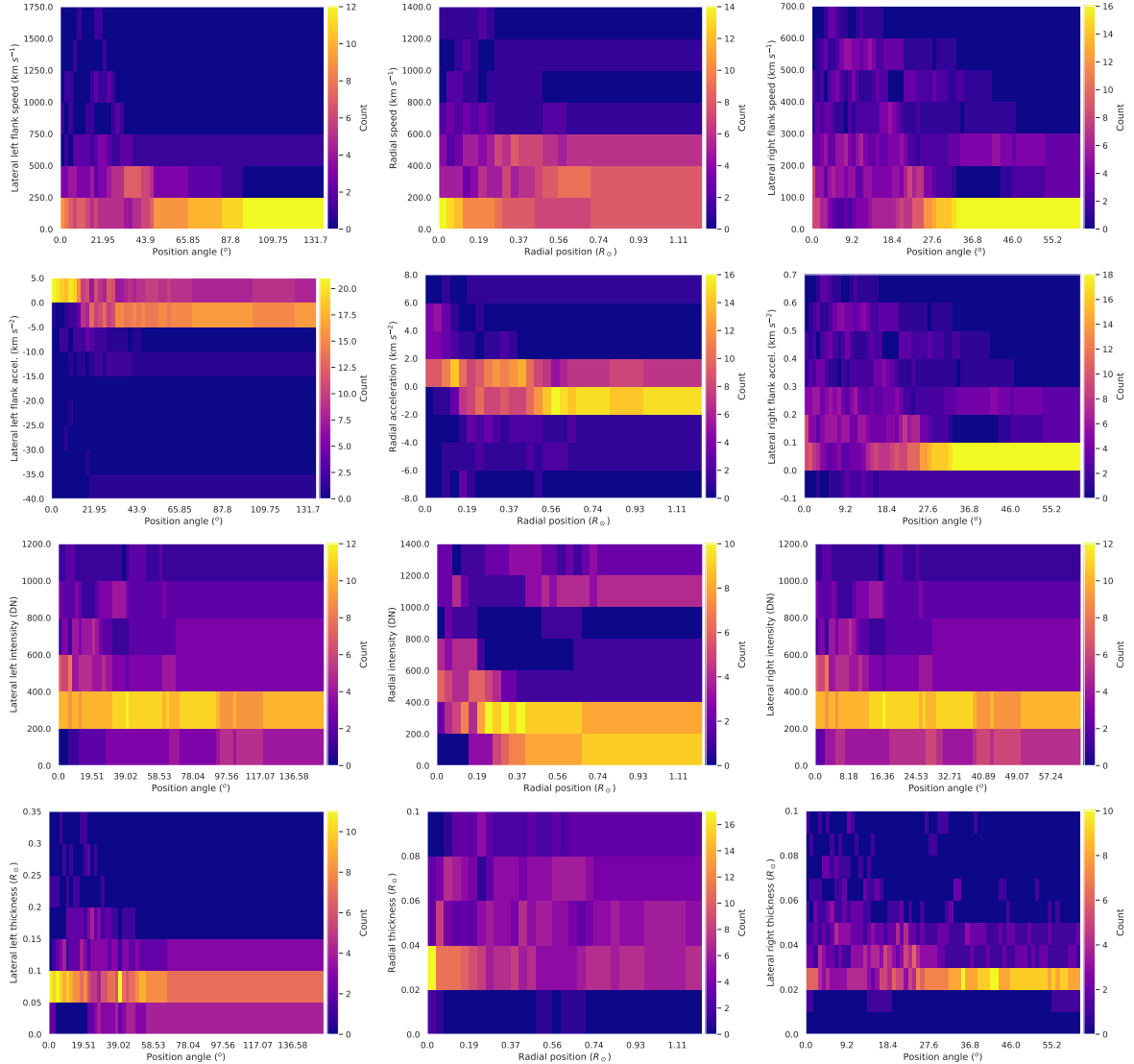


Figure 2.7: Dynamic spectra of the EUV waves kinematics in the AIA FOV. The panels from the top to the bottom are the wave speeds, acceleration, mean intensity, and thickness. The left column is for the lateral left flank, the central column is for the radial direction, and the right column is for the lateral right flank.

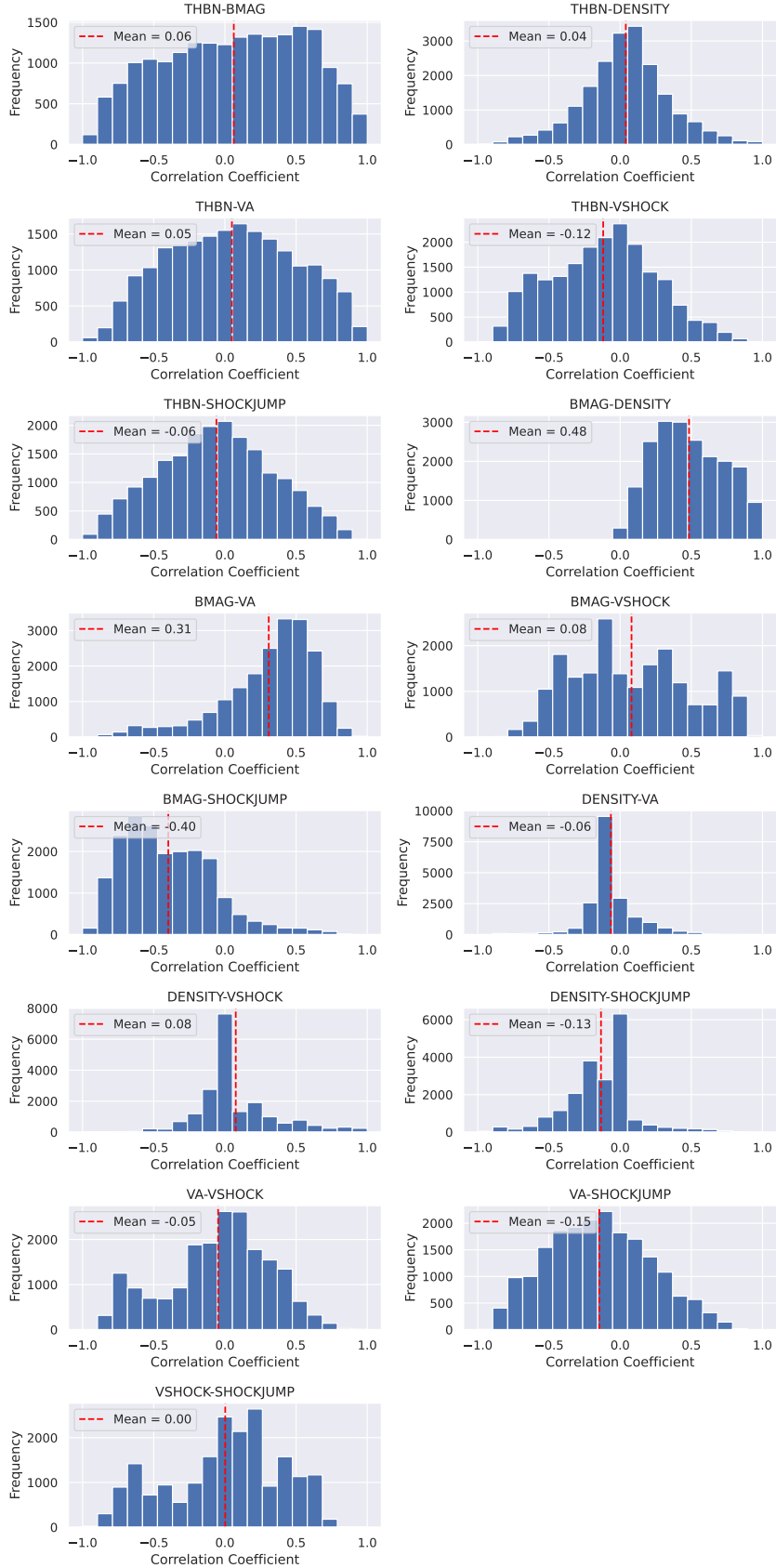


Figure 2.8: Histograms of along-field-lines model plasma parameters in the solar corona for all the 26 events. The vertical dashed red lines are the mean values.

2.6 *Wavetrack*: Automated Recognition and Tracking of Solar Eruptions

2.6.1 Overview

The principal drivers of SEPs are acknowledged to be CME-driven shocks within the corona and interplanetary space. This acceleration primarily occurs through the diffusive shock acceleration (DSA) and shock drift acceleration (SDA) processes (Reames 2021). Efforts have focused on characterizing SEP acceleration under ideal conditions (Vainio & Laitinen 2008; Sokolov et al. 2009; Kozarev et al. 2013), with recent models incorporating observational data (Vourlidas et al. 2012; Kwon et al. 2014; Kozarev et al. 2015, 2019).

Understanding SEP acceleration requires comprehensive knowledge of CME-shock interactions with three-dimensional coronal fields (Rouillard et al. 2016). Modeling DSA necessitates deducing shock front shapes from observations, considering the impact of the local magnetic field-shock angle (Guo & Giacalone 2013). EUV imaging, facilitated by instruments like STEREO (Wuelser et al. 2004) and SDO/AIA (Lemen et al. 2012), enables shock characterization, supporting time-dependent modeling of SEP acceleration (Kozarev & Schwadron 2016; Kozarev et al. 2017, 2019). Solar feature detection, including EUV waves, employs automated techniques (Aschwanden 2010; Pérez-Suárez et al. 2011), with challenges in wave recognition and tracking (Podladchikova & Berghmans 2005; Verbeeck et al. 2014; Long et al. 2014; Ireland et al. 2019).

Wavetrack, a Python library, addresses these challenges by offering flexible solar feature detection and tracking (Stepanyuk et al. 2022). It integrates wavelet transforms and filtering, enabling multiscale data representation (Starck & Murtagh 2002) and Δ trous wavelet transform (Akansu 1991; Holschneider et al. 1989), essential for tasks like CME tracking.

Various techniques contribute to solar image analysis, including wavelet transform, image filtering, feature detection algorithms, machine learning, and solar feature tracking.

- **Wavelet Transform:** The Δ trous wavelet transform facilitates multi-scale data representation, aiding feature extraction in solar image analysis.
- **Image Filtering:** Various techniques enhance specific features within solar images, aiding in phenomena detection.
- **Feature Detection Algorithms:** Automated algorithms improve solar feature identification efficiency across different observations.
- **Machine Learning:** Integration of machine learning techniques such as Convolutional Neural Networks (CNNs) and Generative Adversarial Networks (GANs) enriches solar image analysis capabilities.
- **Solar Feature Tracking:** Tracking algorithms monitor feature evolution over time, crucial for understanding solar processes.

Observations from SDO/AIA, particularly in 193 and 211 \AA wavelengths, are instrumental in studying solar dynamic features, facilitating CBF analysis and tracking.

2.6.2 Image Filtering Techniques

Image filtering techniques, including thresholding, wavelet decomposition, and segmentation, were central to the method. Initial thresholding narrowed the dynamic range of base difference images, focusing on the object of interest. Following thresholding, the base difference images underwent Δ trous wavelet decomposition into multiple scales. Each wavelet coefficient was then thresholded relative to the statistical distribution of pixel intensities at each decomposition level. Segmentation produced object masks for each time step, which were subsequently multiplied by the original data to reveal intensity variations within the object.

Tailored approaches were employed due to variations in statistical distributions of pixel intensities between base and running difference images. Base difference images focused on specific segments containing the object of interest, such as a CBF, while running difference images, used for eruption initiation identification, were dependent on specific features and objects observed.

The \AA trous wavelet transform, providing a multi-scale data representation, significantly contributed to solar image recognition and tracking. This hierarchical decomposition facilitated the extraction of specific objects and their masks from imaging observations, aiding in their tracking and temporal analysis. It enhanced the visibility of faint features like EUV waves, offering a versatile framework applicable to various solar phenomena across different wavelengths, thus serving as a valuable tool for analyzing CME shock waves and filaments.

The study introduced the Wavetrack package, an automated tool for detecting and tracking dynamic coronal features in solar observations. By utilizing wavelet decomposition, feature enhancement, filtering, and object recombination, Wavetrack identified and tracked features such as CBFs and eruptive filaments. This Python framework, adaptable to both on-disk and off-limb features, facilitates tracking of features evolving over time.

2.6.3 Wavetrack for Coronal Wave and Filament Tracking

Wavetrack employed wavelet decomposition, feature enhancement, and filtering for tracking coronal waves. The method enhanced faint features like EUV waves using the \AA trous wavelet decomposition. Automated feature recognition, including intensity thresholding and segmentation, isolated coronal wave features, generating time-dependent pixel masks for both on-disk and off-limb features.

For filament tracking, Wavetrack utilized wavelet decomposition, feature recognition, object mask generation, and image recombination. The method identified different scales of features and enhanced them for tracking. Object masks isolated filament features at each time step, and image recombination produced final feature maps. Image choice, such as inverted AIA 193 \AA images, depended on source data and filament velocity.

2.6.4 Fourier Local Correlation Tracking (FLCT)

The study employed the FLCT model to determine solar feature velocities, utilizing the FLCT method. FLCT analyzed consecutive solar images and tracked feature motion over time using object masks from Wavetrack. The output provided detailed maps of instantaneous velocity, aiding in understanding solar feature expansion and evolution.

The study integrated advanced image processing techniques, including wavelet transform, filtering, feature detection algorithms, and machine learning, for comprehensive solar observation analysis. Wavetrack emerged as a versatile tool, particularly valuable for dynamic coronal feature tracking, offering significant insights into solar dynamics.

2.6.5 Results

The study showcases the versatility of the Wavetrack package through several examples:

1. **May 11, 2011 event:** Wavetrack algorithm tracked an erupting filament and its associated coronal bright front (CBF), revealing their relationship using AIA 193 \AA observations.
2. **September 29, 2013 event:** Wavetrack monitored a large-scale filament eruption, consistently tracking features on the solar disk and corona.
3. **December 12, 2013 event:** Wavetrack analyzed driven and non-driven regions of a CBF, revealing its relation to eruptive features.
4. **June 07, 2011 event:** Wavetrack observed significant radial speed variations and stable angle changes during a compressive front event.

Focusing on the May 11, 2011 event accompanied by a CBF, the methodology was applied to three events observed by AIA (Kozarev et al. 2015, 2017). Wavetrack adeptly tracked CBF evolution both on the solar disk and off the limb, maintaining performance despite pixel distribution and intensity differences. The application facilitated detailed study of CBF shapes and intensity distributions, separate from the broader corona. Wavetrack effectively segmented CBF objects under different activity states, highlighting its capability to track multiple separate parts of the same feature.

Wavetrack was used to isolate and study CBF and filament kinematics using the FLCT method. Figure 2.9 shows FLCT results of the May 11, 2011 event, revealing uneven expansion of the CBF from the central source. The combined approach elucidated dynamic behavior not discernible from intensity

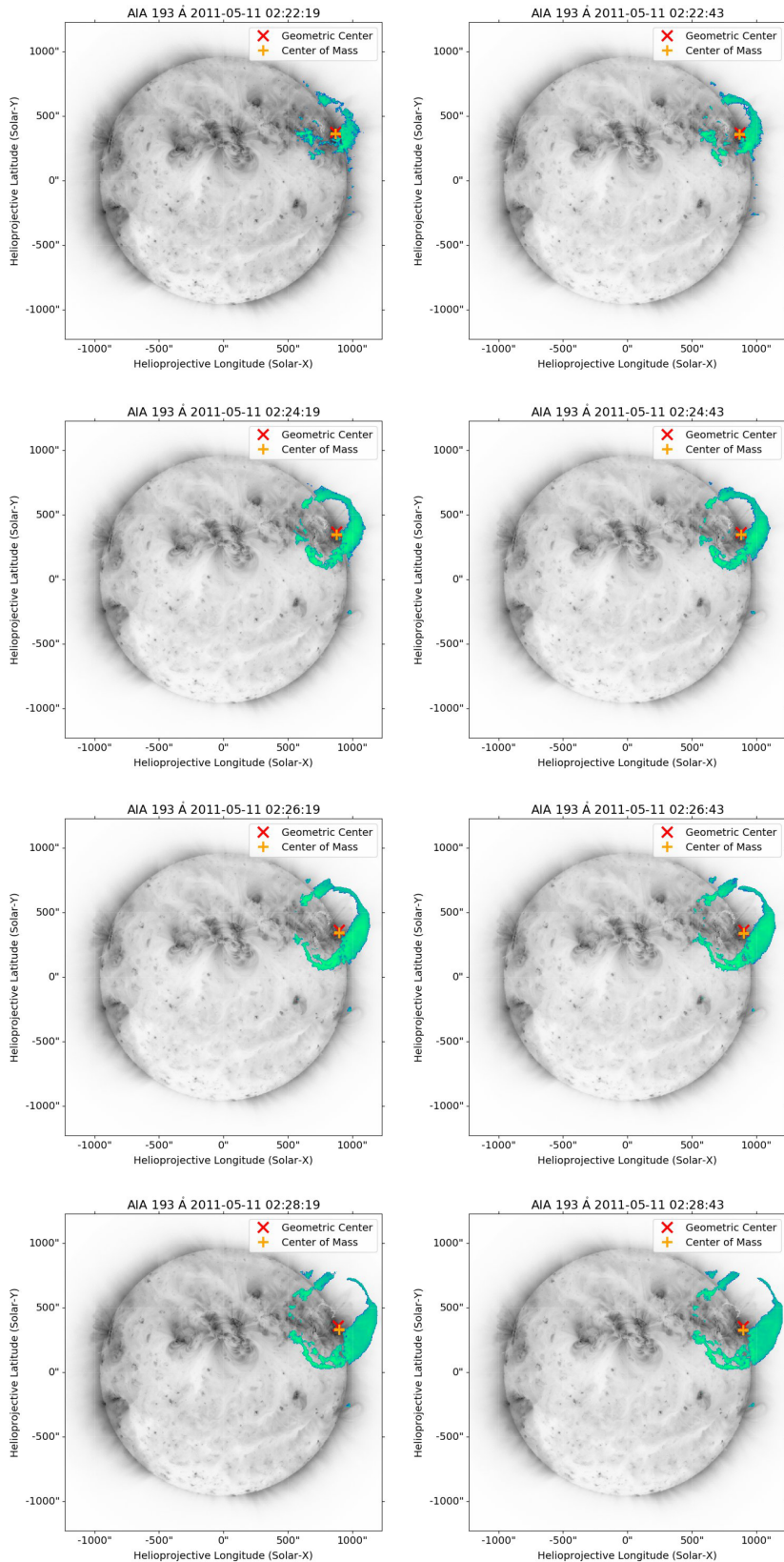


Figure 2.9: Wavetrack images of a May 11, 2011 eruption, with CBF mask applied. Four image pairs shown, separated by 2 minutes, to track CBF over time. Credit goes to Stepanyuk et al. (2022).

observations alone. Figure 2.10 displays the direction and speed of each CBF region. It reveals uneven expansion, with the thinnest part, strongly driven by the erupting filament, moving fastest. This nuanced insight, inaccessible through intensity observations alone, highlights the value of our combined Wavetrack and FLCT approach in understanding coronal feature dynamics. Figure 2.11 depicts thorough analysis of CBF centers of mass (CM) and geometric centers (GC), illustrating their positional and speed variations over time. These findings provide valuable insights into CBF dynamics during the specified event.

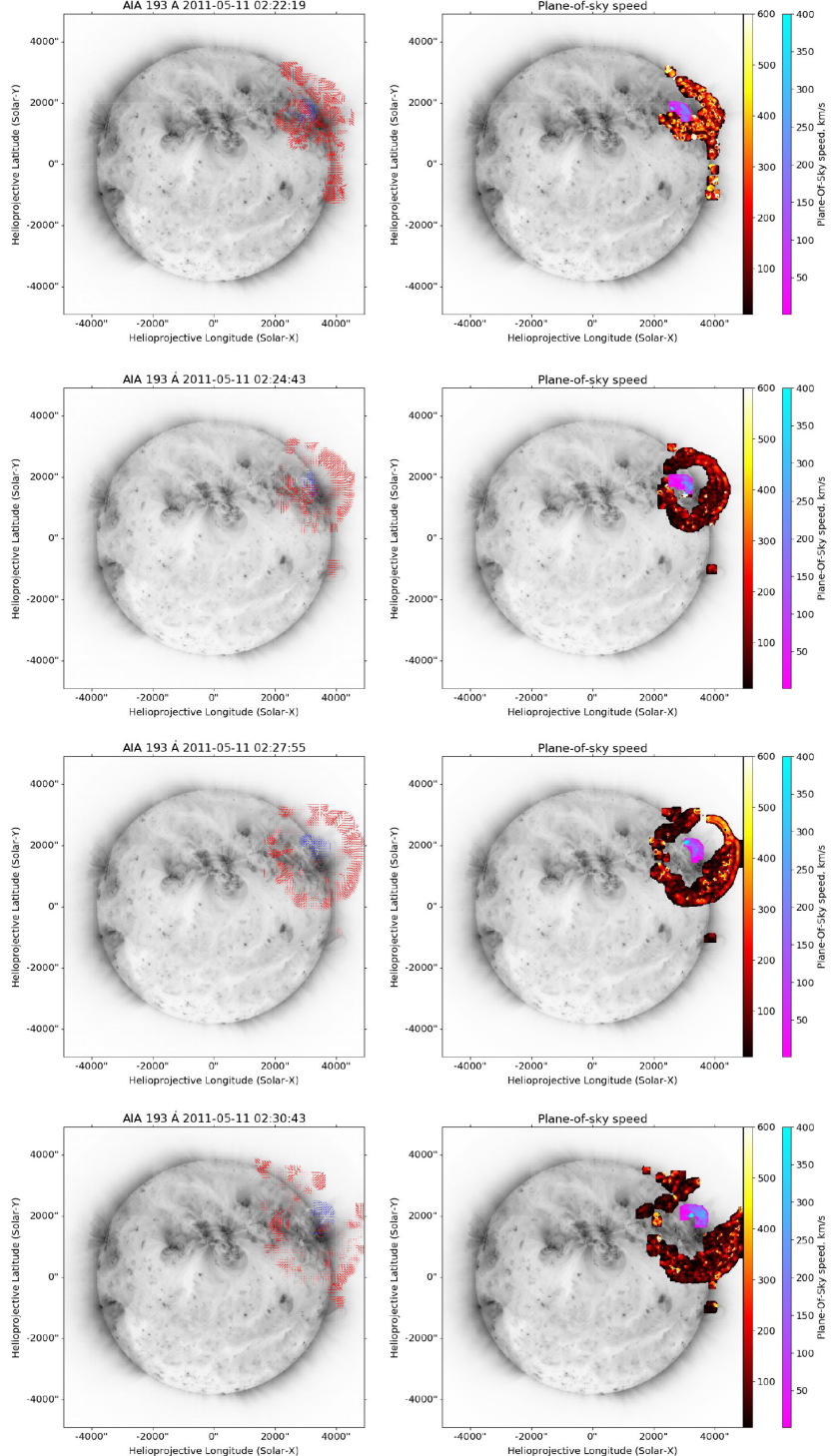


Figure 2.10: FLCT model output for four image pairs from Fig. 3. Left: the plane-of-sky velocity vectors. Right: plane-of-sky speed. Credit goes to Stepanyuk et al. (2022).

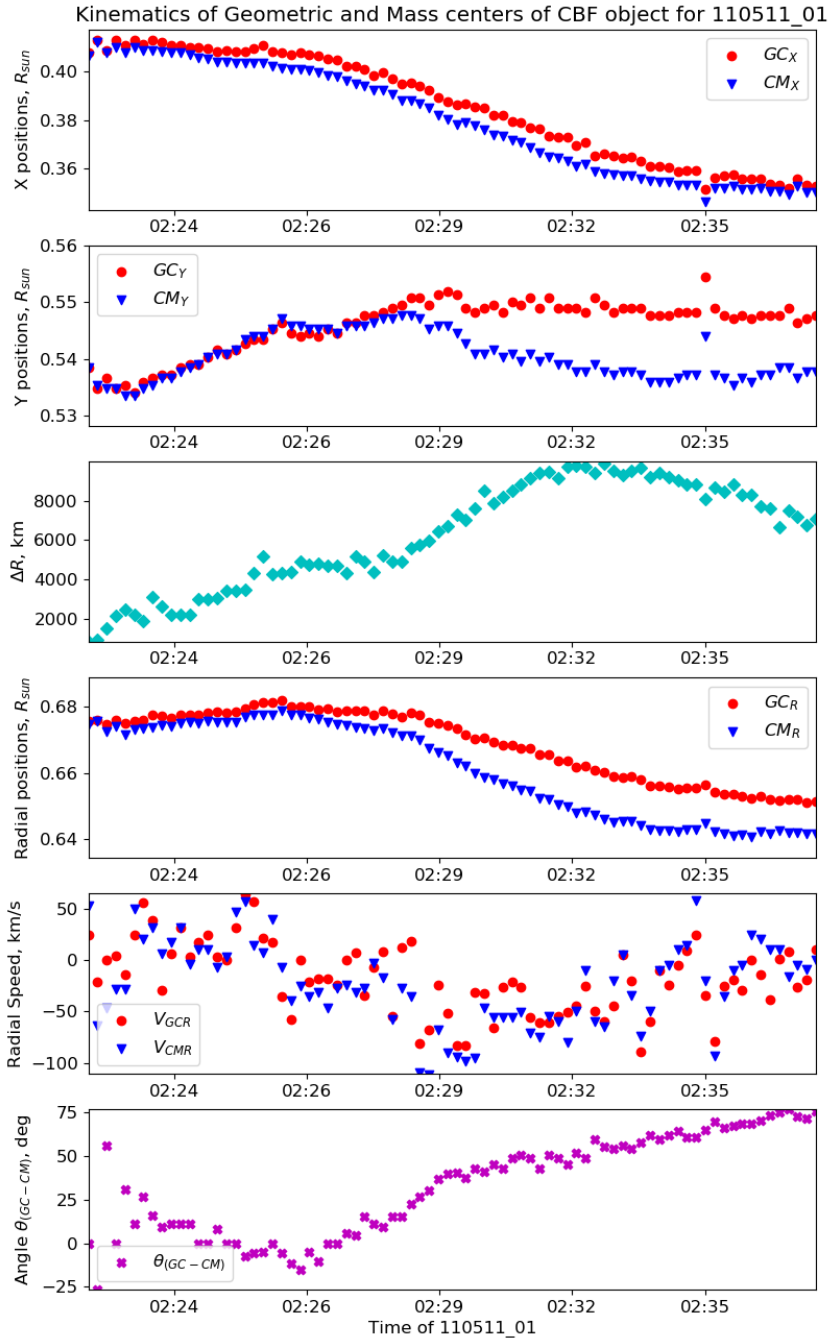


Figure 2.11: Analysis of the center of mass and geometric centers' motion during the May 11, 2011 event. The different rows present the X-, Y-, and R- positions for both GC and CM, the distance between GC and CM in km , and the angle between these two points over time. Credit goes to Stepanyuk et al. (2022).

2.7 Geomagnetic Storms: CME Speed De-Projection vs. In Situ Analysis

This study, led by Miteva et al. (2023), examines the relationship between geomagnetic storm (GS) intensity and solar/interplanetary phenomena. Using the *PyThea* framework, we reconstruct 3D geometry of geo-effective CMEs and compare on-sky and de-projected speed values, employing spheroid, ellipsoid, and graduated cylindrical shell (GCS) models. We investigate parameters of GS-associated phenomena, finding that fast CME speeds combined with specific magnetic structure orientations are indicative of GS strength. Accurate estimations of geometry, direction, and de-projected speeds are crucial for GS forecasting in space weather prediction schemes.

2.7.1 Overview

Solar eruptive events such as CMEs and solar flares (SFs) influence space weather, with electromagnetic radiation preceding energetic particles and CME plasma clouds (Fletcher et al. 2011; Webb & Howard 2012; Klein & Dalla 2017; Temmer 2021; Malandraki & Crosby 2018; Gopalswamy 2022). Geomagnetic storms (GSs) occur due to interactions between solar wind plasma and Earth's magnetosphere, facilitated by magnetic reconnection during events like CME impacts (Dungey 1961; Akasofu 1981; Echer & Gonzalez 2022; Gonzalez et al. 1994; Saiz et al. 2013; Lakhina & Tsurutani 2016). Fast CMEs cause intense GSs, affecting technology and inducing disruptions in near-Earth space (Tsurutani et al. 1997; Zhang et al. 2007; Wu & Lepping 2016; Borovsky & Denton 2006; Pulkkinen 2007).

However, single spacecraft observations limit accurate CME speed estimations due to projection effects (Paouris et al. 2021; Kouloumvakos et al. 2022). Previous studies found no clear correlation between GS intensity and solar flare/CME parameters (Samwel & Miteva 2023), highlighting the need for reliable early warnings based on solar or near-Sun measurements. Accurate prediction of CME impact on Earth requires understanding their directionality and geometry, crucial for maximizing forecast lead time (Kay & Gopalswamy 2018; Vourlidas et al. 2003; Jackson et al. 2010).

Improving reconstruction techniques to correct projection effects enhances CME propagation understanding and forecasting (Thernisien et al. 2009; Mierla et al. 2010; Wood et al. 2010; Thernisien 2011). Existing CME propagation models exhibit discrepancies between 2D and 3D speeds and widths (Odstrcil et al. 2004; Xie et al. 2004; Vršnak et al. 2013; Pomoell & Poedts 2018; Jang et al. 2016; Verbeke et al. 2022). This study focuses on deducing CME directionality and near-Sun speeds using the *PyThea* framework (Kouloumvakos et al. 2022), analyzing geo-effective cycle 24 CMEs and their correlations with GS intensity and interplanetary parameters.

The event selection process identified 25 significant GSs within Solar Cycle 24 (SC24) and associated them with potential IP and/or solar phenomena. This involved temporal associations with IP and ICME events, CMEs, and solar flares. Various databases and catalogs were utilized for this analysis (Gonzalez et al. 1994; Gopalswamy et al. 2022b; Qiu et al. 2022; Besliu-Ionescu et al. 2022; Abe et al. 2023; Zhang et al. 2007; González et al. 2007; Gopalswamy et al. 2008; Echer et al. 2013; Manu et al. 2022).

Utilized databases and catalogs include the GS database Kyoto⁷, SF database (GOES)⁸, CME catalog (SOHO-LASCO)⁹, ICME Wind and ACE databases^{10, 11}, and IP shock database (Wind)^{12, 13}. These resources were accessed for relevant data retrieval and analysis (Selvakumaran et al. 2016).

2.7.2 PyThea 3D De-Projection Tool

This investigation employs the *PyThea* online tool for 3D reconstruction of CMEs and shock waves (Kouloumvakos et al. 2022), utilizing spheroid, ellipsoid, and GCS models. Two independent observers conduct fitting procedures. Figure 2.12 illustrates fits for event E03, revealing observer bias in structure alignment with the model, potentially leading to CME width overestimation. However, despite this bias, overall results for event E03, including directivity and speed, remain minimally impacted, though discrepancies may arise among different observers.

⁷<https://wdc.kugi.kyoto-u.ac.jp/dstdir/index.html>

⁸<http://ftp.swpc.noaa.gov/pub/warehouse/>

⁹LASCO CME Catalog: https://cdaw.gsfc.nasa.gov/CME_list/

¹⁰https://wind.nasa.gov/ICME_catalog/ICME_catalog_viewer.php

¹¹<https://izw1.caltech.edu/ACE/ASC/DATA/level3/icmetable2.htm>

¹²<http://www.ipshocks.fi/database>

¹³https://lweb.cfa.harvard.edu/shocks/wi_data/

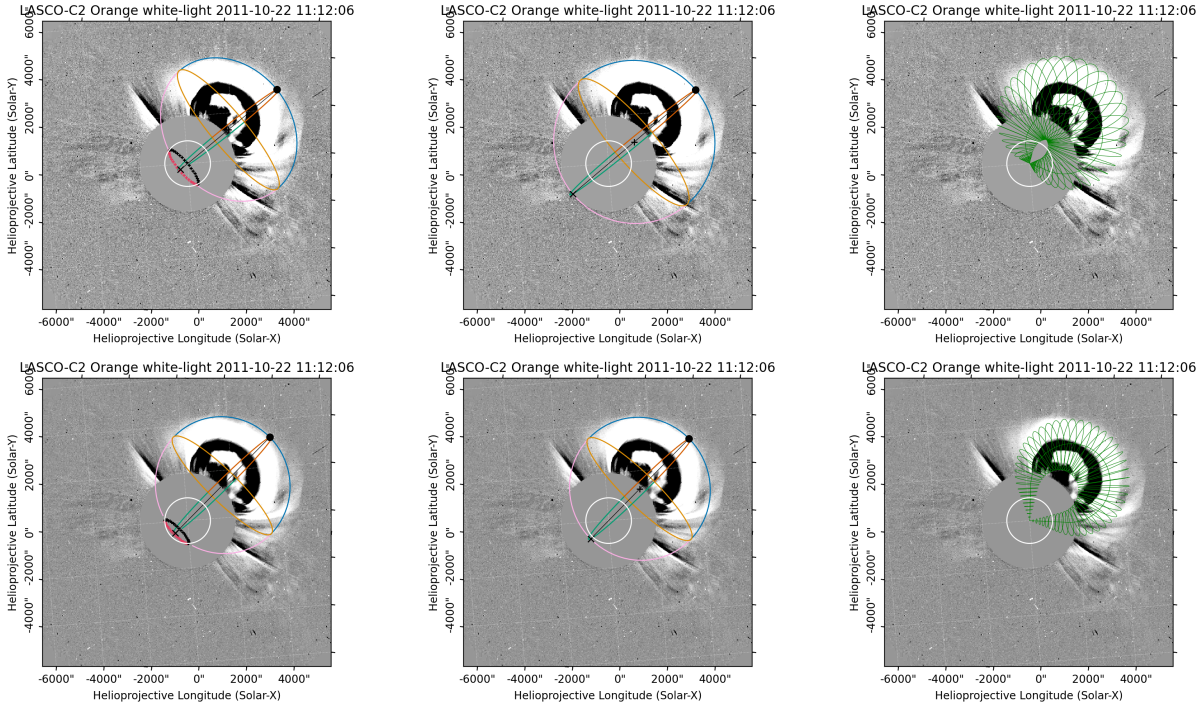


Figure 2.12: 3D reconstructions of a CME (E03) using the spheroid, ellipsoid, and GCS model from the PyThea tool performed by observers 1 and 2 (top and bottom row, respectively). Credit goes to Miteva et al. (2023).

In five cases (E05, E11, E17, E18, E22), attempts to identify SFs or CMEs were unsuccessful, while in six additional cases, SF specifications were unattainable. Events with uncertain CME origins were excluded from subsequent 3D analyses. For example, the unique orientation of a double CME in case E07 rendered its de-projection unfeasible, leading to its exclusion. Similarly, in seven cases (E12, E14–E16, E19, E23, E25), data retrieval issues from both spacecraft led to their omission from 3D analyses.

The study focuses on deriving de-projected CME speeds based on fits at two distinct time steps. Initial CME longitude and latitude are manually specified for each model, utilizing provided SF locations. Final CME directivity is considered relatively crude, derived from qualitative information extracted from available animations¹⁴. This approach ensures a rigorous basis for evaluating de-projected CME speeds.

2.7.3 Results

Projection Effects

Approximately 10 CMEs were analyzed by two designated observers in our research team, including myself, utilizing all three models in the PyThea framework. The fitting process involved two time steps to derive velocity parameters based on height–time estimations. Both observers conducted the 3D de-projection procedure iteratively for each event, resulting in averaged CME speeds presented in Table 2.5, rounded to the nearest tenth. Discrepancies between fitting instances were treated as errors, ranging from 10 km s^{-1} to twice the estimated speed. Figure 2.13 illustrates the correlation between 3D speeds and estimated errors, showing significant variability, particularly with the GCS model, but a discernible positive trend between error magnitude and CME speed.

Subjectivity and varied experience levels among observers influenced the visual fitting process, leading to differences in evaluated speeds, both within individual observers using the same model and across different models for a single observer. Variations in operating system software also contributed to result discrepancies. Events E04, E08, and E21 were incomplete due to PyThea computing issues or substantial uncertainty in CME structure assessment.

Our findings highlight the inherent subjectivity in procedures relying on personal judgment for fit quality, detailed further in (Verbeke et al. 2022). Averaged CME speeds, meticulously outlined in

¹⁴<http://helioweb.net/archive/>

Table 2.5, will serve as the basis for subsequent correlation studies.

Table 2.5: CME Speeds (km s^{-1}) for Observers 1 and 2. Credit goes to Miteva et al. (2023).

#	Spheroid		Ellipsoid		GCS	
	obs1	obs2	obs1	obs2	obs1	obs2
E01	2170 \pm 870	1800 \pm 270	2130 \pm 200	1710 \pm 450	1590 \pm 100	1760 \pm 10
E02	1780 \pm 140	1350 \pm 50	1880 \pm 580	1310 \pm 90	1780 \pm 260	1630 \pm 130
E03	770 \pm 40	740 \pm 10	640 \pm 180	740 \pm 180	1020 \pm 170	700 \pm 270
E04	-	2150 \pm 140	-	2460 \pm 70	-	2530 \pm 630
E06	1410 \pm 420	710 \pm 70	1870 \pm 50	1700 \pm 300	1680 \pm 870	1560 \pm 470
E08	350 \pm 90	-	360 \pm 150	-	350 \pm 70	-
E09	690 \pm 280	630 \pm 150	550 \pm 170	590 \pm 60	670 \pm 610	710 \pm 220
E10	840 \pm 380	610 \pm 1040	1120 \pm 360	960 \pm 90	1160 \pm 650	1310 \pm 80
E13	320 \pm 90	350 \pm 50	620 \pm 140	750 \pm 160	780 \pm 80	1310 \pm 700
E20	830 \pm 190	800 \pm 600	790 \pm 90	570 \pm 20	1240 \pm 280	1130 \pm 230
E21	620 \pm 230	-	440 \pm 40	-	280 \pm 180	-
E24	750 \pm 270	1310 \pm 220	880 \pm 350	2020 \pm 960	950 \pm 120	1560 \pm 540

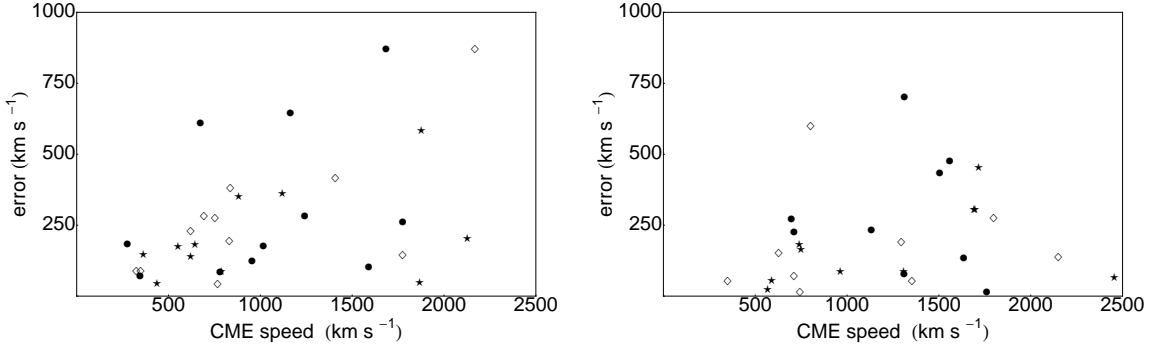


Figure 2.13: Scatter plot illustrates the comparison of 3D de-projected CME speeds derived from the spheroid model (depicted as diamonds), the ellipsoid model (represented by stars), and the GCS model (indicated as dots) versus the measurement errors for observers 1 (left) and 2 (right). Credit goes to Miteva et al. (2023).

Correlation between GSs, Coronal, and Near-Sun Parameters

Figure 2.14 shows a scatter plot illustrating the relationship between the modulus of the GS Dst index and CME speed. Averaged results of three model fits (*3D-mean*) are compared with 2D SOHO-LASCO CME speeds in Table 2.6, alongside error estimates from 3D de-projections. Despite some overlap, the largest error value among observers (as outlined in Table 2.5) is highlighted for clarity.

Analysis reveals no discernible trend between the Dst index and CME speed, regardless of considering 3D de-projections or 2D CME speeds. Data constraints prevented 3D speed de-projections for the most robust GSs, skewing speed distribution and impacting findings. Despite the modest sample size (10 to 20 event pairs), Pearson correlations assess fit quality. Coefficients in Table 2.6 range from negligible (e.g., 0.04 for 2D LASCO speeds) to moderate (highest: 0.55 with GCS model). Notably, no significant correlations are found between Dst index and other coronal parameters (e.g., SF class, location, CME AW), as comprehensively presented in the same table.

Correlation between GSs and IP Parameters

We explore correlations between GSs and various parameters linked to pre-selected IP phenomena. Scatter plots illustrate relationships such as Dst index versus ICME speed and IP shock speed, Dst versus Mach number and sheath duration, and Dst versus $|B_z|$ and B_d/B_u . Figure 2.15 and Table 2.7 detail these correlations. For the limited sample used, we observe moderately positive trends between

Table 2.6: Table displaying Pearson correlation coefficients among the GS Dst index, CME speed, and various solar parameters, with the respective sample sizes indicated in parentheses. Credit goes to Miteva et al. (2023).

CME source	Dst-speed	solar parameter	Dst-solar parameter
LASCO	0.04 (20)	SF class	-0.04 (14)
3D - mean	0.49 (12)	SF latitude	-0.16 (14)
3D spheroid - mean	0.34 (12)	SF longitude	0.13 (14)
3D spheroid - obs1	0.14 (11)	CME AW	0.03 (20)
3D spheroid - obs2	0.15 (10)		
3D ellipsoid - mean	0.53 (12)		
3D ellipsoid - obs1	0.28 (11)		
3D ellipsoid - obs2	0.40 (10)		
3D GCS - mean	0.55 (12)		
3D GCS - obs1	0.49 (11)		
3D GCS - obs2	0.27 (10)		

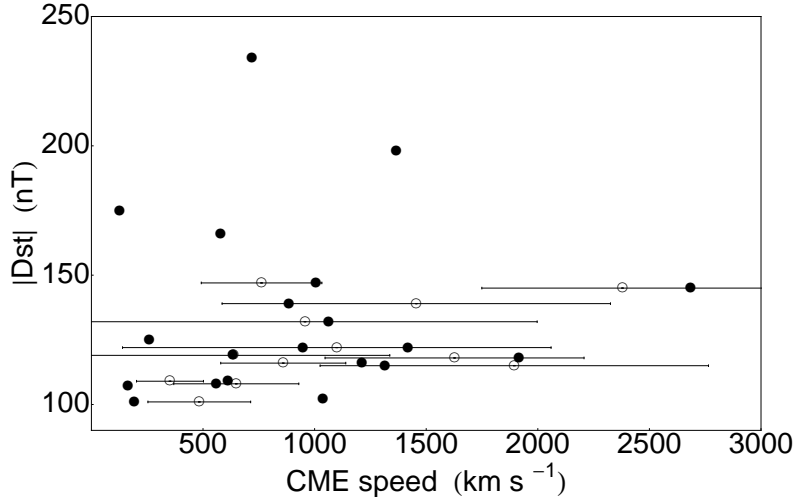


Figure 2.14: Scatter plot illustrating the relationship between the Dst index and CME speed, incorporating data from the SOHO/LASCO instrument (represented by filled circles) and 3D de-projections (depicted by empty circles). Credit goes to Miteva et al. (2023).

Table 2.7: Tabular representation of Pearson correlation coefficients between the GS Dst index and various parameters of IP phenomena. The data is derived from Wind satellite measurements, unless otherwise stated, with the corresponding sample sizes indicated in parentheses. Credit goes to Miteva et al. (2023).

IP parameter	Dst-IP parameter
ICME speed	0.37 (24)
ICME speed (ACE)	0.44 (22)
IP shock speed	0.35 (22)
Mach number	0.36 (21)
sheath duration	0.22 (20)
$ B_z $	0.37 (25)
B_d/B_u	0.48 (21)
T_d/T_u	0.40 (21)
N_d/N_u	0.46 (21)
B	-0.14 (20)
V	0.19 (20)
β_u	-0.14 (21)

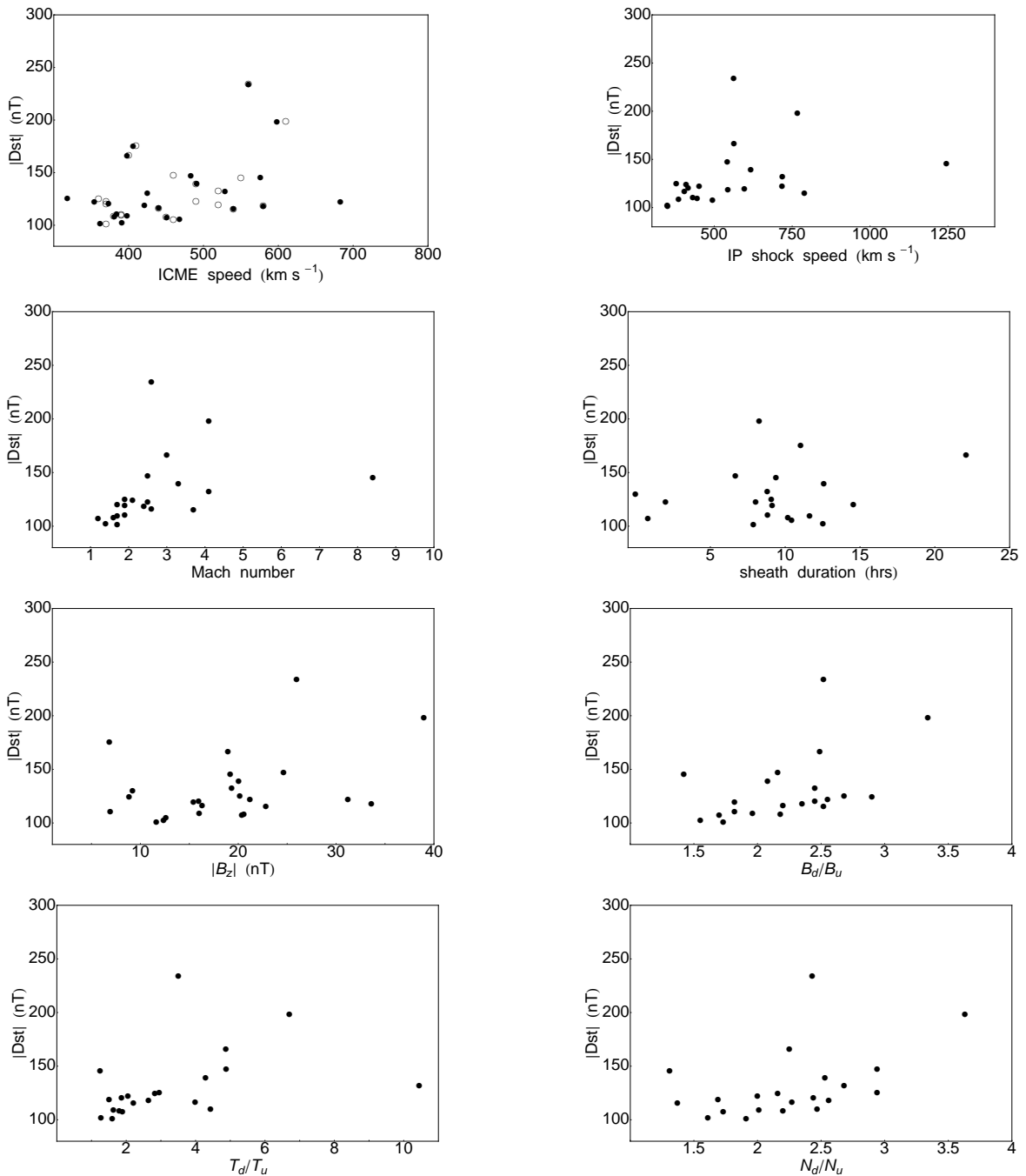


Figure 2.15: Comprehensive scatter plots illustrating the relationships between Dst index and various solar wind parameters, including Wind/ACE ICME speed, IP shock speed, Mach number, duration of sheath region, B_z , magnetic field jump, temperature jump, and density jump. Credit goes to Miteva et al. (2023).

Dst index and plasma compression parameters at the shock interface, comparable to or slightly larger than correlations with ICME speeds. However, the trend with $|B_z|$ is weaker (0.37), contrasting with robust trends from prior studies. Correlations involving Dst and IP shock speed, Mach number, or sheath duration are relatively smaller.

Recent reports suggest strong correlations with electric and magnetic field components (Echer & Gonzalez 2022), although this exceeds our current analysis scope. Caution is warranted in interpreting results due to lack of uncertainty estimates for correlation coefficients. Additional parameters from ICME and IP shock catalogs show no robust correlations with Dst index, all correlation coefficients being smaller than 0.2.

Forecasting GS Strength Based on Solar and IP Parameters

We examine how magnetic obstacle type, orientation upon Earth arrival, and 3D reconstructed CME speeds collectively impact GS intensity, approximated by the Dst index.

The most potent GSs in our compilation exhibit distinctive magnetic structure parameters, including complexity, orientation, and speed at Earth. Exceptions include instances of fast speed flank hits or uncertain configurations, possibly influenced by fast solar wind streams or CIRs. Notably, IP structure associated with certain GSs has notably low speeds. Interpretation considers information from both speed reconstructions and in situ measurements to enhance analysis robustness.

2.8 Discussion

The May 11, 2011 eruption showcased a variety of solar phenomena, including a fast partial-halo CME, a weak solar flare, an eruptive filament, and a type II radio burst. Analyzing the interplay of these events offers insights into solar and interplanetary dynamics.

2.8.1 CME Kinematics and Coronal Shock Wave Characteristics

The CME exhibited characteristics such as a linear speed of 745 km s^{-1} , an acceleration of 3.3 m s^{-2} , and an angular width of 225° . The associated shock wave displayed complex kinematics, observed in both the low and middle/outer corona.

In the low corona, the shock wave's asymmetry and evolving geometry revealed dynamic behavior. Differences in thickness, speed, and acceleration between flanks suggested complex interactions with the coronal environment. Segmenting the shock surface highlighted variations in shock characteristics.

In the middle/outer corona, SOHO/LASCO measurements depicted the dynamic evolution of the EUV wave. Gallagher model fitting emphasized the importance of combining AIA and LASCO measurements. Fluctuations in acceleration and speed underscored the shock wave's complexity.

Statistical analysis revealed patterns in coronal wave events, with radial waves exhibiting distinct characteristics compared to lateral waves. Cumulative dynamic spectra illustrated trends in shock speed and intensity with distance. Correlations between plasma parameters and shock characteristics were identified, laying the groundwork for further parameterizations in subsequent phases of the project.

2.8.2 Dynamic Coronal Features Analysis with Wavetrack

Stepanyuk et al. (2022) utilized Wavetrack to study eruptive solar events, focusing on the May 11, 2011 event associated with a significant CBF. Two additional events, on June 7, 2011, and December 12, 2013, were also examined, demonstrating Wavetrack's versatility in tracking various solar features.

Wavetrack efficiently delineated evolving CBFs across consecutive time steps, even with variations in pixel distributions and intensities. This enabled detailed exploration of time-dependent shapes and intensity distributions, distinct from the broader corona. Segmentation during the December 12, 2013 event highlighted Wavetrack's effectiveness in tracking multiple parts of the same feature.

To analyze CBF and filament kinematics, the FLCT method was employed. Results revealed the plane-of-sky direction and speed of different CBF regions during the May 11, 2011 event. The study showcased the complementary nature of Wavetrack and FLCT in elucidating dynamic behavior.

The study calculated plane-of-sky speeds of the erupting filament driver (Fig. 2.10), showing higher speeds directly below the region of highest speeds in the CBF. Geometric centers and centers of mass were determined, providing insights into the dynamics of the solar eruption event. These findings offer

insights into the dynamics and characteristics of the May 11, 2011 solar eruption event, particularly regarding the movement and speeds of key features like the CBF and erupting filament driver.

2.8.3 Subjectivity in CME Speed Determination

Our study on CMEs reveals significant variability due to subjectivity in fitting and de-projection procedures. Analysis of approximately 10 CMEs using PyThea framework models highlights observer disparities and technical limitations. Averaged CME speeds, documented in Table 2.5, show associated errors emphasizing the challenges and uncertainties in this process.

Despite subjectivity challenges, these averaged values form the basis for correlation studies. Correlating GSs with parameters like the Dst index and CME speeds reveals no discernible trend, with Pearson correlation coefficients indicating diverse relationships.

Scatter plots in Figure 2.15 and Table 2.7 show moderately positive correlations between the Dst index and plasma compression parameters at the shock interface. However, caution is warranted due to the absence of uncertainty estimates for correlation coefficients.

Further analysis of magnetic obstacle characteristics and 3D CME speeds sheds light on patterns influencing GS intensity. Nose-like orientation and complex or flux-rope structures characterize the most potent GSs. Limitations in single-point IP shock speed measurements underscore the need for comprehensive interpretation considering both speed reconstructions and in situ measurements.

2.9 Conclusions

I conducted a study characterizing 26 historical CME-driven CBFs in the low solar corona, observed with the AIA instrument onboard the SDO spacecraft. Utilizing the SPREAdFAST framework, we integrated physics-based and data-driven models to estimate coronal magnetic fields, shock wave dynamics, energetic particle acceleration, and SEP propagation. The analysis relied on AIA base-difference images to generate annulus plots and J-maps for kinematic measurements in radial and lateral directions.

Various time-dependent and distance-dependent kinematic parameters were computed, including shock speed, acceleration, intensity, and thickness. LASCO measurements up to $17R_{\odot}$ were incorporated to improve SEP spectra characterization. Kinematic measurements facilitated time-dependent 3D geometric models of wavefronts and informed plasma diagnostics through MHD and DEM models.

Shock kinematic measurements were used to fit geometric spheroid surface models for each time step, capturing shock characteristics accurately. Parametrized relationships between plasma parameters were explored to identify connections and interdependencies.

In Stepanyuk et al. (2022), we present Wavetrack, an innovative method for automated identification and monitoring of dynamic coronal phenomena. By employing wavelet decomposition, feature enhancement, and filtering, Wavetrack generates time-dependent masks for feature pixels, particularly adept at tracing faint, large-scale features like coronal bright fronts (CBFs) and EUV waves. Operable for on-disk and off-limb features, Wavetrack is implemented as a versatile Python framework.

Application to four events, focusing on CBFs in May 11 and June 07, 2011, and December 12, 2013, demonstrates Wavetrack's proficiency in tracking complete CBF pixel maps. Integrating with the FLCT method reveals the dynamic evolution of CBF regions and their correlation with eruptive filament drivers, highlighting compression effects and speed variations.

Wavetrack also tracks temporal changes in feature regions by computing time-dependent vectors between pixel geometric centers and centers of mass, providing valuable metrics for feature evolution. However, manual segmentation and parameter fine-tuning are currently required, with plans for future improvements to enhance versatility.

The methodology shows promise for broader application across solar dynamic features and datasets, with future research extending its use to filament evolution and coronagraph data analysis, refining our understanding of eruptive front variations across different observational contexts.

Our findings in Kozarev et al. (2022) and Stepanyuk et al. (2022) contribute to understanding shock kinematics and plasma parameters. Future investigations will focus on SEP acceleration near the Sun and transport of coronal and interplanetary particles, refining shock and coronal parameter characterization methods for enhanced accuracy and reliability.

In Miteva et al. (2023), we analyze geo-effective storms during solar cycle 24 to identify predictors for storm intensity. Our approach integrates solar, near-Sun, and interplanetary parameters, incorporating results from PyThea, a tool for CME speed de-projection. We find improvements in correlation

coefficients for projected CME speed, although fast CMEs pose challenges due to reconstruction errors and structural complexity.

Fast halo CMEs exhibit significant deviations, affecting reconstruction quality and limiting forecasting potential for storm strength. In contrast, certain interplanetary parameters, particularly ICME and IP shock speeds, show moderate positive correlations with storm intensity. However, discrepancies in measurements and single-point observations raise concerns about predictive capability.

Among various parameters, the combination of speed and orientation of the magnetic obstacle appears influential, as seen qualitatively in the *helioweather* animations. While de-projected CME speeds enhance modeling accuracy, they do not directly impact storm intensity. Permanent stereoscopic observations, like the ESA Vigil mission, are crucial for improved 3D reconstructions of CME geometries and accurate speed estimations.

In conclusion, our study lays the groundwork for ongoing projects aimed at refining parameterizations and integrating synoptic MHD parameters into the *S3M* synoptic model, enhancing our understanding of solar dynamics and space weather forecasting.

Our findings highlight the importance of integrating advanced tracking methodologies like Wavetrack with kinematic analyses such as FLCT, providing deeper insights into the complexities of eruptive solar events. As we refine these methodologies, our understanding of solar phenomena will advance, contributing to Heliophysics. Furthermore, our study emphasizes the complexity of studying CMEs and their impact on geomagnetic storms. Integrating observational data and model outputs offers a comprehensive perspective for further investigations into the dynamic interplay between solar and interplanetary phenomena in shaping space weather events.

Chapter 3

Solar Radio Observations Integrating Data for Coronal Diagnostics

In this chapter, I focus on multi-wavelength observations of solar type III radio bursts and modeling studies of plasma parameters and coronal magnetic fields to understand solar radio emission mechanisms during quiet times and coronal conditions influencing burst propagation. Initially, I introduce type III radio bursts and detail the data used, followed by output presentation and interpretation.

3.1 Introduction

Type III radio bursts result from energetic electron beams injected into the solar corona, propagating along IMF lines Ergun et al. (1998); Pick (2006); Reid (2020). These beams trigger plasma waves, transformed into radio emission at local plasma frequency or its harmonics Melrose (2017). They manifest as intense emissions drifting in frequency over seconds to minutes, detectable across a wide frequency range Wild & McCready (1950); Lecacheux et al. (1989); Bonnin et al. (2008), offering insight into solar active phenomena Reid & Ratcliffe (2014); Kontar et al. (2017).

Electron beams persist well beyond 1 AU, providing in situ insights into burst and ambient heliospheric conditions, including electron density, beam speed, and Langmuir wave detection Dulk et al. (1985); Boudjada et al. (2020); Gurnett & Anderson (1976, 1977); Reid & Ratcliffe (2014). Combining ground-based and space-borne observations is crucial for comprehensive analysis.

This work studies type III bursts on April 3, 2019, using data from LOFAR van Haarlem et al. (2013) and PSP Fox et al. (2016), integrating PFSS and MAS models Altschuler & Newkirk (1969); Schatten et al. (1969); Mikić et al. (1999). LOFAR imaging provides burst source localization, expanding knowledge of electron beam triggers and coronal conditions. Understanding these aspects is crucial for comprehending solar energetic particles, solar wind, and their effects on near-Earth space.

Previous studies have investigated type III burst mechanisms Chen et al. (2013); Bonnin et al. (2008); Reiner et al. (2009); Saint-Hilaire et al. (2012); Morosan & Gallagher (2017); Pulupa et al. (2020); Krupar et al. (2020); Cattell et al. (2021); Harra et al. (2021); Badman et al. (2022). Modern instruments like LOFAR and PSP offer enhanced sensitivity, yet challenges remain, including electron acceleration mechanisms and discrepancies between observations and models.

The chapter is structured as follows: Section 3.2 describes LOFAR and PSP observations of type III bursts; Section 3.3 explains data analysis and modeling techniques; Section 3.4 presents analysis results, investigating physical mechanisms and comparing with solar corona models; and Section 3.5 summarizes findings and discusses implications.

3.2 Observations

Several studies have investigated solar radio emissions during the PSP's second encounter in late 2019 Krupar et al. (2020); Pulupa et al. (2020); Cattell et al. (2021); Harra et al. (2021); Badman et al. (2022). This study focuses on type III radio bursts occurring on April 3, 2019, between approximately 12:10 and 12:50 UT, coinciding with active regions AR12737 and AR12738. AR12737, on the near side of the Sun, exhibited a β magnetic configuration with eight sunspots Hale et al. (1919), while detailed observations of AR12738 were unattainable due to its far-side position.

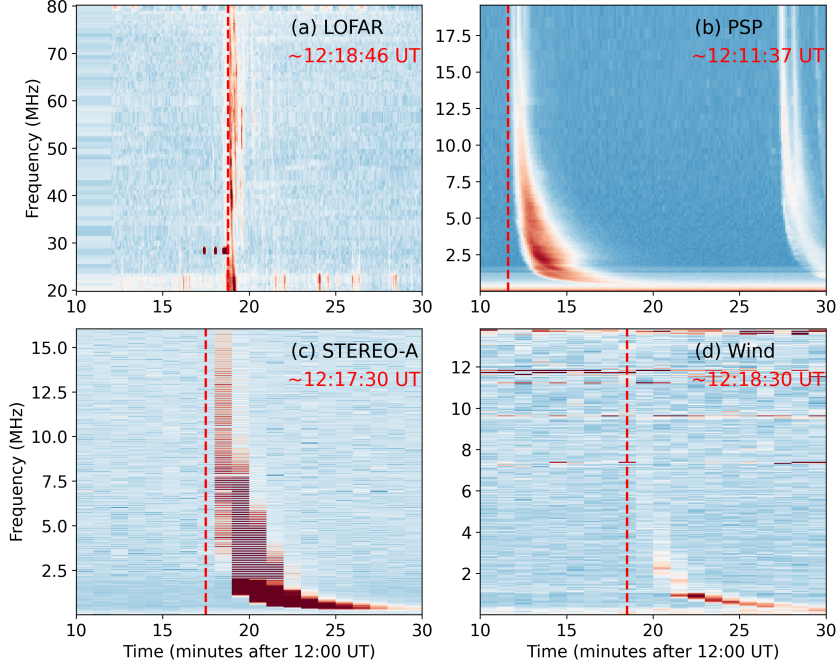


Figure 3.1: Radio dynamic spectra for a single burst obtained from multiple instruments. The top-left panel is from the LOFAR/LBA instrument, the top-right is from the PSP/FIELDS instrument, the bottom-left is from the STEREO/SWAVES instrument, and the bottom-right is from the Wind/WAVES. The vertical red dashed line denotes the start time of the burst.

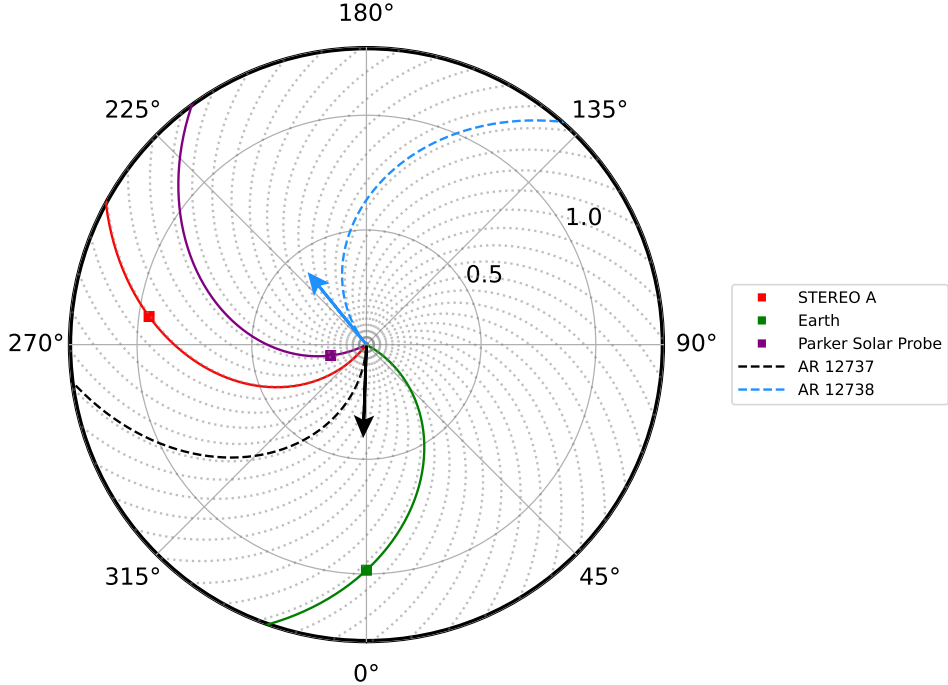


Figure 3.2: Top view of the spacecraft positions in the ecliptic plane at 12:15 UT on April 3, 2019, with the Sun-Earth line as the reference point for longitude. The Earth's location is representative of the positions of LOFAR, Wind/WAVES, and GOES-15/XRS instruments. The spacecraft were connected back to the Sun by a 400 km/s reference Parker Spiral. The black arrow represents the longitude of AR12737 and the blue arrow represents the longitude of the AR12738. The gray dotted lines are the background Parker spiral field lines. The black dashed spiral shows the field line connected to the AR12737, and the blue dashed spiral is connected to the AR12738. The figure is generated using the Solar MAgnetic Connection Haus (Solar-MACH) tool (Gieseler et al. 2023).

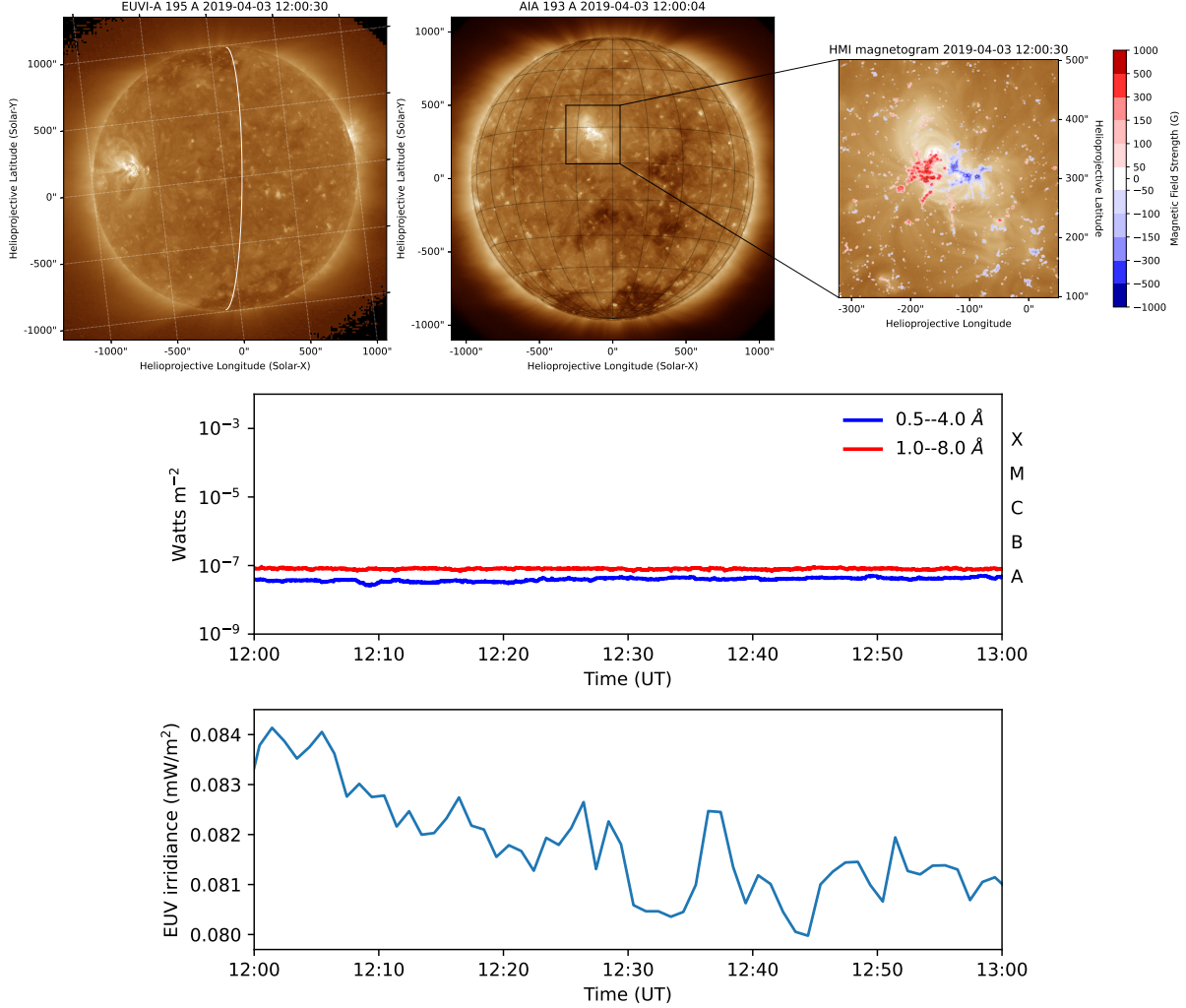


Figure 3.3: Exploring the X-ray and EUV emissions from the Sun. The top panel showcases a cutout region of the SDO/AIA 193 Å image of the solar disk along with the STEREO-A EUVI 195 Å point of view. The white curve is the limb of the solar disk as seen by AIA from the right side. The red and blue colors are the contours of the line-of-sight magnetogram from the SDO/HMI instrument. The levels are (50, 100, 150, 300, 500, 1000) Gauss. The middle panel shows the X-ray flux from the GOES-14 spacecraft shows minimum activity. The bottom panel shows the time series of the ESP Quad band from the SDO/EVE instrument, which shows the solar irradiance in the EUV band.

Intense type III radio bursts were observed by four instruments (Wind/WAVES, PSP/FIELDS, STEREO-A/SWAVES, and LOFAR/LBA) during a regular survey. Figure 3.1 displays the first type III burst observed by these instruments, with the start time determined using the second derivative of the light curve at specific frequency channels. The relative orientations of the instruments with respect to Earth are shown in Figure 3.2, with PSP and STEREO spacecraft almost aligned with the Sun. The solar disk appeared quiet, with no X-ray or EUV transient emissions during the study period, confirmed by GOES-15/XRS and SDO/EVE observations. Despite this, the sensitive LOFAR telescope detected bursts close to noon, corroborated by PSP data.

Localized regions of relatively higher intensity, likely small-scale coronal brightening spots or campfires, were observed in EUVI and AIA images Young et al. (2018); Madjarska (2019); Berghmans et al. (2021). Subsequent subsections introduce the PSP and LOFAR instruments and their observations of the radio bursts.

3.2.1 PSP Observations

Parker Solar Probe (PSP) is a spacecraft launched in 2018 to study solar corona and solar wind (Fox et al. 2016). I utilized level-2 data from the FIELDS instrument suite (Bale et al. 2016; Pulupa et al. 2017), available in CDF format on the PSP FIELDS data products website¹. Data values were converted from V^2/Hz to dB units using a threshold of $10^{-16} V^2/Hz$ for radio burst detection (Pulupa et al. 2020). High- and Low-Frequency Receiver data were combined into a single dynamic spectrum covering 10.5 kHz to 19.2 MHz, with noise minimized through subtraction of mean intensity values.

3.2.2 LOFAR Observations

The LOw Frequency ARray (LOFAR) telescope (van Haarlem et al. 2013) observes the Sun at frequencies between 10 and 240 MHz. Dynamic spectrum data from the Low-Band Antenna (LBA) were obtained from the LOFAR long-term archive². Background subtraction and Gaussian smoothing were applied to clean the spectrum. PSP and LOFAR spectra were combined, considering the travel time difference of radio signals from the Sun to each instrument. LOFAR data were down-sampled to match PSP’s 7-second cadence. The resulting combined spectrum is shown in Figure 3.4. LOFAR’s LBA frequency ranges between 19.82 and 80.16 MHz, while PSP’s cover 10.55 kHz to 19.17 MHz.

To automatically detect type III radio bursts in the combined dynamic spectrum, I applied the algorithm proposed by Zhang et al. (2018), which employs probabilistic Hough transformation to detect vertical bright edges within a specified deviation angle from the vertical direction.

3.3 Methods

3.3.1 Imaging of Radio Sources

I developed an automated pipeline to preprocess and calibrate LOFAR interferometric data for solar radio imaging (Zhang et al. 2022a). Burst detection was performed using the algorithm by Zhang et al. (2018) on combined LOFAR and PSP dynamic spectra (Fig. 3.4). The Parker electron-density model (Parker 1960) was employed to map bursts to radial distances, with least-squares fitting used to derive frequency drifts and electron beam speeds.

Subsequently, burst detection was repeated on LOFAR dynamic spectra alone (Fig. 3.5) to identify (f, t) pairs for each burst. Snapshot frequencies were selected for interferometric imaging, calibrated using Tau-A observations. The WSClean algorithm (Offringa et al. 2014) was applied to obtain cleaned images of radio sources at the chosen frequencies.

Persistence imaging was employed to enhance image clarity and information content (Thompson & Young 2016). This method compares pixel values across a time-ordered series of images, retaining the brightest values to create a persistent display.

To determine type III source locations in 3D space, LOFAR observations were combined with modeling. Grids of footpoints were constructed on GONG magnetogram data around active regions AR12737 and AR12738. Pfsspy package (Stansby et al. 2020) traced coronal magnetic field lines, aiding in estimating source radii and 3D positions. Radial distances of sources from the Sun were determined assuming harmonic emission, considering Newkirk electron-density models (Newkirk 1961, 1967). Deprojection of

¹PSP FIELDS data products: <http://research.ssl.berkeley.edu/data/psp/data/sci/fields/>

²LOFAR LTA: <https://lta.lofar.eu/>

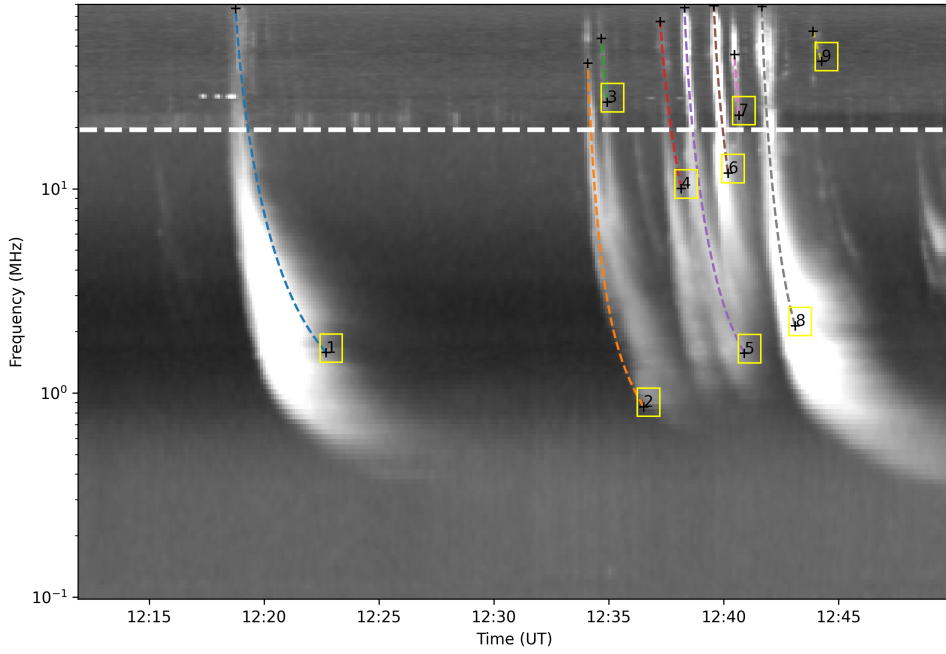


Figure 3.4: Automatic detection of type III radio bursts from the combined radio dynamic spectrum of LOFAR and PSP instruments. The dashed horizontal lines separates the LOFAR frequency range (top) and the PSP frequency range (bottom).

Table 3.1: Characteristics of the type III bursts detected via the automatic algorithm from the combined spectrum.

Burst ID	Start Time (UT)	End Time (UT)	Start Frequency (MHz)	End Frequency (MHz)	Frequency Drift (MHz s^{-1})	Beam Speed (c)
1	12:18:45	12:22:42	76.44	1.57	0.892	0.044
2	12:34:05	12:36:31	41.24	0.86	0.241	0.119
3	12:34:40	12:34:56	54.44	26.54	3.992	0.046
4	12:37:14	12:38:09	66.03	10.02	4.006	0.046
5	12:38:17	12:40:54	76.92	1.57	0.77	0.066
6	12:39:34	12:40:11	78.86	11.93	3.192	0.062
7	12:40:28	12:40:40	45.34	22.9	3.21	0.067
8	12:41:39	12:43:06	78.21	2.13	1.555	0.093
9	12:43:53	12:44:15	59.07	42.13	2.424	0.013

type III sources was performed to estimate their 3D positions relative to Earth's line of sight (LOS) (Fig. 3.7). Axes translations between LOFAR images and 3D space were accounted for. Detailed explanations and equations are provided in Appendices ?? and ??.

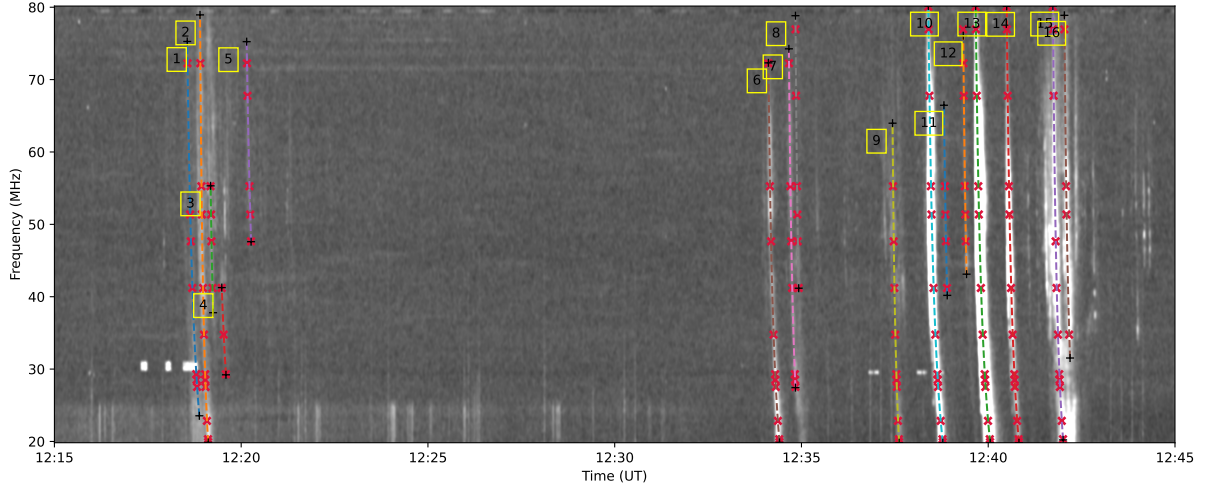


Figure 3.5: Automatic detection of type III bursts observed by LOFAR. The red symbols along the fit lines are the (f, t) coordinates of the image snapshots shown in Figure 3.6.

3.3.2 Modeling

To analyze the coronal plasma environment during the events, I utilized standard coronal solutions from MHD simulations by Predictive Science Inc. (PSI) based on the MAS code (Mikić et al. 1999). The PSI MAS coronal solution for April 3, 2019, at 12:00 UT was obtained from the PSI data archive. Initially, I determined the angle between the burst's radial vector and the line of sight (LOS), as well as the complement angle representing the separation between the radial vector and the Earth's perspective. Using the complement angle, I derived the Carrington longitude to extract a longitudinal segment from the MAS datacube, treating it as if it were in the plane of the sky (POS). Longitudinal slices were extracted using the psipy python package. The FORWARD model, responsible for generating synthetic coronal maps, was then applied to the selected data slice. In Figure 3.8, the first radio contour of the sixth type III burst is overlaid on 2D maps of plasma parameters. These parameters include plasma density, temperature, magnetic field strength, plasma beta parameter, total plasma pressure, and Alfvén speed. Estimates of local plasma conditions at the centroids' coordinates of type III sources for each frequency band are illustrated in Figure 3.9 for the sixth type III burst.

3.4 Results and discussion

3.4.1 Type III Radio Burst Detection and Characterization

Radio waves arrived at STEREO one minute before reaching Wind (Fig. 3.1). However, due to the close proximity to the Sun, the difference in arrival times is within the resolution of the observations, making it inconclusive which spacecraft detected the emission first.

The combined dynamic spectrum from LOFAR and PSP (Fig. 3.4) showed limitations in detecting type III bursts compared to LOFAR alone, possibly due to frequency drift and dispersion challenges. Nine bursts were captured from the combined spectrum, while 16 were traced in LOFAR alone (Table 3.1).

3.4.2 Imaging of Radio Emission Sources

Persistence imaging of the 16 type III bursts from LOFAR (Fig. 3.6) suggested a common origin in the south-east quadrant of the solar disk, despite the absence of an active region at that precise location. A 3D projection of radio source contours onto the coronal magnetic field (Fig. 3.7) revealed a south-eastward propagation relative to Earth's perspective. The radio sources aligned with closed field lines in

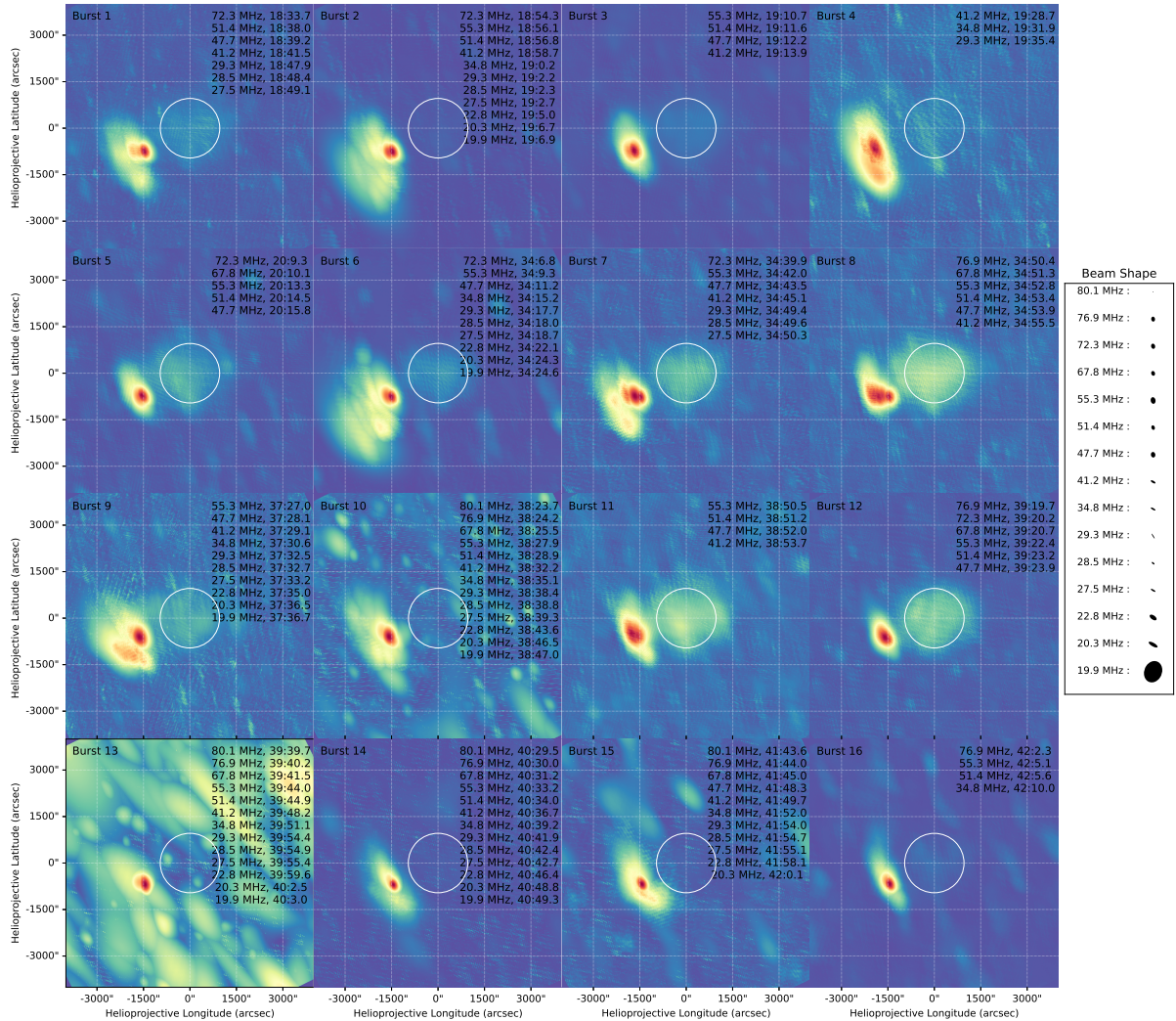


Figure 3.6: Persistence imaging for the 16 type III bursts detected in the LOFAR dynamic spectrum. The label shows the observation frequencies in MHz and times in (minutes:seconds from 12:00:00 UT). Here, the color coding is not absolute, but rather each panel has its own color code.

the southern hemisphere and open field lines from the southern coronal hole. However, limitations exist due to outdated magnetic data for AR12738.

The potential origins of type III radio emissions include closed-field lines structures, electron beams from open-field active regions, or from corona acceleration due to magnetic field expansion in active regions. Furthermore, an inverse relationship between imaging quality and solar radio emission brightness was noted, attributed to calibration solution inaccuracies caused by solar emission leakage into calibrator beam side lobes.

3.4.3 Plasma Diagnostics and Magnetic Field Analysis

The alignment of radio sources (Fig. 3.7) with a streamer-like structure near the equator indicates elevated plasma beta, reduced coronal temperature, and diminished Alfvén speed. However, the coronal plasma density appeared homogeneous with no prominent structures due to model resolution limitations. Radio sources for all bursts were found in the same quadrant from Earth's perspective, confined between the equatorial sheet and the southern coronal hole and moving along that boundary.

Variability of coronal plasma quantities at radio sources' centroids was observed (Fig. 3.9), with coronal temperature increasing with radial distance. Additionally, the behavior of coronal magnetic field, plasma total dynamic pressure, and Alfvén speed decreased over distance. Plasma beta parameter sharply increased around 40 MHz, suggesting dominance of plasma pressure over magnetic pressure at that distance from the Sun.

Comparison of density profiles (Fig. 3.9) indicated significant differences between MAS and FORWARD modeling results compared to the $2.5 \times$ Newkirk density model and theoretical expectations. The discrepancy, even after accounting for enhancement factors, suggests possible scattering effects or stealth CMEs affecting density observations, highlighting limitations in current modeling and suggesting the need for additional physics to characterize density distribution accurately.

3.5 Summary and conclusions

In this study (Nedal et al. 2023b), a series of 16 type III bursts observed on April 3, 2019, during the PSP's near-Sun encounter, were analyzed using PSP/FIELDS and LOFAR. These bursts, spanning nearly 20 minutes, occurred amidst relative solar quietness with a dominant active region on the solar disk. A semi-automated pipeline aligned PSP and LOFAR observations, facilitating analysis of burst characteristics like frequency drift and electron beam speeds, suggesting their interrelation.

Interferometric imaging revealed a single source for these bursts in the solar corona's southeast limb. Various potential origins for the bursts were discussed, including impulsive events (Ishikawa et al. 2017; Che 2018; Chhabra et al. 2021), plasma upflows (Harra et al. 2021), and magnetic reconnection (Gopalswamy et al. 2022a). Magnetic extrapolation indicated no open potential field lines to active regions AR12737 or AR12738, consistent with prior findings.

Integration of burst source location with magnetic modeling suggested discrepancies, possibly due to scattering effects. Scattering and propagation effects were found significant, impacting burst location determination. Future investigations, including the TDoA technique and Solar Orbiter observations, were proposed.

The study highlighted LOFAR's efficacy in characterizing solar eruptive events and quiet periods, with implications for space weather monitoring. Future work aims to automate burst analysis and investigate their relation to solar surface activity. Additionally, analysis using LOFAR imaging and MAS modeling indicated discrepancies between observed and modeled burst trajectories, emphasizing the need for model refinements. Overall, this study underscores the importance of considering scattering effects and refining models to enhance understanding of solar radio emissions' propagation in the corona (Kontar et al. 2019, 2023; Chen et al. 2023).

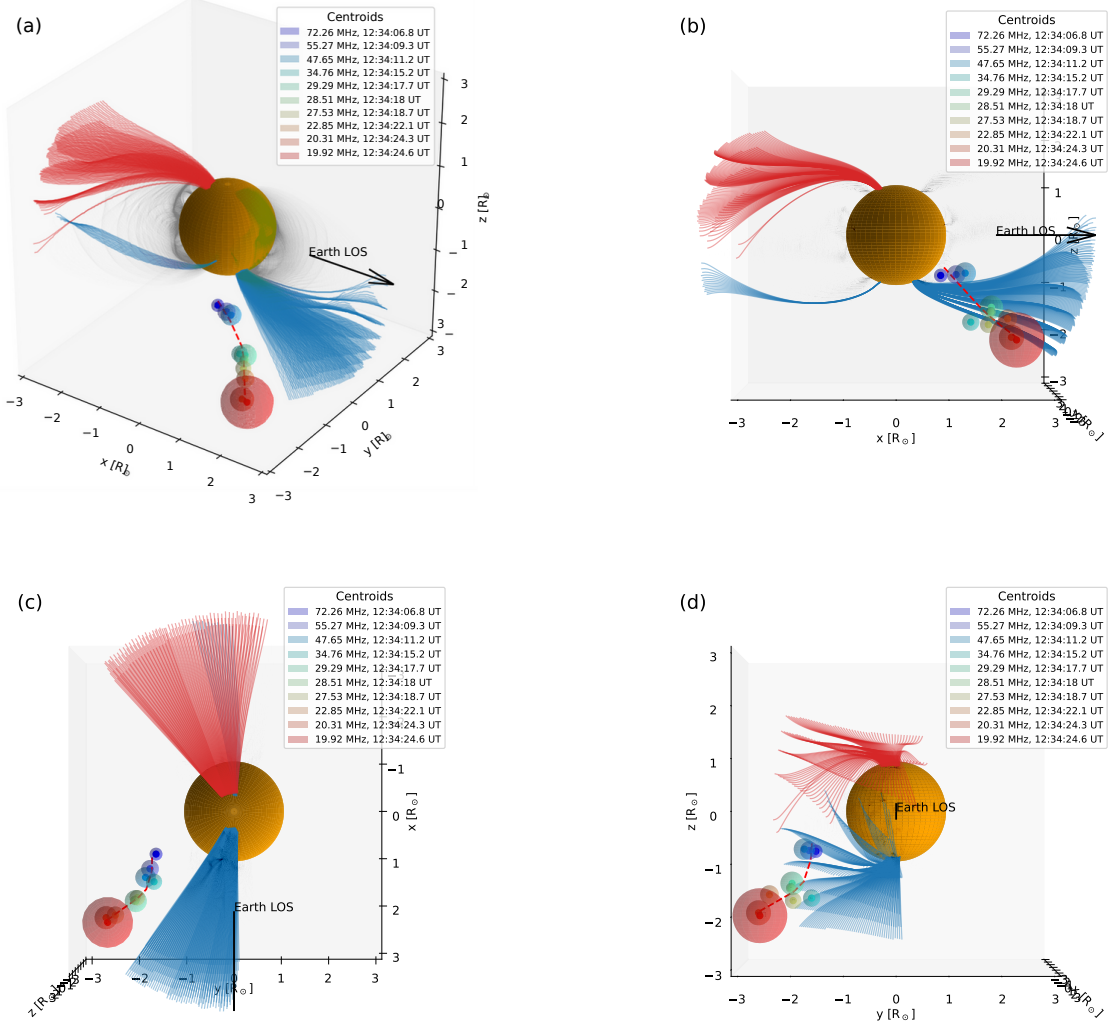


Figure 3.7: Different viewing angles for the deprojection of the radio sources of the sixth burst using the $2.5 \times$ Newkirk electron-density model on the PFSS solution. The black arrow points toward the Earth's LOS. The yz plane is the POS as seen from the Earth. The red dashed line is a spline curve fit for the sources' centroids. The red, black, and blue curves are the open northern, closed, and open southern field lines, respectively. The opacity of the closed field lines is decreased for better visualization.

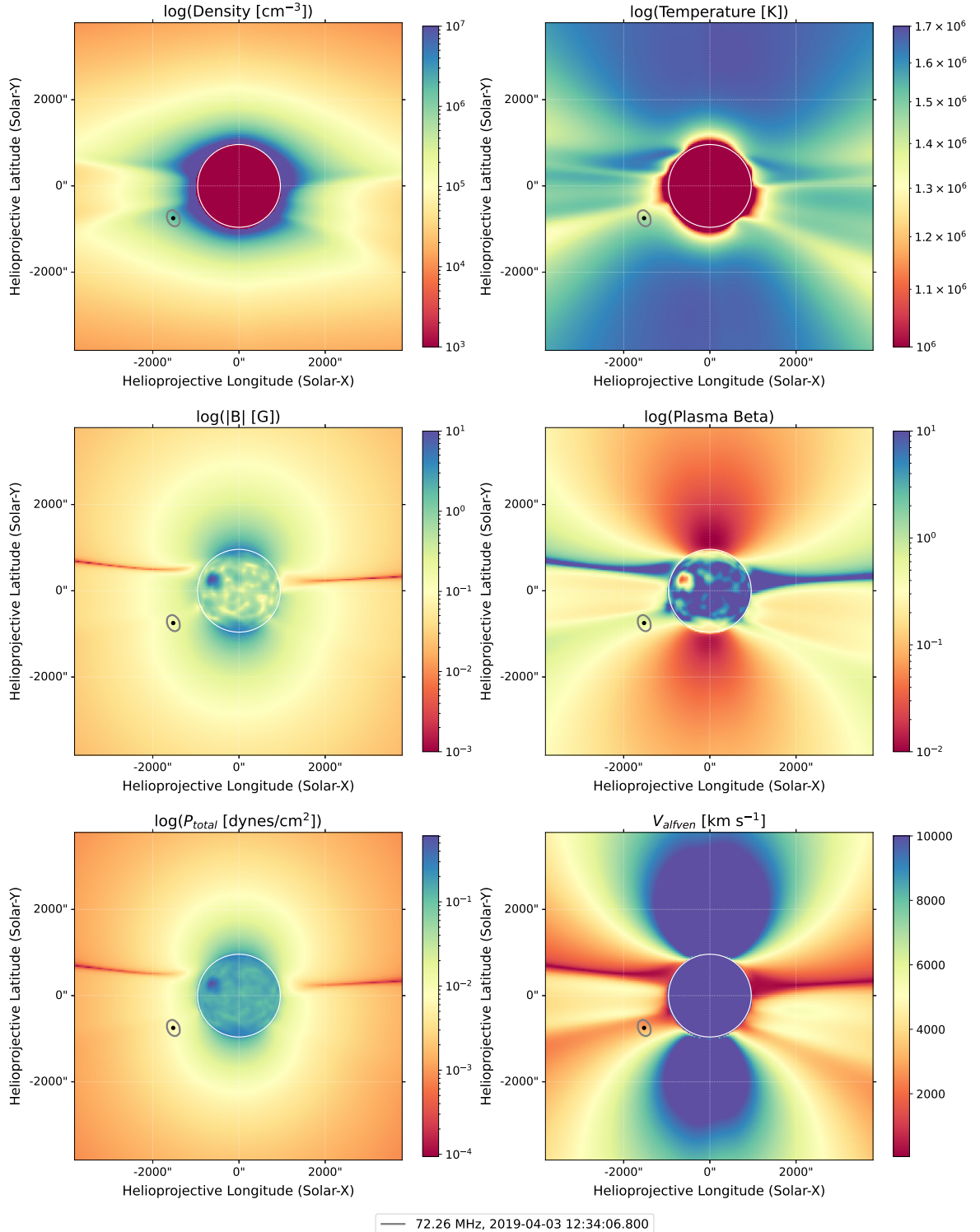


Figure 3.8: Synthesized maps of plasma parameters obtained using the FORWARD toolset, with the 70%-contour of radio emission of the sixth burst at the first timestamp (12:34:06.8 UT) at the frequency of 72.26 MHz depicted on top of the 2D POS cuts. The left column represents, from top to bottom, plasma density, magnetic field, and the total plasma dynamic pressure. The right column represents, from top to bottom, the temperature, plasma beta, and the Alfvén speed.

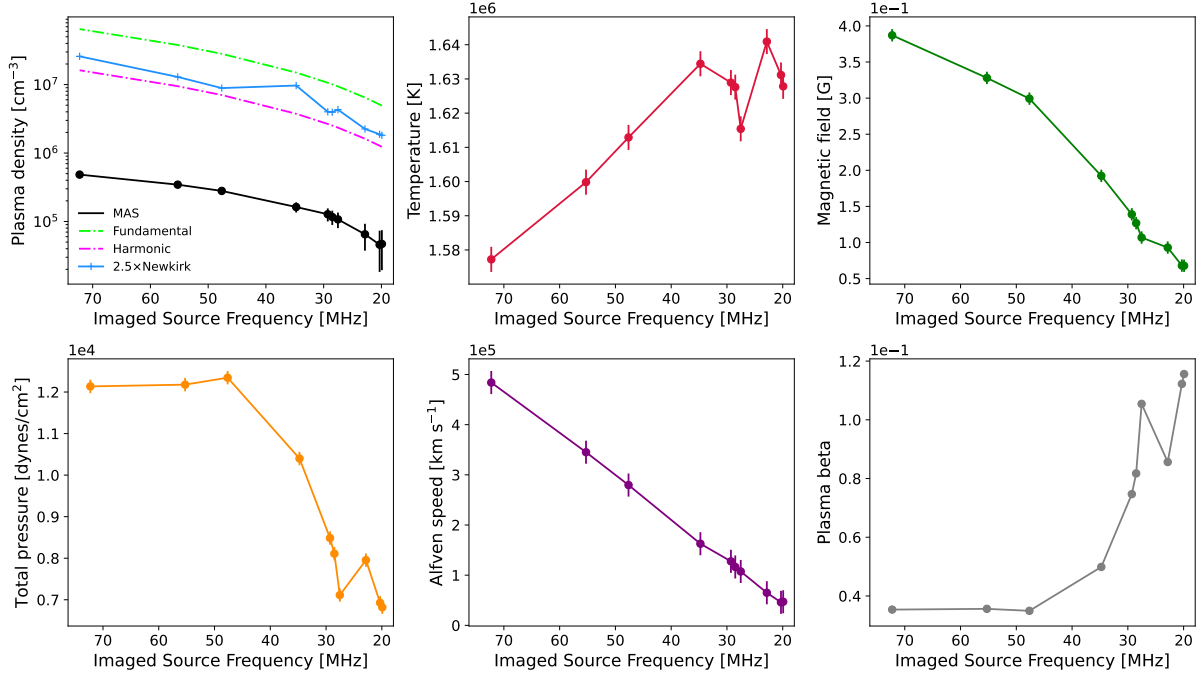


Figure 3.9: Coronal plasma parameters sampled from the 2D maps by the source centroids. The top panel shows (from left to right) the plasma density profiles from the MAS model, $2.5 \times$ Newkirk model, and the theoretical densities under the fundamental and harmonic assumptions, plasma temperature, and magnetic field. The bottom panel shows, from left to right, the total plasma dynamic pressure, Alfvén speed, and plasma beta. The x-axis is inverted to demonstrate a progression of increasing radial distance from the Sun as the observer moves towards the right.

Chapter 4

Modeling and Forecasting of Solar Energetic Protons

This chapter comprises two sections. The first focuses on a modeling study concerning energetic proton acceleration and propagation from the solar corona to 1 AU. Utilizing a physics-based approach, including 3D coronal models and a 3D MAS-MHD model, we employ the EPREM model to determine fluxes and spectra of energetic protons at 1 AU, comparing results with in-situ measurements. The second part introduces a deep learning approach for forecasting the integral flux of energetic protons across three energy channels over three forecasting horizons.

4.1 Introduction

CMEs are pivotal in solar physics, attracting attention for their role in solar activity. Observations across various wavelengths provide insights into their dynamics (Vourlidas et al. 2003; Zhang & Dere 2006; Bein et al. 2011; Bastian et al. 2001; Veronig et al. 2010). Particularly, EUV observations, aided by instruments like AIA, have become crucial in capturing early CME stages (Lemen et al. 2012; Pesnell et al. 2012). CMEs can induce shock waves in the solar corona, observable as EUV waves or CBFs, crucial for SEP acceleration (Thompson et al. 1998; Long et al. 2011; Ontiveros & Vourlidas 2009; Gopalswamy & Yashiro 2011; Battarbee et al. 2013; Kozarev et al. 2013; Schwadron et al. 2014; Kong et al. 2017).

Previous research has focused on characterizing CME dynamics and their associated shocks, notably their relationship with CBFs (Kozarev et al. 2019). Extending this work, our study models CBF-related shock dynamics and particle acceleration up to $10 R_{\odot}$, integrating with a numerical particle transport model, marking a significant advancement in Sun-to-Earth physics-based modeling (Kozarev et al. 2022).

SEP production by coronal shocks throughout the inner heliosphere has garnered attention. CMEs, particularly in their early stages, play a major role in SEP acceleration (Reames 1999; Ontiveros & Vourlidas 2009; Gopalswamy & Yashiro 2011; Battarbee et al. 2013; Kozarev et al. 2013; Schwadron et al. 2014; Kong et al. 2017). Our study extends modeling of CBF-related shock dynamics and particle acceleration, marking the first validated Sun-to-Earth physics-based modeling for SEP acceleration and transport (Kozarev et al. 2022).

Various models exist for SEP forecasting (Whitman et al. 2023), including physics-based, empirical, and Machine Learning (ML) based models. Notably, the PROSPER model provides probabilistic predictions for multiple energy channels (Papaioannou et al. 2022), while ML approaches offer promising avenues for accurate and rapid forecasting (Lavasa et al. 2021; Kasapis et al. 2022). Despite advancements, forecasting SEP fluxes remains challenging, emphasizing the need for dependable forecasting systems. In upcoming sections, we address challenges in modeling SEP fluxes, particularly focusing on imbalanced datasets and low-resolution data. Our study builds upon previous work on CBF kinematics discussed in Chapter 2 and presents advanced deep learning models for forecasting daily integral flux of SEP, offering insights into space radiation profiles.

4.2 Early-Stage SEP Acceleration by CME-Driven Shocks

4.2.1 Overview

Recent studies highlight CMEs as primary contributors to SEP production (Reames 1999), especially in their early stages (Ontiveros & Vourlidas 2009; Gopalswamy & Yashiro 2011). Advanced modeling techniques have been employed to understand CME-related shock dynamics and SEP acceleration (Kozarev et al. 2019; Kozarev & Schwadron 2016; Kozarev et al. 2022). Our study extends this modeling up to $10 R_{\odot}$, marking a significant advancement in Sun-to-Earth physics-based modeling for SEP acceleration and transport. To analyze particle fluxes at 1 AU, we utilize the SPREAdFAST framework discussed in Chapter 2. SPREAdFAST aims to model and analyze SEP events, combining detailed CBF observations with modeling of coronal plasma and SEP production (Kozarev et al. 2022). Its components include CBF kinematics modeling, coronal shock and particle acceleration modeling, interplanetary particle transport modeling, and comparison with observations from instruments like SOHO and ERNE. This comprehensive framework enhances our understanding and forecasting capabilities for SEP events, contributing to advancements in Sun-to-Earth physics-based modeling.

4.2.2 Coronal SEP Acceleration

Utilizing the coronal Diffusive Shock Acceleration (DSA) model (Kozarev & Schwadron 2016; Kozarev et al. 2019), we calculate proton acceleration dynamics from the low corona to $10 R_{\odot}$, employing remote solar observations and data-driven model output from the CASHeW framework. The model incorporates shock parameters along multiple shock-crossing field lines to compute proton injection momenta and subsequent distribution function spectra or fluxes. Its validity is confirmed through analysis of several SEP events.

4.2.3 Input Data and Spectral Fitting

We utilize suprathermal proton spectra obtained from 1 AU fluxes recorded by the SOHO/ERNE instrument (Torsti et al. 1995) as input data, fitted with power laws in the energy range of 0.056–3.0 MeV. These spectra serve as input for the DSA model, allowing detailed examination of proton acceleration dynamics under CME-driven shocks.

4.2.4 Transport of SEPs and Comparison with ERNE Observations

To model the transport of accelerated SEPs to 1 AU, we employ a modified version of the Energetic Particle Radiation Environment Module (Schwadron et al. 2010, EPREM). This model incorporates essential effects such as pitch-angle scattering, adiabatic focusing and cooling, convection, streaming, and stochastic acceleration. Comparison with ERNE observations is conducted, assessing the agreement between modeled and observed proton fluences and onset times. The methodology involves selecting events meeting specific criteria, characterizing CBF kinematics using the CASHeW framework, and comparing modeled and observed proton fluences through scatter plots and Mean Squared Logarithmic Error (MSLE).

4.2.5 Results and Discussions

Modeling the dynamics of shock waves and particle acceleration in the solar corona yields insights into solar particle radiation. The study underscores the coronal environment's pivotal role in SEP acceleration and transport. It reveals that coronal structures and particle energy significantly influence SEP production during CME-driven shocks. Continuous changes in acceleration occur due to plasma parameter gradients. This understanding aids in spatial distribution and energy dependence assessment of SEPs. Moreover, the SPREAdFAST framework shows promise for SEP event forecasting and space weather prediction. Discrepancies between modeled and observed fluxes, particularly at higher energies, suggest the need for refining the modeling framework to better align with observations.

4.3 Solar Proton Flux Forecasting with Deep Learning Models

4.3.1 Data Preparation

This section outlines the selection of input physical quantities, their sources, and the forecasting outputs. Two categories of input features are considered: remote signatures and in-situ measurements. Remote signatures include the F10.7 index, long-wavelength (X_L), and short-wavelength (X_S) x-ray fluxes, obtained from the GOES database¹. In-situ measurements comprise near-Earth solar wind magnetic field and plasma parameters, sourced from spacecraft stationed at the Lagrange point (L1)². Data covering December 1976 to July 2019 were acquired from the Space Physics Data Facility (SPDF) OMNIWeb database and supplemented with daily sunspot numbers from the SILSO archive³.

Figure 4.1 displays the timeseries data for all features, including SEP integral fluxes, sunspot numbers, F10.7 index, x-ray fluxes, solar wind speed, and IMF magnitude. The dataset was split into training, validation, and test sets for deep learning model development (Ripley 1996). Correlation analysis guided the selection of input parameters, focusing on logarithms of SEP fluxes, x-ray fluxes, F10.7 index, sunspot numbers, solar wind speed, and IMF magnitude. Separate models were trained for each target output feature. To ensure consistency, all timeseries data durations were aligned and resampled to daily averages. Missing values were linearly interpolated. The dataset split followed a 9-2-1 strategy over the 43-year timeframe, allocating 74.29% to training, 16.2% to validation, and 9.51% to testing. This strategy aimed to mitigate bias and streamline training efficiency, without shuffling timeseries data to maintain temporal order (Nedal et al. 2019; Pala & Atici 2019; Benson et al. 2020; Zhang et al. 2022b; Zhu et al. 2022).

4.3.2 Method

This section outlines the data analysis methods employed in this study. It begins with an overview of model selection, followed by a detailed explanation of the Bi-directional Long Short-Term Memory (BiLSTM) neural network architecture.

The Bi-LSTM Model

BiLSTM neural networks, an extension of recurrent neural networks (RNNs), process input sequences in both forward and backward directions (Schuster & Paliwal 1997; Hochreiter & Schmidhuber 1997; Kolen & Kremer 2001). Unlike regular RNNs, which rely solely on past information, BiLSTM networks incorporate future context, enhancing prediction accuracy. Each BiLSTM layer comprises forward and backward LSTM layers, as depicted in Figure 4.2, enabling the model to capture long-term dependencies effectively.

BiLSTM networks offer several advantages over traditional LSTM networks (Graves & Schmidhuber 2005; Ihianle et al. 2020; Alharbi & Csala 2021). They excel in tasks like timeseries forecasting, speech recognition, and language translation by capturing long-term dependencies in both directions (Wöllmer et al. 2013; Graves & Jaitly 2014; Sundermeyer et al. 2014; Huang et al. 2018; Nammou et al. 2022). Additionally, they adapt well to variable-length sequences and handle noisy data. However, BiLSTM networks are computationally intensive, require more parameters, and demand larger training datasets.

The final dataset comprises 7 features, spanning from December 25th, 1976, to July 30th, 2019, totaling 15,558 samples. The model configuration includes 4 BiLSTM layers with 64 neurons each and an output dense layer with 3 neurons representing the forecasting horizon. The total number of trainable parameters is 333,699. Training involved 50 epochs, as further iterations did not yield significant improvements. Callbacks such as *ModelCheckpoint*, *EarlyStopping*, and *ReduceLROnPlateau* were employed to monitor model performance, minimize overfitting, and adjust learning rate, respectively.

Model Selection

To determine the most suitable model, I conducted a comprehensive analysis, starting with baseline models like the naive (persistence) model and moving-average model. Following this, I explored ML-based models, opting for the Adaptive moment estimation (Adam) optimizer for its efficiency (Kingma & Ba 2015).

¹GOES SXR Database: <https://satdat.ngdc.noaa.gov/sem/goes/data/avg/>

²OMNI Database: <https://omniweb.gsfc.nasa.gov>

³Sunspot Number Dataset: <https://www.sidc.be/silso/home>

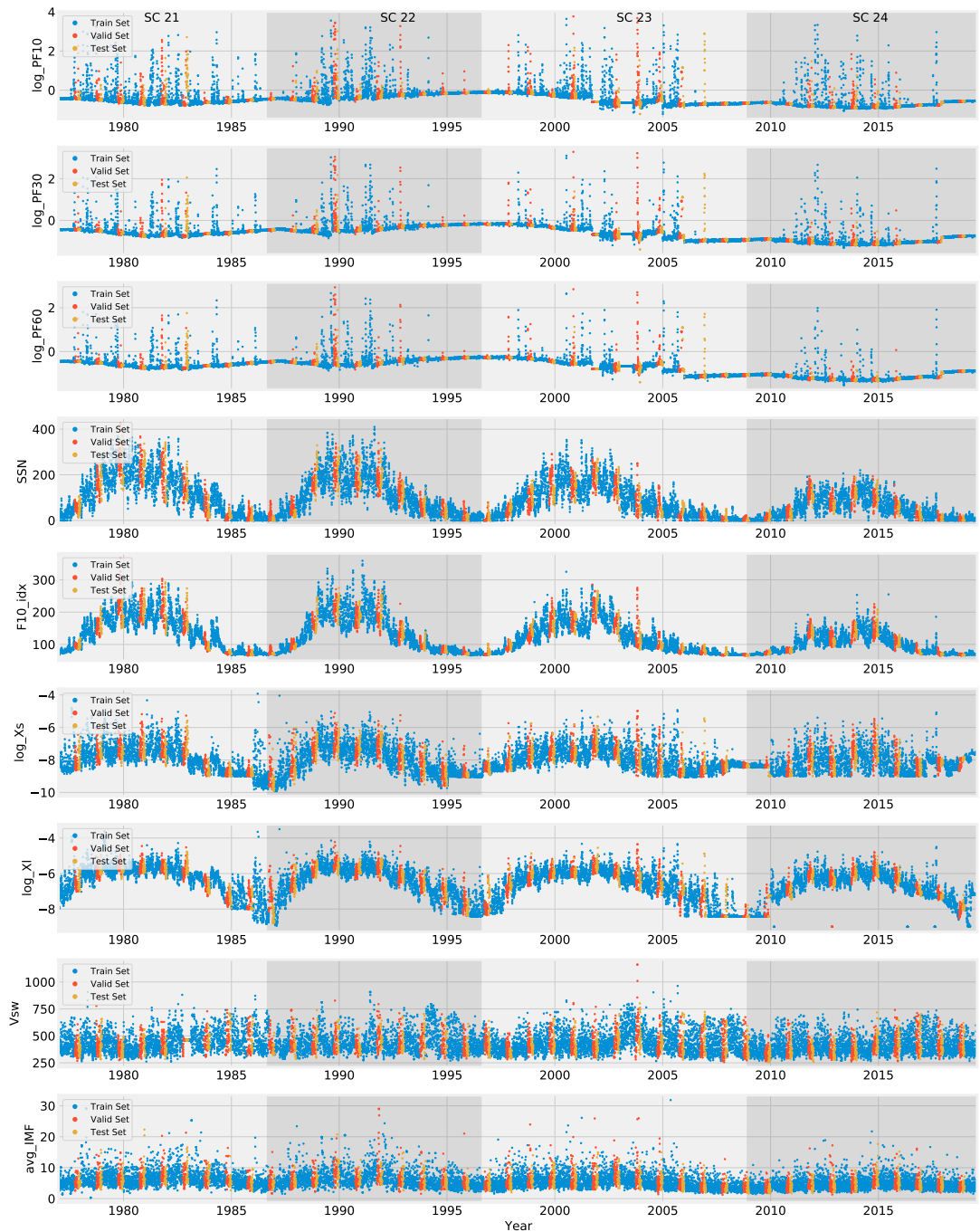


Figure 4.1: Data splitting for all input features, showing the training, validation, and testing sets. Daily data from 1976-12-25 00:00 to 2019-07-30 00:00. The gray shading labels the solar cycles from SC21 to SC24.

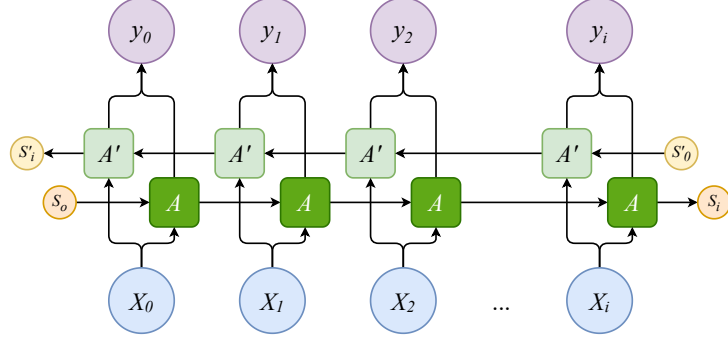


Figure 4.2: Architecture of a single BiLSTM layer. The blue circles at the bottom labeled by $(x_0, x_1, x_2, \dots, x_i)$ are the input data values at multiple time steps. The purple circles, on the other hand, are the output data values at multiple time steps labeled by $(y_0, y_1, y_2, \dots, y_i)$. The dark green and light green boxes are the activation units of the forward and backward layers, respectively. The orange and yellow circles are the hidden states at the forward and backward layers, respectively. Both the forward and backward layers compose a single hidden BiLSTM layer. The figure is adopted from Olah (2015)

Data preparation involved creating a windowed dataset using a Multi-Input Multiple Output (MIMO) strategy, minimizing the imbalance of active and quiet days (Benson et al. 2020). The Huber loss function was selected due to its robustness to outliers, crucial for our noisy data.

Various neural network architectures were examined, including linear models, dense ML models, simple RNNs, LSTM, and BiLSTM models. Optimal learning rates were determined using the `LearningRateScheduler` callback function. Ultimately, a BiLSTM model with five hidden layers, each comprising 64 neurons, and a learning rate of 0.001 was chosen based on performance evaluation on validation and test sets. Figure 4.3 illustrates the comparative analysis of Huber loss across the evaluated models. Multiple evaluation metrics were utilized to assess model accuracy and performance, guiding further refinement.

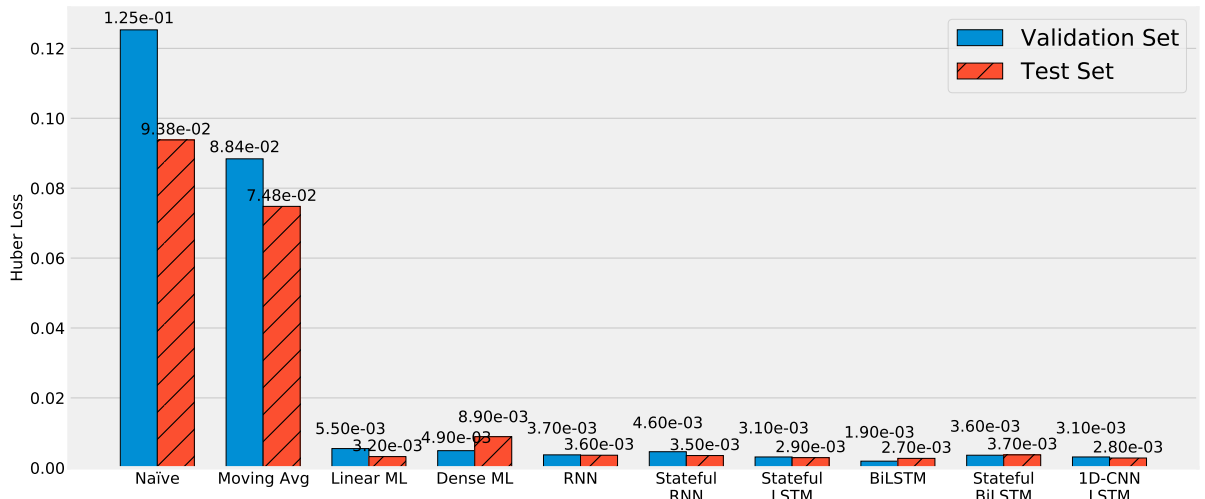


Figure 4.3: Benchmarking of 10 models, shows the Huber loss for the validation and test sets.

4.3.3 Results and discussion

Long-term Forecasting

In Figure 4.3, ML-based methods showed similar performance, outperforming persistence and moving average models. The BiLSTM model exhibited superior performance across validation and test sets.

Three BiLSTM models, one per energy channel, were developed and trained to forecast SEP integral flux. Model performance was evaluated using Huber loss (Fig. 4.4), MAE, and learning rate adjustments via `LearningRateScheduler` callback function.

Experimentation revealed batch size and optimizer learning rate as critical hyperparameters affecting model performance (Greff et al. 2016). Other architectural changes yielded marginal improvements but increased training time and computational resources.

Figure 4.5 depicts model predictions against observations for 1-day, 2-day, and 3-day forecasts across energy channels. Correlation analysis on the out-of-sample test set showed high correlation across forecast windows. Correlation between modeled data and observations declined with longer forecast horizons, especially noticeable between 1 and 1.5 on the x-axis. Rolling window analysis (Fig. 4.6) revealed correlation drops during solar cycle transitions.

During low solar activity, forecasting low SEP fluxes becomes challenging due to increased randomness. Factors influencing correlation during quiet periods require further investigation.

Model performance ranked highest for >60 MeV, followed by >10 MeV and >30 MeV channels. Correlation decline at >30 MeV is consistent with previous findings (Le & Zhang 2017).

Visual inspection of test set examples (Fig. 4.5) revealed strong correlation between predicted and observed onset time, peak time, and end times of SEP events. This suggests that the model effectively captures temporal variations and flux trends in SEP events.

Evaluation using skill scores and threshold-based clustering algorithm demonstrated declining performance with longer forecasting windows. Our model showed comparable performance with previous studies (Table 4.3), with lower false alarm rate compared to UMASEP model.

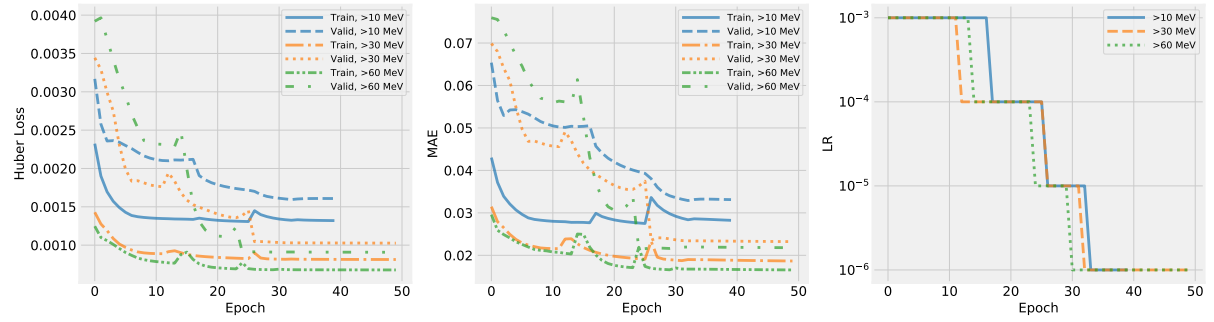


Figure 4.4: *Left Panel* - The Huber loss vs. the number of training epochs for the BiLSTM model for the validation and test sets, for the 3 energy channels. *Middle Panel* - The mean absolute error (MAE); the model's metric vs. the number of training epochs. *Right Panel* - Shows how the learning rate of the Adam optimizer changes over the number of epochs.

Table 4.1: Summary of the performance results of the models for the validation and test sets.

Validation Set									
log PF >10 MeV					log PF >30 MeV			log PF >60 MeV	
Model Loss	0.0016				0.0010			0.0009	
Model Metric	0.0329				0.0232			0.0218	
MAE	0.061	0.091	0.125	0.053	0.079	0.098	0.052	0.069	0.086
MSE	0.013	0.028	0.054	0.010	0.031	0.055	0.009	0.027	0.047
RMSE	0.114	0.168	0.233	0.098	0.176	0.234	0.097	0.164	0.217
MAPE	22.156	28.104	34.721	13.039	18.590	22.735	10.036	13.994	16.731
Test Set									
log PF >10 MeV					log PF >30 MeV			log PF >60 MeV	
Model Loss	0.0014				0.0011			0.0010	
Model Metric	0.0333				0.0283			0.0250	
MAE	0.072	0.099	0.125	0.053	0.088	0.107	0.045	0.066	0.081
MSE	0.015	0.030	0.050	0.009	0.029	0.048	0.007	0.020	0.034
RMSE	0.121	0.172	0.224	0.094	0.170	0.218	0.082	0.141	0.184
MAPE	30.135	37.498	48.139	20.599	34.300	40.803	12.358	20.504	25.305

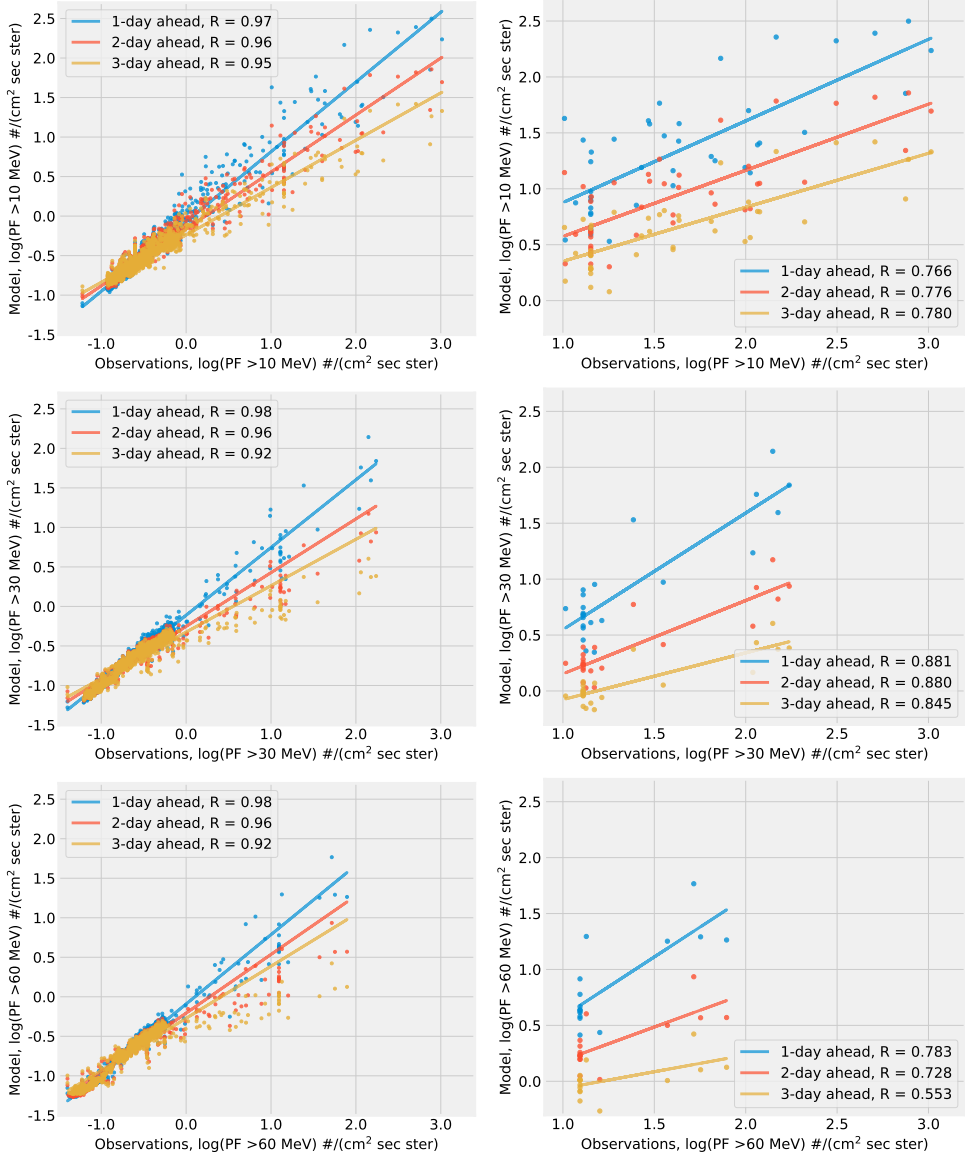


Figure 4.5: Correlation between the model predictions and observations for 1-day, 2-day, and 3-day ahead for >10 MeV (top panel), >30 MeV (middle panel), and >60 MeV (bottom panel). The panels in the left column represent all the points of the test set, those in the right column represent all the observations points with daily mean flux ≥ 10 pfu.

Table 4.2: Confusion matrix for the energy channel ≥ 10 MeV predictions in the test set.

E >10 MeV	No. events	TP	TN	FP	FN
1-day ahead	15	21	1441	2	13
2-day ahead	13	14	1441	2	20
3-day ahead	5	5	1443	0	29

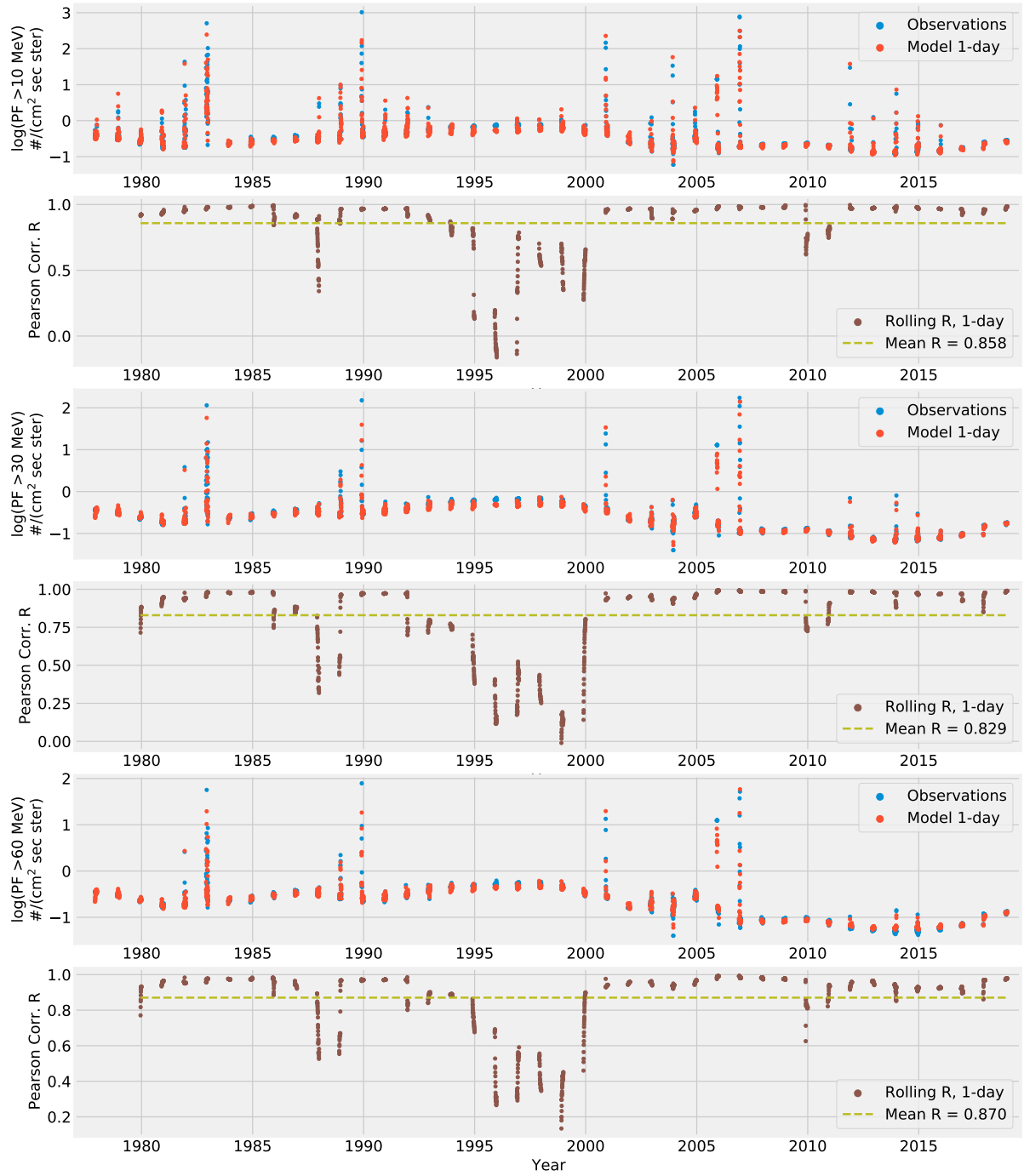


Figure 4.6: Comparison between the model outputs and observations of the test set for the 3 energy channels. In addition to the rolling-mean window correlation for 1-day ahead predictions.

Table 4.3: Comparing the skill scores with previous models. The dashed entries mean the data is unavailable (Whitman et al. (2023) for more details).

Model	POD	FAR	TSS	HSS	POFD	CSI	Accuracy	Precision
Our BiLSTM model	1-Day	0.618	0.087	0.531	0.732	0.001	0.583	0.99
	2-Day	0.412	0.125	0.287	0.553	0.001	0.389	0.985
	3-Day	0.147	0	0.147	0.252	0	0.147	0.980
UMASEP-10 (Núñez 2011)	0.822	0.219	—	—	—	—	—	—
PCA (Papaioannou et al. 2018)	0.587	0.245	—	0.65	—	—	—	—
SPARX (Dalla et al. 2017)	0.5	0.57	—	—	0.32	0.3	—	—
SPRINTS (Engell et al. 2017)	0.56	0.34	—	0.58	—	—	—	—
REleASE (Malandraki & Crosby 2018)	0.63	0.3	—	—	—	—	—	—

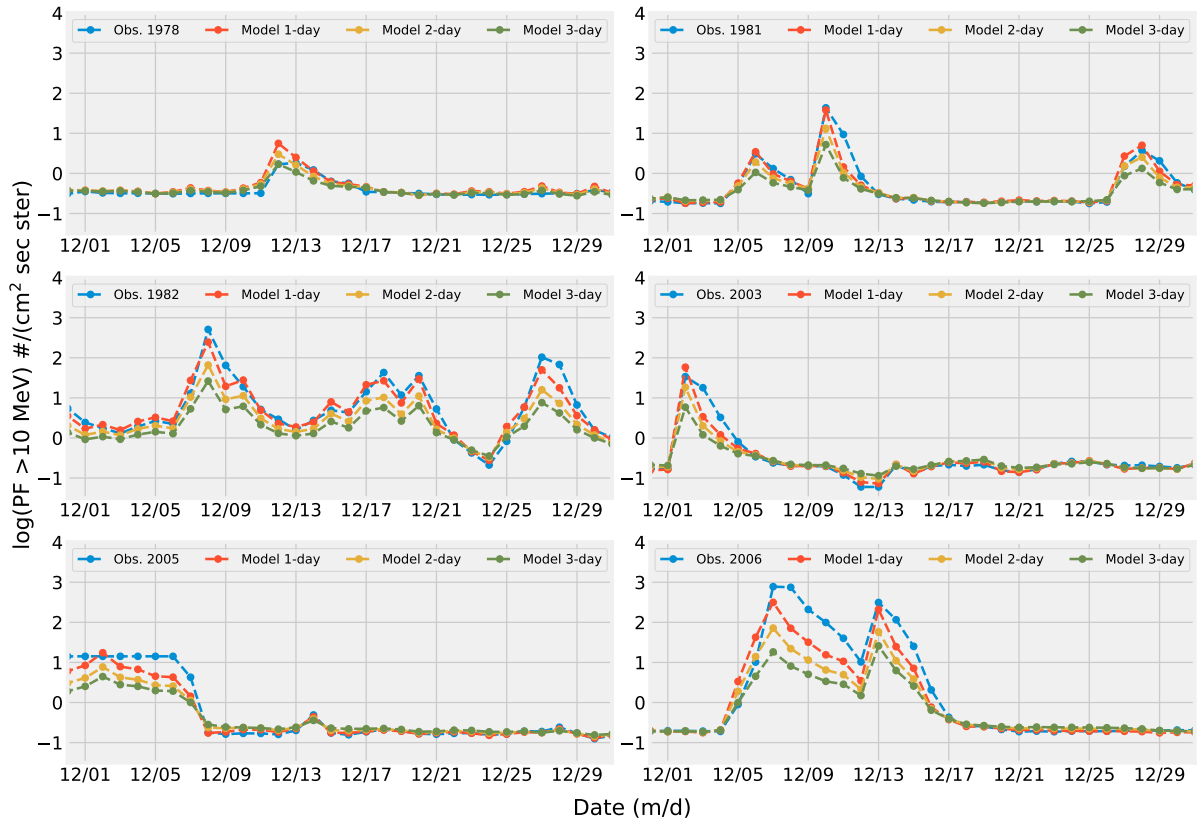


Figure 4.7: The model's forecasts for the out-of-sample testing set for the >10 MeV channel are shown at forecast horizons of 1 day, 2 days, and 3 days ahead, using samples of data from December in selected years mentioned in the top-left side of the plots.

Short-term Forecasting

This study aims to enhance the prediction accuracy of SEP integral flux, crucial for mitigating space weather hazards (Nedal et al. 2023a). Employing a BiLSTM NN model, it utilizes high-resolution hourly-averaged data from four standard integral GOES channels. Key input parameters include the F10.7 index, sunspot number, x-ray flux, solar wind speed, and IP magnetic field strength, sourced from OMNIWeb and GOES databases across two solar cycles. Additional features, like active region locations from NOAA daily reports, are incorporated for improved predictions.

Evaluation involves out-of-sample testing, assessing feature impacts, and benchmarking against existing methods. Data partitioning follows the 9-2-1 strategy over a 23-year period (1996–2018), with 73.99%, 16.44%, and 9.57% allocated to training, validation, and testing sets respectively. Data formatting adopts the MIMO strategy (Benson et al. 2020).

The model forecasts the logarithm of integral proton flux across energy channels, with a focus on >10 MeV. Figure 4.9 compares 1-hour predictions with observations for two sample SEP events.

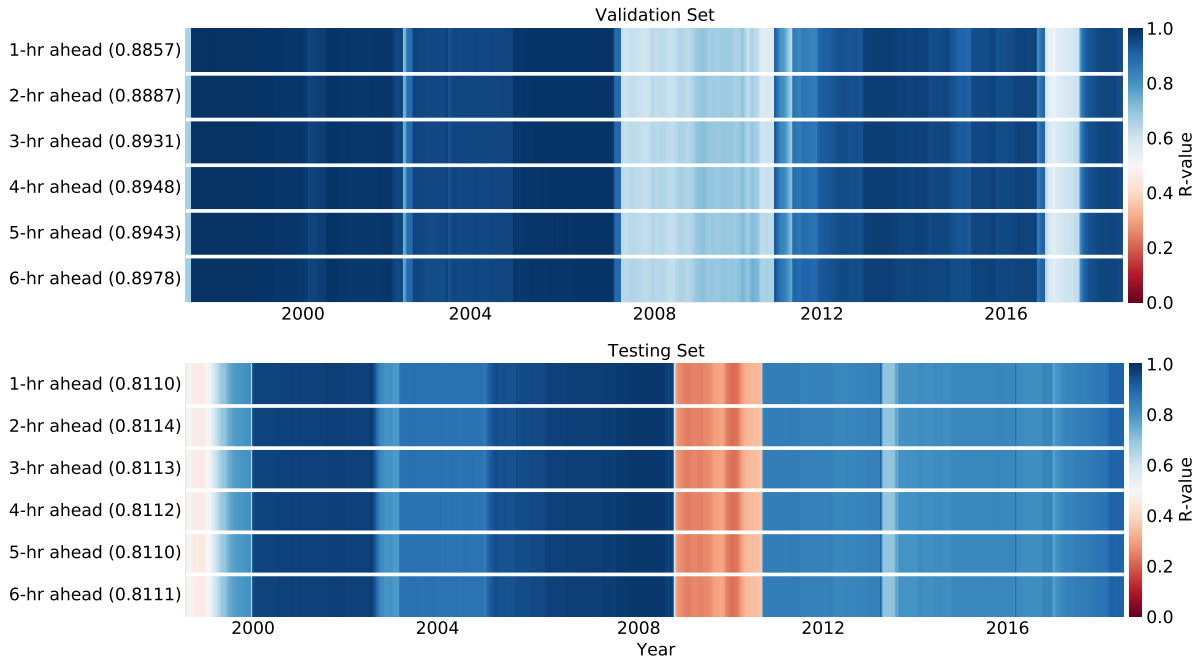


Figure 4.8: Temporal heatmap shows a comparison between the model outputs and observations for the rolling-mean window correlation of the integral >10 MeV proton flux at six predicting windows. The top panel represents the validation set and the bottom panel represents the testing set. The numbers on the y-axis are the mean R values.

Table 4.4: The MSE/MAE for the validation and test sets over six forecasting windows.

	1-hr	2-hr	3-hr	4-hr	5-hr	6-hr
Valid. Set	0.078/0.238	0.086/0.254	0.091/0.263	0.098/0.273	0.102/0.280	0.115/0.299
Test Set	0.012/0.080	0.012/0.079	0.012/0.080	0.011/0.079	0.011/0.080	0.011/0.079

4.4 Conclusions

In Kozarev et al. (2022), we pioneer a multi-event exploration, comprehensively examining Sun-to-1 AU SEP simulations utilizing detailed coronal diffusive shock acceleration and interplanetary propagation. Analyzing 62 eruptive events with the SPREAdFAST framework, originally designed for early-stage SEP event forecasting, yielded promising results, showcasing the framework's efficacy.

Input spectra for coronal proton acceleration were derived from quiet-time suprathermal spectra scaled to the Sun. Coronal proton acceleration, influenced by solar corona conditions, exhibited significant impacts on proton acceleration and shock wave surface characteristics.

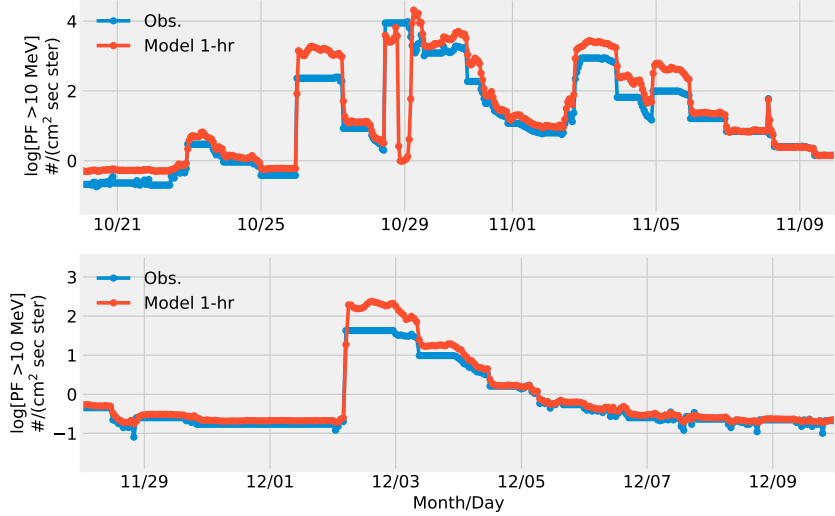


Figure 4.9: Comparison between the model’s forecast and the observations for the integral >10 MeV proton flux at forecast horizon of 1 hour ahead. The top panel represents a sample of the validation set and the bottom panel represents a sample of the testing set.

Comparing DSA model results with SOHO/ERNE instrument observations at 1 AU revealed promising alignment, though discrepancies, particularly at higher energies, were noted. Future work will focus on realistic event modeling, incorporating time-dependent injection of source spectra and three-dimensional transport effects.

In Nedal et al. (2023a), BiLSTM neural networks are developed and trained to predict daily-averaged integral flux of SEP at 1-day, 2-day, and 3-day ahead, focusing on energy channels >10 MeV, >30 MeV, and >60 MeV. Input data from OMNIWeb databases span four solar cycles, utilizing MIMO strategy for forecasting, achieving promising results with low MSE values and strong correlations.

The study highlights challenges in longer-term SEP forecasting, particularly in maintaining model performance over extended forecasting windows. Short-term predictions are crucial for space weather forecasting, emphasizing the significance of accurate modeling for protecting space assets.

BiLSTM networks offer promise for heliophysics forecasting tasks, warranting further investigation into optimal model configurations and data requirements. Our study contributes to the growing field of deep learning in heliophysics and space weather research.

In conclusion, our work demonstrates the potential of BiLSTM neural networks in forecasting SEP integral fluxes, essential for space weather forecasting and safeguarding space assets. Future efforts will focus on real-time prediction models, incorporating recent data and enhancing model sophistication for improved accuracy.

Chapter 5

Summary

In this final chapter, I provide a comprehensive summary of key findings from the dissertation's chapters, focusing on EUV waves, solar type III bursts, and SEP modeling and forecasting. Exploration of Coronal Bright Fronts (CBFs) and the Wavetrack tool enhances understanding of solar dynamics. Extending the CBF dataset promises deeper insights, while multi-wavelength observations aim to elucidate energetic particle origins. Developments in interpretable deep learning models driven by higher resolution data offer potential for advancing SEP forecasting.

Chapter 2 analyzes base-difference images from SDO/AIA to study EUV waves, calculating kinematic parameters and employing SOHO/LASCO measurements. The introduction of Wavetrack facilitates automated identification of dynamic coronal phenomena, showing proficiency in tracking complete pixel maps. Chapter 3 examines type III bursts during PSP's near-Sun encounters, observing sixteen bursts using PSP/FIELDS and LOFAR. A semi-automated pipeline aids in data analysis, aligning bursts and locating emissions off the southeast limb, suggesting a single source of electron beams low in the corona. Chapter 4 investigates Sun-to-Earth SEP simulations for 62 eruptive events, utilizing the SPREAdFAST framework. Input spectra for coronal proton acceleration demonstrate solar corona influence, with overall alignment with in situ observations. A BiLSTM neural network model for forecasting SEP integral flux at 1 AU shows promising results for short-term predictions.

In conclusion, the dissertation contributes to understanding EUV waves, offers an automated tool for tracking coronal phenomena, provides insights into type III bursts and SEP simulations, and advances forecasting using deep learning. Future directions include refining models and incorporating recent data for comprehensive space weather forecasting.

The quest to understand the Sun's dynamic nature persists, with future heliophysics research poised to advance our knowledge and space weather forecasting capabilities.

Expanding the dataset for EUV waves across solar cycle phases offers insights into their behavior amidst cyclical solar activity. Similarly, analyzing solar radio bursts across diverse active regions enhances our understanding of their characteristics. Utilizing multi-wavelength observations from instruments like LOFAR, Parker Solar Probe, and Solar Orbiter enriches our understanding of energetic particles and radio bursts in the solar corona. High-resolution data enhances the accuracy of dynamic process representations. Addressing scattering and propagation effects on SEPs and radio burst observations is crucial for refining forecasting models.

Incorporating features from active regions into SEP prediction models improves forecasting capabilities. Implementing interpretable deep learning architectures enhances model reliability and reduces forecasting errors. Developing real-time analysis tools integrating data from new instruments and space-craft, alongside advanced methodologies, enables early warnings and accurate risk assessments for space weather events.

Bibliography

- Abe, O., Fakomiti, M., Igboama, W., et al. 2023, Advances in Space Research, 71, 2240
- Akansu, A. N. 1991, Optical Engineering, 30, 912
- Akasofu, S. I. 1981, Space Science Reviews, 28, 121
- Alharbi, F. R. & Csala, D. 2021, in 2021 International Conference on Electrical, Communication, and Computer Engineering (ICECCE), IEEE, 1–6
- Altschuler, M. D. & Newkirk, G. 1969, Solar Physics, 9, 131
- Amari, T., Canou, A., & Aly, J.-J. 2014, Nature, 514, 465
- Aschwanden, M. J. 2002, Space Science Reviews, 101, 1
- Aschwanden, M. J. 2010, Solar Physics, 262, 235
- Badman, S. T., Carley, E., Cañizares, L. A., et al. 2022, The Astrophysical Journal, 938, 95
- Bale, S., Goetz, K., Harvey, P., et al. 2016, Space science reviews, 204, 49
- Bastian, T., Pick, M., Kerdraon, A., Maia, D., & Vourlidas, A. 2001, The Astrophysical Journal, 558, L65
- Battarbee, M., Vainio, R., Laitinen, T., & Hietala, H. 2013, Astronomy & Astrophysics, 558, A110
- Bein, B. M., Berkebile-Stoiser, S., Veronig, A. M., et al. 2011, apj, 738, 191
- Benson, B., Pan, W. D., Prasad, A., Gary, G. A., & Hu, Q. 2020, Solar Physics, 295, 65
- Berghmans, D., Auchère, F., Long, D. M., et al. 2021, Astronomy & Astrophysics, 656, L4
- Besliu-Ionescu, D., Maris Muntean, G., & Dobrica, V. 2022, Solar Physics, 297, 65
- Biesecker, D., Myers, D., Thompson, B., Hammer, D., & Vourlidas, A. 2002, The Astrophysical Journal, 569, 1009
- Bonnin, X., Hoang, S., & Maksimovic, M. 2008, Astron. Astrophys., 489, 419
- Borovsky, J. E. & Denton, M. H. 2006, Journal of Geophysical Research: Space Physics, 111
- Boudjada, M. Y., Abou el Fadl, A., Galopeau, P. H., Al-Haddad, E., & Lammer, H. 2020, Advances in Radio Science, 18, 83
- Brewer, D. A., Barth, J. L., Label, K. A., Kauffman, W. J., & Giffin, G. 2002, Acta Astronautica, 51, 609
- Byrne, J., Long, D., Gallagher, P., et al. 2013, Astronomy & Astrophysics, 557, A96
- Camporeale, E. 2019, Space weather, 17, 1166
- Cane, H. V., Erickson, W., & Prestage, N. 2002, Journal of Geophysical Research: Space Physics, 107, SSH
- Cattell, C., Glesener, L., Leiran, B., et al. 2021, Astron. Astrophys., 650, A6

- Che, H. 2018, Journal of Physics: Conference Series, 1100, 012005
- Chen, N., Ip, W.-H., & Innes, D. 2013, *Astrophys. J.*, 769, 96
- Chen, P. 2016, Low-Frequency Waves in Space Plasmas, 379
- Chen, P. F., Wu, S. T., Shibata, K., & Fang, C. 2002, *The Astrophysical Journal*, 572, L99
- Chen, X., Kontar, E. P., Chrysaphi, N., et al. 2023, arXiv e-prints, arXiv:2306.09160
- Cheung, M. C., Boerner, P., Schrijver, C., et al. 2015, *The Astrophysical Journal*, 807, 143
- Chhabra, S., Klimchuk, J. A., & Gary, D. E. 2021, *The Astrophysical Journal*, 922, 128
- Dalla, S., Swalwell, B., Battarbee, M., et al. 2017in (Cambridge University Press), 268–271
- Debrunner, H., Flückiger, E., Grädel, H., Lockwood, J., & McGuire, R. 1988, *Journal of Geophysical Research: Space Physics*, 93, 7206
- Delannée, C. & Aulanier, G. 1999, *Solar Physics*, 190, 107
- Dierckxsens, M., Tziotziou, K., Dalla, S., et al. 2015, *Solar Physics*, 290, 841
- Domingo, V., Fleck, B., & Poland, A. I. 1995, *Solar Physics*, 162, 1
- Dulk, G., Steinberg, J.-L., Lecacheux, A., Hoang, S., & MacDowall, R. J. 1985, *Astronomy and Astrophysics*, 150, L28
- Dungey, J. 1961, *Journal of Geophysical Research*, 66, 1043
- Eastwood, J., Nakamura, R., Turc, L., Mejnertsen, L., & Hesse, M. 2017, *Space Science Reviews*, 212, 1221
- Echer, E. & Gonzalez, W. 2022, *Advances in Space Research*, 70, 2830
- Echer, E., Tsurutani, B., & Gonzalez, W. 2013, *Journal of Geophysical Research: Space Physics*, 118, 385
- Efron, B. 1979, *The Annals of Statistics*, 7, 1
- Engell, A., Falconer, D., Schuh, M., Loomis, J., & Bissett, D. 2017, *Space Weather*, 15, 1321
- Ergun, R., Larson, D., Lin, R., et al. 1998, *The Astrophysical Journal*, 503, 435
- Feynman, J., Armstrong, T., Dao-Gibner, L., & Silverman, S. 1990, *Solar Physics*, 126, 385
- Fletcher, L., Dennis, B. R., Hudson, H. S., et al. 2011, *Space science reviews*, 159, 19
- Florios, K., Kontogiannis, I., Park, S.-H., et al. 2018, *Solar Physics*, 293, 28
- Fox, N., Velli, M., Bale, S., et al. 2016, *Space Science Reviews*, 204, 7
- Gabriel, S., Evans, R., & Feynman, J. 1990, *Solar physics*, 128, 415
- Gallagher, P. T., Lawrence, G. R., & Dennis, B. R. 2003, *The Astrophysical Journal Letters*, 588, L53
- Gieseler, J., Dresing, N., Palmroos, C., et al. 2023, *Frontiers in Astronomy and Space Sciences*, 9, 384
- Gonzalez, W., Joselyn, J.-A., Kamide, Y., et al. 1994, *Journal of Geophysical Research: Space Physics*, 99, 5771
- González, W. D., Echer, E., Clua-Gonzalez, A., & Tsurutani, B. T. 2007, *Geophysical research letters*, 34
- Goodfellow, I., Bengio, Y., & Courville, A. 2016, *Deep learning* (MIT press)
- Gopalswamy, N. 2022, *Atmosphere*, 13, 1781

- Gopalswamy, N., Akiyama, S., Yashiro, S., Michalek, G., & Lepping, R. 2008, Journal of Atmospheric and Solar-Terrestrial Physics, 70, 245
- Gopalswamy, N., Mäkelä, P., & Yashiro, S. 2019, Sun and Geosphere, 14, 111
- Gopalswamy, N., Mäkelä, P., Yashiro, S., et al. 2017in , IOP Publishing, 012009
- Gopalswamy, N., Mäkelä, P., Yashiro, S., Akiyama, S., & Xie, H. 2022a, in 2022 3rd URSI Atlantic and Asia Pacific Radio Science Meeting (AT-AP-RASC), 1–4
- Gopalswamy, N. & Yashiro, S. 2011, apjl, 736, L17
- Gopalswamy, N., Yashiro, S., Akiyama, S., et al. 2022b, Journal of Geophysical Research: Space Physics, 127, e2022JA030404
- Graves, A. & Jaitly, N. 2014in (Beijing, China: PMLR), 1764–1772
- Graves, A. & Schmidhuber, J. 2005, Neural networks, 18, 602
- Greff, K., Srivastava, R. K., Koutník, J., Steunebrink, B. R., & Schmidhuber, J. 2016, IEEE transactions on neural networks and learning systems, 28, 2222
- Guo, F. & Giacalone, J. 2013, The Astrophysical Journal, 773, 158
- Gurnett, D. A. & Anderson, R. R. 1976, Science, 194, 1159
- Gurnett, D. A. & Anderson, R. R. 1977, Journal of Geophysical Research, 82, 632
- Hale, G. E., Ellerman, F., Nicholson, S. B., & Joy, A. H. 1919, Astrophys. J., 49, 153
- Harra, L., Brooks, D. H., Bale, S. D., et al. 2021, Astronomy & Astrophysics, 650, A7
- Hochreiter, S. & Schmidhuber, J. 1997, Neural computation, 9, 1735
- Holman, G. D., Aschwanden, M. J., Aurass, H., et al. 2011, Space science reviews, 159, 107
- Holschneider, M., Kronland-Martinet, R., Morlet, J., & Tchamitchian, P. 1989, in Wavelets. Time-Frequency Methods and Phase Space, ed. J.-M. Combes, A. Grossmann, & P. Tchamitchian (Springer-Verlag), 286
- Huang, X., Tan, H., Lin, G., & Tian, Y. 2018, 2018 International Conference on Artificial Intelligence and Big Data (ICAIBD), 185
- Ihianle, I. K., Nwajana, A. O., Ebenuwa, S. H., et al. 2020, IEEE Access, 8, 179028
- Ireland, J., Inglis, A. R., Shih, A. Y., et al. 2019, Solar Physics, 294, 158
- Ishikawa, S.-n., Glesener, L., Krucker, S., et al. 2017, Nature Astronomy, 1, 771
- Jackson, B., Hick, P., Buffington, A., et al. 2010in , American Institute of Physics, 659–662
- Jang, S., Moon, Y.-J., Kim, R.-S., Lee, H., & Cho, K.-S. 2016, The Astrophysical Journal, 821, 95
- Kahler, S., Cliver, E., Cane, H., et al. 1987, in Proceedings of the 20th International Cosmic Ray Conference Moscow, Volume 3, p. 121
- Kahler, S., Sheeley Jr, N., Howard, R., et al. 1984, Journal of Geophysical Research: Space Physics, 89, 9683
- Kahler, S. W., Cliver, E. W., & Ling, A. G. 2007, Journal of Atmospheric and Solar-Terrestrial Physics, 69, 43
- Kane, R. 2011, Indian Journal of Radio & Space Physics, 40, 7
- Kasapis, S., Zhao, L., Chen, Y., et al. 2022, Space Weather, 20, e2021SW002842
- Kay, C. & Gopalswamy, N. 2018, Journal of Geophysical Research: Space Physics, 123, 7220
- Kingma, D. P. & Ba, J. 2015, International Conference on Learning Representations (ICLR), San Diego

- Klassen, A., Karlický, M., & Mann, G. 2003a, *Astronomy & Astrophysics*, 410, 307
- Klassen, A., Pohjolainen, S., & Klein, K.-L. 2003b, *Solar Physics*, 218, 197
- Klein, K.-L. & Dalla, S. 2017, *Space Science Reviews*, 212, 1107
- Kolen, J. F. & Kremer, S. C. 2001, Gradient Flow in Recurrent Nets: The Difficulty of Learning LongTerm Dependencies (IEEE), 237–243
- Kong, X., Guo, F., Giacalone, J., Li, H., & Chen, Y. 2017, *The Astrophysical Journal*, 851, 38
- Kontar, E. P., Chen, X., Chrysaphi, N., et al. 2019, *The Astrophysical Journal*, 884, 122
- Kontar, E. P., Emslie, A. G., Clarkson, D. L., et al. 2023, arXiv preprint arXiv:2308.05839
- Kontar, E. P., Yu, S., Kuznetsov, A., et al. 2017, *Nature communications*, 8, 1515
- Kouloumvakos, A., Rodríguez-García, L., Gieseler, J., et al. 2022, *Frontiers in Astronomy and Space Sciences*, 9, 974137
- Kozarev, K., Nedal, M., Miteva, R., Dechev, M., & Zucca, P. 2022, *Frontiers in Astronomy and Space Sciences*, 9, 34
- Kozarev, K. A., Davey, A., Kendrick, A., Hammer, M., & Keith, C. 2017, *Journal of Space Weather and Space Climate*, 7, A32
- Kozarev, K. A., Dayeh, M. A., & Farahat, A. 2019, *The Astrophysical Journal*, 871, 65
- Kozarev, K. A., Evans, R. M., Schwadron, N. A., et al. 2013, *The Astrophysical Journal*, 778, 43
- Kozarev, K. A., Korreck, K. E., Lobzin, V. V., Weber, M. A., & Schwadron, N. A. 2011, *The Astrophysical Journal*, 733, L25
- Kozarev, K. A., Raymond, J. C., Lobzin, V. V., & Hammer, M. 2015, *The Astrophysical Journal*, 799, 167
- Kozarev, K. A. & Schwadron, N. A. 2016, *apj*, 831, 120
- Krucker, S., Hudson, H. S., Jeffrey, N. L. S., et al. 2011, *The Astrophysical Journal*, 739, 96
- Krupar, V., Szabo, A., Maksimovic, M., et al. 2020, *Astrophys. J. Suppl.*, 246, 57
- Kwon, R.-Y., Zhang, J., & Olmedo, O. 2014, *The Astrophysical Journal*, 794, 148
- Laitinen, T. & Dalla, S. 2017, *The Astrophysical Journal*, 834, 127
- Lakhina, G. S. & Tsurutani, B. T. 2016, *Geoscience Letters*, 3, 1
- Lanzerotti, L. J. 2001, Washington DC American Geophysical Union Geophysical Monograph Series, 125, 11
- Lavasa, E., Giannopoulos, G., Papaioannou, A., et al. 2021, *Solar Physics*, 296, 107
- Le, G.-M. & Zhang, X.-F. 2017, *Research in Astronomy and Astrophysics*, 17, 123
- Lecacheux, A., Steinberg, J. L., Hoang, S., & Dulk, G. A. 1989, *Astron. Astrophys.*, 217, 237
- Lemen, J. R., Akin, D. J., Boerner, P. F., et al. 2011, in *The solar dynamics observatory* (Springer), 17–40
- Lemen, J. R., Title, A. M., Akin, D. J., et al. 2012, *Solar Physics*, 275, 17
- Li, B. & Cairns, I. H. 2012, *The Astrophysical Journal*, 753, 124
- Lilensten, J., Coates, A. J., Dehant, V., et al. 2014, *The Astronomy and Astrophysics Review*, 22, 1
- Lin, R. 2005, *Advances in Space Research*, 35, 1857
- Liu, W. & Ofman, L. 2014, *Solar Physics*, 289, 3233

- Long, D. M., Bloomfield, D. S., Chen, P.-F., et al. 2017, *Solar physics*, 292, 1
- Long, D. M., Bloomfield, D. S., Gallagher, P. T., & Pérez-Suárez, D. 2014, *Solar Physics*, 289, 3279
- Long, D. M., DeLuca, E. E., & Gallagher, P. T. 2011, *apjl*, 741, L21
- Ma, S., Raymond, J. C., Golub, L., et al. 2011, *The Astrophysical Journal*, 738, 160
- MacDowall, R., Lara, A., Manoharan, P., et al. 2003, *Geophysical research letters*, 30
- Madjarska, M. S. 2019, *Living Reviews in Solar Physics*, 16, 2
- Magdalenić, J., Marqué, C., Zhukov, A. N., Vršnak, B., & Žic, T. 2010a, *Astrophys. J.*, 718, 266
- Magdalenić, J., Marqué, C., Zhukov, A. N., Vršnak, B., & Žic, T. 2010b, *Astrophys. J.*, 718, 266
- Malandraki, O. E. & Crosby, N. B. 2018, Solar particle radiation storms forecasting and analysis: the HESPERIA HORIZON 2020 project and beyond
- Mann, G., Klassen, A., Aurass, H., & Classen, H.-T. 2003, *Astronomy & Astrophysics*, 400, 329
- Manu, V., Balan, N., Zhang, Q.-H., & Xing, Z.-Y. 2022, *Journal of Geophysical Research: Space Physics*, 127, e2022JA030747
- Markwardt, C. B. 2009, in *Astronomical Society of the Pacific Conference Series*, Vol. 411, *Astronomical Data Analysis Software and Systems XVIII*, ed. D. A. Bohlender, D. Durand, & P. Dowler, 251
- Melrose, D. 1980, *Space Science Reviews*, 26, 3
- Melrose, D. 2017, *Reviews of Modern Plasma Physics*, 1, 1
- Mierla, M., Inhester, B., Antunes, A., et al. 2010in , Copernicus GmbH, 203–215
- Mikić, Z., Linker, J. A., Schnack, D. D., Lionello, R., & Tarditi, A. 1999, *Physics of Plasmas*, 6, 2217
- Miteva, R., Klein, K.-L., Malandraki, O., & Dorrian, G. 2013, *Solar Physics*, 282, 579
- Miteva, R., Nedal, M., Samwel, S. W., & Temmer, M. 2023, *Universe*, 9, 179
- Miteva, R., Samwel, S., Costa-Duarte, M., & Danov, D. 2016, in *Proceedings of the Eighth Workshop” Solar Influences on the Magnetosphere, Ionosphere and Atmosphere*, Vol. 30, 27–30
- Miteva, R., Samwel, S., Costa-Duarte, M., & Malandraki, O. 2017, *Sun Geosph*, 12
- Moore, R. L., Sterling, A. C., Hudson, H. S., & Lemen, J. R. 2001, *The Astrophysical Journal*, 552, 833
- Morosan, D. E. & Gallagher, P. T. 2017, in *Planetary Radio Emissions VIII*, ed. G. Fischer, G. Mann, M. Panchenko, & P. Zarka, 357–368
- Nammous, M. K., Saeed, K., & Kobojek, P. 2022, *Journal of King Saud University - Computer and Information Sciences*, 34, 764
- Nedal, M., Kozarev, K., Arsenov, N., & Zhang, P. 2023a, *J. Space Weather Space Clim.*, 13, 26
- Nedal, M., Kozarev, K., Zhang, P., & Zucca, P. 2023b, *A&A*, 680, A106
- Nedal, M., Mahrous, A., & Youssef, M. 2019, *Astrophysics and Space Science*, 364, 161
- Newkirk, G. 1967, *Annual Review of Astronomy and Astrophysics*, 5, 213
- Newkirk, Gordon, J. 1961, *Astrophys. J.*, 133, 983
- Nindos, A., Alissandrakis, C. E., Hillaris, A., & Preka-Papadema, P. 2011, *Astron. Astrophys.*, 531, A31
- Nindos, A., Aurass, H., Klein, K. L., & Trottet, G. 2008, *Sol. Phys.*, 253, 3
- Nitta, N. V., Mason, G. M., Wang, L., Cohen, C. M. S., & Wiedenbeck, M. E. 2015, *The Astrophysical Journal*, 806, 235

- Nitta, N. V., Schrijver, C. J., Liu, W., et al. 2013, *The Astrophysical Journal*, 776, 58
- Nymmk, R. 2007, *Advances in Space Research*, 40, 321
- Núñez, M. 2011, *Space Weather*, 9
- Odstrcil, D., Riley, P., & Zhao, X. 2004, *Journal of Geophysical Research: Space Physics*, 109
- Offringa, A. R., McKinley, B., Hurley-Walker, N., et al. 2014, *Mon. Not. R. Astron. Soc.*, 444, 606
- Ofman, L. & Thompson, B. 2002, *The Astrophysical Journal*, 574, 440
- Olah, C. 2015, Neural Networks, Types, and Functional Programming, [Blog post]
- Olmedo, O., Vourlidas, A., Zhang, J., & Cheng, X. 2012, *The Astrophysical Journal*, 756, 143
- Ontiveros, V. & Vourlidas, A. 2009, *The Astrophysical Journal*, 693, 267
- Ontiveros, V. & Vourlidas, A. 2009, *apj*, 693, 267
- Pala, Z. & Atici, R. 2019, *Solar Physics*, 294, 50
- Paouris, E., Vourlidas, A., Papaioannou, A., & Anastasiadis, A. 2021, *Space Weather*, 19, e2020SW002617
- Papaioannou, A., Anastasiadis, A., Kouloumvakos, A., et al. 2018, *Solar Physics*, 293, 1
- Papaioannou, A., Vainio, R., Raukunen, O., et al. 2022, *Journal of Space Weather and Space Climate*, 12, 24
- Park, J., Innes, D. E., Bucik, R., & Moon, Y.-J. 2013, *The Astrophysical Journal*, 779, 184
- Parker, E. N. 1960, *Astrophysical Journal*, 132, 821
- Patsourakos, S. & Vourlidas, A. 2009, *The Astrophysical Journal*, 700, L182
- Patsourakos, S. & Vourlidas, A. 2012, *Solar Physics*, 281, 187
- Patsourakos, S., Vourlidas, A., & Stenborg, G. 2010, *Astrophys. J. Lett.*, 724, L188
- Pérez-Suárez, D., Higgins, P. A., Bloomfield, D. S., et al. 2011, Automated Solar Feature Detection for Space Weather Applications, 207–225
- Pesnell, W. D., Thompson, B. J., & Chamberlin, P. C. 2012, *solphys*, 275, 3
- Piantschitsch, I., Vršnak, B., Hanslmeier, A., et al. 2018, *The Astrophysical Journal*, 860, 24
- Pick, M. 2006, in *Solar and Heliospheric Origins of Space Weather Phenomena*, ed. J.-P. Rozelot, Vol. 699, 119
- Pick, M., Forbes, T. G., Mann, G., et al. 2006, Multi-Wavelength Observations of CMEs and Associated Phenomena, Vol. 21, 341
- Podladchikova, O. & Berghmans, D. 2005, *Solar Physics*, 228, 265
- Pomoell, J. & Poedts, S. 2018, *Journal of Space Weather and Space Climate*, 8, A35
- Priest, E. & Forbes, T. 2007, *Magnetic Reconnection*
- Pulkkinen, T. 2007, *Living Reviews in Solar Physics*, 4, 1
- Pulupa, M., Bale, S., Bonnell, J., et al. 2017, *Journal of Geophysical Research: Space Physics*, 122, 2836
- Pulupa, M., Bale, S. D., Badman, S. T., et al. 2020, *Astrophys. J. Suppl.*, 246, 49
- Qiu, S., Zhang, Z., Yousof, H., et al. 2022, *Advances in Space Research*, 70, 2047
- Ramstad, R., Holmström, M., Futaana, Y., et al. 2018, *Geophysical Research Letters*, 45, 7306
- Reames, D. V. 1999, *Space Science Reviews*, 90, 413

- Reames, D. V. 2013, Space Science Reviews, 175, 53
- Reames, D. V. 2021
- Reid, H. A. 2020, Frontiers in Astronomy and Space Sciences, 7, 56
- Reid, H. A. & Kontar, E. P. 2018a, Astronomy & Astrophysics, 614, A69
- Reid, H. A. & Kontar, E. P. 2018b, The Astrophysical Journal, 867, 158
- Reid, H. A. S. & Ratcliffe, H. 2014, Research in Astronomy and Astrophysics, 14, 773
- Reiner, M. J., Goetz, K., Fainberg, J., et al. 2009, Solar Physics, 259, 255
- Ripley, B. D. 1996, Pattern Recognition and Neural Networks (Cambridge University Press)
- Rodriguez, J., Onsager, T., & Mazur, J. 2010, Geophysical Research Letters, 37
- Rouillard, A. P., Plotnikov, I., Pinto, R. F., et al. 2016, The Astrophysical Journal, 833, 45
- Rouillard, A. P., Sheeley, N. R., Tylka, A., et al. 2012, The Astrophysical Journal, 752, 44
- Saint-Hilaire, P., Vilmer, N., & Kerdraon, A. 2012, The Astrophysical Journal, 762, 60
- Saiz, E., Cerrato, Y., Cid, C., et al. 2013, Journal of Space Weather and Space Climate, 3, A26
- Samwel, S. & Miteva, R. 2023, Advances in Space Research, 72, 3440
- Savitzky, A. & Golay, M. J. 1964, Analytical chemistry, 36, 1627
- Schatten, K. H., Wilcox, J. M., & Ness, N. F. 1969, Solar Physics, 6, 442
- Schrijver, C. J. 2015, Space Weather, 13, 524
- Schrijver, C. J., Kauristie, K., Aylward, A. D., et al. 2015, Advances in Space Research, 55, 2745
- Schrijver, C. J. & Siscoe, G. L. 2010a, Heliophysics: Evolving solar activity and the climates of space and Earth (Cambridge University Press)
- Schrijver, C. J. & Siscoe, G. L. 2010b, Heliophysics: Evolving solar activity and the climates of space and Earth (Cambridge University Press)
- Schuster, M. & Paliwal, K. K. 1997, IEEE transactions on Signal Processing, 45, 2673
- Schwadron, N. A., Gorby, M., Török, T., et al. 2014, Space Weather, 12, 323
- Schwadron, N. A., Townsend, L., Kozarev, K., et al. 2010, Space Weather, 8
- Schwenn, R. 2006, Living reviews in solar physics, 3, 1
- Selvakumaran, R., Veenadhari, B., Akiyama, S., et al. 2016, Journal of Geophysical Research: Space Physics, 121, 8188
- Sokolov, I. V., Roussev, I. I., Skender, M., Gombosi, T. I., & Usmanov, A. V. 2009, The Astrophysical Journal, 696, 261
- Stansby, D., Yeates, A., & Badman, S. T. 2020, Journal of Open Source Software, 5, 2732
- Starck, J.-L. & Murtagh, F. 2002, Astronomical image and data analysis (Springer Netherlands)
- Stepanyuk, O., Kozarev, K., & Nedal, M. 2022, Journal of Space Weather and Space Climate, 12, 20
- Sundermeyer, M., Alkhouri, T., Wuebker, J., & Ney, H. 2014, in Proceedings of the 2014 conference on empirical methods in natural language processing (EMNLP) (Association for Computational Linguistics), 14–25
- Suzuki, S. & Dulk, G. 1985, Cambridge: Cambridge University Press, 289
- Švestka, Z. 1995, Advances in Space Research, 16, 27

- Temmer, M. 2021, Living Reviews in Solar Physics, 18, 4
- Thernisien, A. 2011, The Astrophysical Journal Supplement Series, 194, 33
- Thernisien, A., Vourlidas, A., & Howard, R. 2009, Solar Physics, 256, 111
- Thompson, B. & Young, C. 2016, The Astrophysical Journal, 825, 27
- Thompson, B. c., Gurman, J., Neupert, W., et al. 1999, The Astrophysical Journal, 517, L151
- Thompson, B. J. & Myers, D. C. 2009, *Astrophys. J. Suppl.*, 183, 225
- Thompson, B. J., Plunkett, S. P., Gurman, J. B., et al. 1998, *grl*, 25, 2465
- Torsti, J., Valtonen, E., Lumme, M., et al. 1995, *Sol. Phys.*, 162, 505
- Trottet, G., Samwel, S., Klein, K.-L., Dudok de Wit, T., & Miteva, R. 2015, Solar Physics, 290, 819
- Tsurutani, B. T. 1985
- Tsurutani, B. T., Gonzalez, W. D., & Kamide, Y. 1997, Surveys in geophysics, 18, 363
- Vainio, R. & Laitinen, T. 2008, Journal of Atmospheric and Solar-Terrestrial Physics, 70, 467
- van Haarlem, M. P., Wise, M. W., Gunst, A., et al. 2013, *Astronomy & astrophysics*, 556, A2
- Verbeeck, C., Delouille, V., Mampaey, B., & De Visscher, R. 2014, *Astronomy and Astrophysics*, 561, A29
- Verbeke, C., Mays, M. L., Kay, C., et al. 2022, *Advances in Space Research*
- Veronig, A., Muhr, N., Kienreich, I., Temmer, M., & Vršnak, B. 2010, The Astrophysical Journal Letters, 716, L57
- Vourlidas, A., Lynch, B. J., Howard, R. A., & Li, Y. 2013, Solar Physics, 284, 179
- Vourlidas, A., Syntelis, P., & Tsinganos, K. 2012, Solar Physics, 280, 509
- Vourlidas, A., Wu, S. T., Wang, A. H., Subramanian, P., & Howard, R. A. 2003, *apj*, 598, 1392
- Vršnak, B. & Cliver, E. W. 2008, Solar Physics, 253, 215
- Vršnak, B., Žic, T., Vrbanec, D., et al. 2013, Solar physics, 285, 295
- Warmuth, A. 2015, Living Reviews in Solar Physics, 12, 1
- Webb, D. F. & Howard, T. A. 2012, Living Reviews in Solar Physics, 9, 1
- Whitman, K., Egeland, R., Richardson, I. G., et al. 2023, Advances in Space Research, 72, 5161, cOSPAR Space Weather Roadmap 2022: Scientific Research and Applications
- Wild, J. & McCready, L. 1950, Australian Journal of Chemistry, 3, 387
- Wild, J., Smerd, S., & Weiss, A. 1963, Annual Review of Astronomy and Astrophysics, 1, 291
- Wills-Davey, M., DeForest, C., & Stenflo, J. O. 2007, The Astrophysical Journal, 664, 556
- Wöllmer, M., Zhang, Z., Weninger, F., Schuller, B., & Rigoll, G. 2013, in 2013 IEEE International Conference on Acoustics, Speech and Signal Processing, IEEE, 6822–6826
- Wood, B., Howard, R., & Socker, D. 2010, The Astrophysical Journal, 715, 1524
- Wu, C.-C. & Lepping, R. P. 2016, Solar Physics, 291, 265
- Wuelser, J.-P., Lemen, J. R., Tarbell, T. D., et al. 2004, in Society of Photo-Optical Instrumentation Engineers (SPIE) Conference Series, Vol. 5171, Telescopes and Instrumentation for Solar Astrophysics, ed. S. Fineschi & M. A. Gummin, 111–122

- Xapsos, M. A., Stauffer, C. A., Jordan, T. M., Adams, J. H., & Dietrich, W. F. 2012, IEEE Transactions on Nuclear Science, 59, 1054
- Xie, H., Ofman, L., & Lawrence, G. 2004, Journal of Geophysical Research: Space Physics, 109
- Young, P. R., Tian, H., Peter, H., et al. 2018, Space Science Reviews, 214, 1
- Zhang, J., Cheng, X., & Ding, M.-d. 2012, Nature communications, 3, 747
- Zhang, J. & Dere, K. P. 2006, apj, 649, 1100
- Zhang, J., Richardson, I., Webb, D., et al. 2007, Journal of Geophysical Research: Space Physics, 112
- Zhang, P., Wang, C. B., & Ye, L. 2018, Astronomy & Astrophysics, 618, A165
- Zhang, P., Zucca, P., Kozarev, K., et al. 2022a, The Astrophysical Journal, 932, 17
- Zhang, W., Zhao, X., Feng, X., et al. 2022b, Universe, 8, 30
- Zhu, H., Zhu, W., & He, M. 2022, Solar Physics, 297, 157